UNIVERSITÀ POLITECNICA DELLE MARCHE

FACOLTÀ DI INGEGNERIA

DIPARTIMENTO DI INGEGNERIA CIVILE, EDILE E ARCHITETTURA (DICEA)

CORSO DI LAUREA MAGISTRALE IN INGEGNERIA CIVILE

Caratterizzazione viscoelastica lineare di miscele riciclate a freddo mediante prova di indentazione

Characterising the linear viscoelastic behaviour of cold recycled mixtures using the indentation test

Relatore:

Prof. Ing. Andrea Graziani

Correlatori:

Prof. Denis Jelagin

Ing. Chiara Mignini

Candidato:

Vittoria Grilli

Anno Accademico 2019-2020

Summary

Riassunto **3**

Introduction **6**

Cold recycled materials **8**

1.1 Cold recycling techniques ***8***

1.1.1 Cold in-place recycling 9

1.1.2 Full depth reclamation 10

1.1.3 Cold central plant recycling 11

1.2 Composition of cold recycled mixtures ***12***

1.3 FAM ***14***

Measuring complex modulus using the indentation test **17**

2.1 Linear viscoelastic behaviour ***17***

2.1.1 Creep 18

2.1.2 Stress relaxation 19

2.1.3 Cyclic loading 20

2.1.4 The Maxwell Spring-Dashpot Model 22

2.1.5 The Wiechert Model and Prony series 23

2.1.6. Interconversion between LVE functions based on Prony series in frequency domain 24

2.2 Relaxation modulus obtained from indentation test ***27***

Materials and Methods **30**

3.1 Materials ***30***

3.1.1 Aggregates 30

3.1.2 Bitumen emulsions 33

3.1.3 Hydraulic binders and water 33

3.2 Mixtures and FAM composition ***35***

3.2.1 Mixtures 35

3.2.2 FAM 36

3.3 Mixing, compaction and curing ***39***

3.4 Indentation test ***43***

3.5 Experimental programme ***49***

Results and analysis **53**

4.1 Analysis on one specimen *53*
4.2 Preliminary tests *59*
4.2.1 Machine compliance 59
4.2.2 Linearity check 60
4.3 First run testing *60*
4.3.1 Mixtures 60
4.3.2 FAM 62
4.3.3 Statistical analysis 64
4.3.4 Summary of first run testing 69
4.4 Second run testing *70*
4.4.1 Mixtures 70
4.4.2 FAM 75
4.4.3 Statistical analysis 78
4.4.4 Mastercurves 85
4.4.5 Summary of second run testing 89
4.4.6 Comparison between FAM and Mixtures 90
4.5 Comparison with classical E ∗test *94*
Conclusions **100**
References **102**

Riassunto

Negli ultimi anni, la ricerca sui materiali per la costruzione e la manutenzione delle pavimentazioni stradali è orientata verso il tema della sostenibilità ambientale. Ad oggi esistono diversi metodi sviluppati per il riutilizzo di un materiale al termine della sua vita utile, al fine di ottenere una materia prima di qualità, adatta ad un nuovo utilizzo.

In questo contesto si colloca il riciclaggio a freddo, il cui obiettivo principale è quello di massimizzare il riutilizzo del conglomerato bituminoso di recupero (*Reclaimed Asphalt,* RA) ovvero il materiale dismesso dalle vecchie pavimentazioni.
Nella grande famiglia di miscele riciclate a freddo, ci si concentrerà sui Cement Bitumen Treated Materials (CBTM).

In questa prospettiva, il presente studio si occupa della caratterizzazione del comportamento viscoelastico lineare delle miscele riciclate a freddo mediante prova di indentazione (*indentation test*) eseguita nel laboratorio de "*School of Architecture and the Built Environment"* dell' KTH-Royal Institute of Technology (Stoccolma, Svezia): si verificherà se una prova semi-distruttiva, che inevitabilmente danneggia la superficie del campione, sarà in grado di misurare una grandezza tipica del campo elastico, ovvero il modulo complesso.
Nel programma sperimentale sono stati presi in considerazione diversi materiali, sia in termini di composizione granulometrica (curva continua e curva discontinua) che in termini di tipologia di legante idraulico (cemento a basso contenuto di pH e cemento ad elevata finezza).

In particolare, di ciascuna combinazione dei materiali suddetti, sono state testate sia le miscele che le malte, ottenendo così otto diverse combinazioni di materiali. Inoltre, sono stati utilizzati due diversi tipi di indenter in termini di superficie di contatto. Il programma sperimentale è stato strutturato in due fasi principali, al termine delle quali i risultati sono stati analizzati sia qualitativamente che quantitativamente, attraverso delle analisi statistiche.

La presente tesi si articola in quattro capitoli:

1. Introduzione al riciclaggio a freddo. Sono riassunte le tecniche di riciclaggio a freddo adottate nel settore delle pavimentazioni stradali e sono state analizzate le principali caratteristiche delle miscele riciclate a freddo.
2. Calcolo del modulo complesso mediante la prova di indentazione. È descritta la metodologia per l'esecuzione della prova di indentazione e il comportamento viscoelastico lineare dei materiali.
3. Materiali e metodi. Sono descritti e commentati i materiali utilizzati in questa ricerca e le metodologie di prova e confezionamento dei provini adottate.
4. Risultati e analisi. Sono riportati e discussi i principali risultati ottenuti.

L'obiettivo principale della presente tesi è quello di valutare la fattibilità dell'indentation test come strumento pratico per il calcolo del modulo complesso.
Di seguito sono elencati i risultati ottenuti:

- I risultati di E^* sono fisicamente coerenti, come si può vedere dall' andamento delle isoterme, poiché i valori del modulo complesso aumentano con la diminuzione della temperatura e all'aumentare della frequenza;
- Le analisi statistiche dei valori $G\ (t = 1)$ e dell'intervallo di confidenza dei valori del modulo complesso mostrano una variabilità dei risultati più pronunciata con l'indenter piccolo, a causa dell'effetto scala, poiché l'aggregato grosso ha lo stesso ordine di grandezza dell'area dell'indenter piccolo;
- L'effetto di scala è molto più evidente nelle miscele (a causa della presenza dell'aggregato grosso) e meno marcato nelle malte, al punto da dedurre che per queste ultime, l'uso del tipo dell'indenter è trascurabile, poiché le prove condotte con l'indenter piccolo garantiscono una dispersione dei risultati minore.
- I test eseguiti su campioni diversi (dal momento che l'indentation test è una prova semi-distruttiva) sono più variabili e soggetti ad errori, rendendo così la costruzione delle curve maestre non del tutto accurata. Ne consegue che la prova è molto sensibile anche al minimo cambio di materiale;
- Dal confronto con i test effettuati sugli stessi materiali presso il "Laboratorio di Strade e Trasporti" di DICEA presso l'Università Politecnica delle Marche, si evince un buon andamento per i provini confezionati con la curva continua. I

provini confezionati con la curva discontinua invece, sono affetti da una non-linearità, probabilmente a causa di una rottura prematura del materiale.

Introduction

In recent years, the research on materials for the construction and maintenance of road pavements has been directed towards the theme of environmental sustainability. Nowadays, there are several methods developed to reuse construction materials at the end of their service life, to obtain a raw material suitable for a new use. This context includes *cold recycling materials* whose main objective is to maximise the reuse of the reclaimed asphalt (RA) resulting from the demolition of end-of-life pavements, without heating. In the large scope of cold recycled material mixtures, this research focused on Cement Bitumen Treated Materials (CBTM).

The main objective of this research was to characterise the linear viscoelastic behaviour of cold recycled materials using the indentation test. This measuring technique was recently applied to conventional bituminous materials but, in this thesis, it was applied for the first time to cold materials treated with bitumen emulsion and cement. Four types of materials have been investigated, considering a dense graded and a gap graded distribution, and two type of cement, Sulfoaluminous cement and Portland-slag cement. For each material, mixtures and fine aggregate matrix mortars, obtained by removing coarse aggregate from the mixtures, have been tested. In addition, two different types of indenter in terms of area of contact (2.52 mm and 6.32 mm) have been used.

The experiments were carried out in the Laboratory of *School of Architecture and the Built Environment (ABE)* of the KTH Royale Institute of Technology (Stockholm, Sweden) and have been structured in two main phases, at the end of which the results have been analysed both qualitatively and quantitatively, through statistical analysis. In conclusion, some considerations were made on the feasibility of the test and on the construction of the mastercurves.

This thesis has four chapters:

1. Introduction to cold recycling. The cold recycling techniques adopted in the field of bituminous pavements and the main characteristics of cold recycled mixtures are presented;
2. Measuring the complex modulus using the indentation test. The indentation test and the theoretical background of linear viscoelastic behaviour are presented.
3. Materials and methods. Describes the materials used in this research and the adopted experimental procedures.
4. Results and analysis. The main results are reported and discussed.

Chapter 1.
Cold recycled materials

This chapter will initially introduce the cold recycling techniques adopted in the field of bituminous pavements, which are increasingly being looked at, especially in recent years, due to the growing focus of the construction industry on eco-friendly techniques and sustainability.

Later attention will be focused on the cold recycled mixtures and fine aggregate matrix (FAM) mortars, obtained by removing coarse aggregate from the mixture. FAM mortars can be considered as the binding matrix of the mixture and can be used to predict its mechanical properties.

1.1 Cold recycling techniques

With the rapid development of modern industry, the huge consumption of traditional energy resources, especially petroleum, leads to the severe energy crisis and environmental issues. Above all, seeking alternative pavement materials and initiative construction technology to maintain an efficient, safe and cost effective pavement system has become an urgent task for government departments, academic community as well as construction contractors.

In recent years, due to the obvious advantages of rehabilitating existing pavements, great attention has been paid on recycling technology. Recycling techniques has the virtue of consuming less raw materials and fossil fuel, lower pollutant emissions, and improving the pavement performance (2).

In this regard, bitumen emulsion mixtures play an important role because they are manufactured at ambient temperature and therefore, significantly reduce carbon dioxide emissions and energy consumption, with respect to hot and warm bituminous mixtures.

Bitumen emulsion mixtures are also widely used in cold recycling. Cold recycled mixtures can incorporate up to 100% reclaimed asphalt (RA), further reducing disposal cost and consumption of natural aggregates (3).

In fact, cold recycling is carried out without prior heating of the materials by means of suitable equipment that allows mixing the RA with the bituminous binder, cement, water and the addition of virgin aggregate.

According to the Asphalt Recycling and Reclaiming Association (ARRA), cold recycling techniques can be classified as: cold in-place recycling (CIR), cold central plant recycling (CCPR) and full depth reclamation (FDR) (2).

1.1.1 Cold in-place recycling

It is a cold in-place method that is used to identify procedures where only bituminous layers are milled and incorporated in the recycled mixture. (4) (Figure 1.1). The CIR process consists of the on-site rehabilitation of the asphalt pavement with a recycling train which can range in size from a single unit to a multi-unit train (5).

CIR method has the advantages of being able to completely repair various pavement distresses such as potholes, rutting, irregular cracks, and reflection cracks, prolonging the service life of asphalt pavement and improving the ride comfort. Furthermore, this technology also can save transport cost and energy, shorten project period and relieve the environment pollution by using high percentage of the recycled materials. (2)

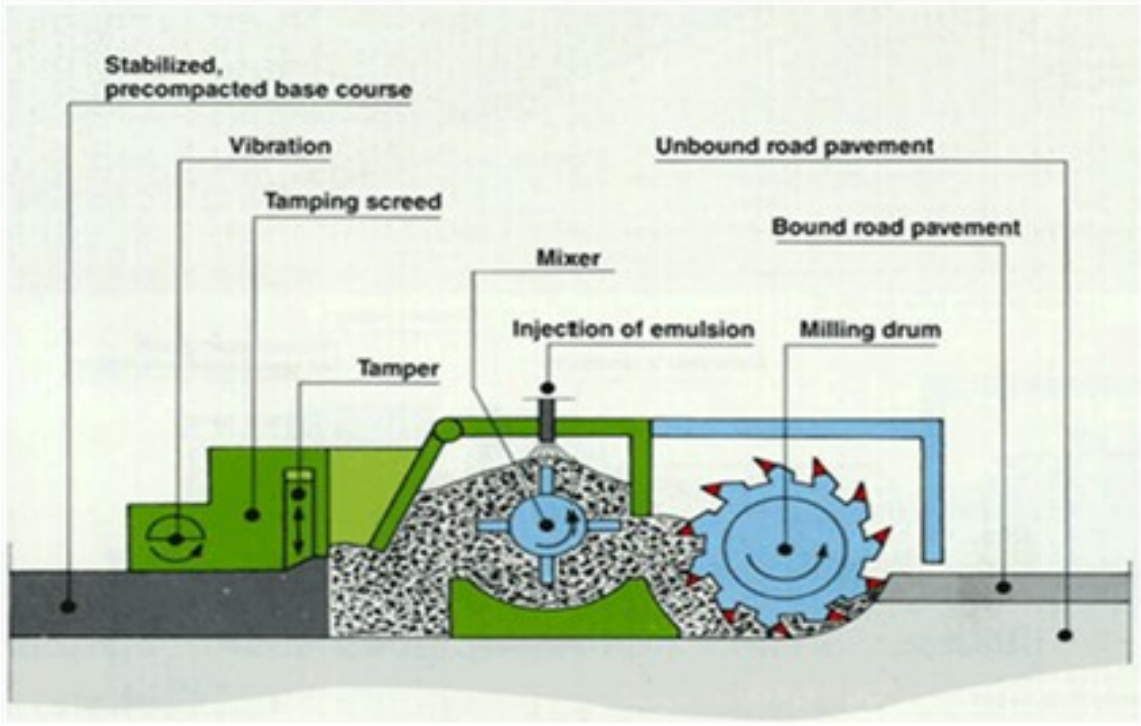

Figure 1.1: Cold in-place recycling

1.1.2 Full depth reclamation

FDR is the rehabilitation technique in which the full thickness of the asphalt pavement and a predetermined portion of the underlying materials (base, subbase and/or subgrade) is uniformly pulverized and blended to provide an upgraded, homogenous base material. FDR is performed on the roadway without the addition of heat, similar to CIR. Treatment depths vary depending on the thickness of the existing pavement structure, but generally range between 4 to 12 inches (100 and 300 mm) (5).

The only difference compared with CIR is that the asphalt layers are milled with part of the base layer together in FDR technology and thus the recycled materials are mixed up with not only the recycled asphalt materials but also the recycled base materials (2). FDR allows a larger amount of material to be recycled, with considerable environmental advantages over CIR (4).

However, some limitations hinder the further application of FDR. The main limitation is the lack of the practical experience and appropriate mix design method, which determines the additive types and dosage, subsequently the construction cost. Additionally, an overlay with certain thickness is needed to improve the water stability

of rehabilitated pavement. Moreover, the application of FDR is highly affected by the climate and environment conditions (2).

1.1.3 Cold central plant recycling

CCPR is conducted at a central or mobile plant. Just as the process of CIR, the first step of CCPR method is also milling the existing asphalt section, and then the milled materials was collected and stockpiled for later use in plant. CCPR is most frequently used as part of a total reconstruction of an existing roadway or in new construction where an existing source of RAP is available (5).

The recycled materials will be crushed to expectation size and then mixed with new materials, additives and water. Subsequently the conventional asphalt wearing course will be paved on the recycling pavement. (2)

Same as CIR method, CCPR also has the advantages of cost reduction, environmental protection, shortening construction periods. However, CCPR has its own superiority compared to CIR method.

Firstly, in CCPR method a better variability control of recycled asphalt and higher quality of CR mixes can be achieved due to the better mixing in the plant. Secondly, the use of CCPR can obviously prolong the design life to 15 and 20 years due to the retained integrity of the overall structural (2).

Three methodologies described above are summarised in Table 1.1.

Table 1.1: Comparison between different Cold recycling methodologies.

Cold recycling Methods	Mixing Technology	Advantages	Limitations
CIR	In situ	1. Save the transport cost. 2. Solve moderate rutting and cracking.	1. Difficult construction quality control. 3. Curing is required.
CCPR	central plant	1. Easy construction quality control. 2. Ideal grading can be achieved. 3. Repair nonstructural distresses.	Curing is required. Transport cost is increased.
FDR	In situ	Solve severe surface and partial structure distresses.	1. Lack of the practical experience 2. Appropriate mix design method is required.

1.2 Composition of cold recycled mixtures

The Reclaimed Asphalt (RA), obtained by milling, planning, or crushing the existing pavement, is considered in its grading curve together with bitumen. The lumps of aggregate bound by bitumen are called grains.

The composition of cold recycled mixtures shall consist of the following materials:

- Reclaimed asphalt (RA), usable in quantities up to 100%;
- Virgin aggregates, inserted in variable quantities to correct the grain size of the milled material;
- Bituminous binder (bituminous emulsion or foamed bitumen), in percentages ranging between 3% and 6%;
- Hydraulic binder, usually cement, in quantities ranging from 1% to 3%;
- Additional water, to ensure machinability to the mixture during application and compaction. In fact, liquids act as lubricants during the compaction phase by replacing heat.

In addition to the RA and natural aggregate, natural filler also plays an important role, since it promotes the dispersion of bitumen within the mixture. If foamed bitumen is used, the quantity and quality of the filler present in the aggregate mixture is essential as the bitumen and filler particles form a mastic that acts as a binder for the coarse aggregates. On the contrary, to bituminous emulsion, the quantity of fillers is less important, as bitumen already partially covers the larger aggregates and filler has the only purpose of correcting the grading curve, if it is missing the fine fraction.

As shown in the graph in Fig. 1.2, obtained as an adaptation of that proposed by *Asphalt Academy (2002)*, it is possible to identify the following Cold Bitumen Emulsion Mixtures (CBEM) families:

- Cement-Bitumen Treated Materials (CBTM) have the same base as Cement Treated Materials (CTM) but are also characterized by the presence of bitumen, showing an intermediate mechanical behaviour between cementitious mixtures and bituminous mixtures. The dosage of both binders is between 1 and 3%.

- Bitumen Stabilized Materials (BSM) are products characterized by a prevalence of bituminous binder, in this case the residual bitumen usually does not exceed 3% (it can be used up to 1% of cement as filler).
- Cold Asphalt Mixtures (CAMs), which exhibit behaviour similar to traditional Bituminous Conglomerates and are mainly used in base layer. They are characterized by a low cement content, at most dosed at 2%, and a high content of bitumen, between 3 and 6%.

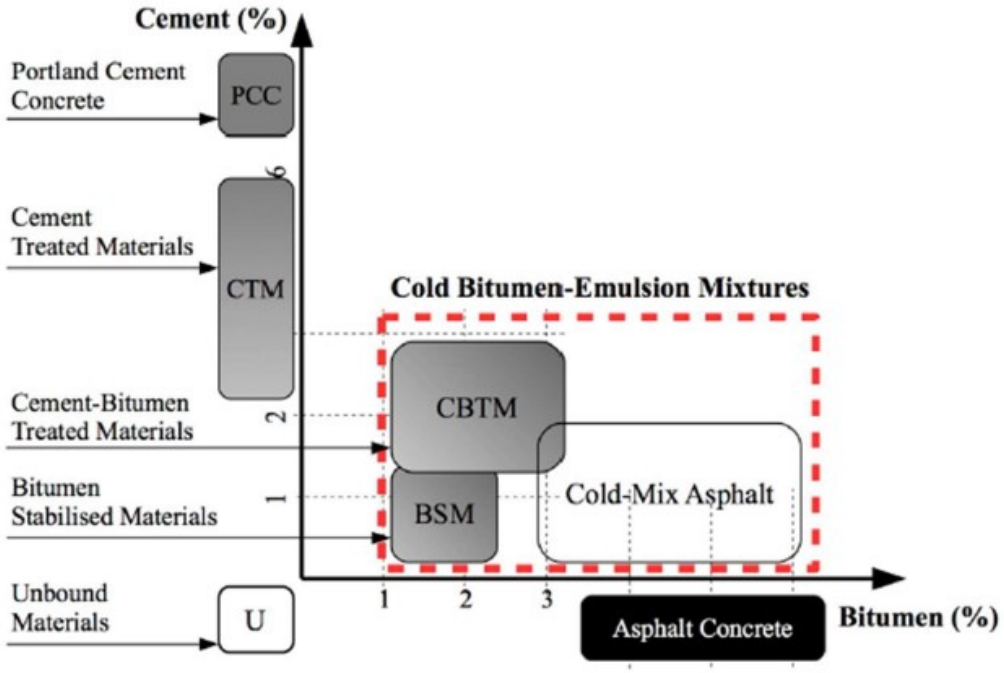

Figure 1.2: composition of pavement mixtures according to the relationship between cementitious binder and bituminous binder (4)

In this thesis *cement bitumen treated materials* will be investigated.

They are characterised by considerably higher cohesion and stiffness with respect to BSMs. The basic idea while preparing CBTMs is to start from a CTMs and, adding a bitumen emulsion, reduce cracking susceptibility and the overall structural stiffness of the recycled layer. This results in a mechanical behaviour closer to that of an asphalt concrete (AC) as thermal dependency and fatigue issues appear (4).

In particular, as it is shown in Table 1.2, the mechanical behaviour of CBTMs depends on the properties and the dosages of hydraulic and bituminous binders (and consequently by bitumen /cement ratio) (6).

Table 1.2: CBTM behaviour dependent on B/C ratio.

Dosage of cement	Dosage of bitumen	B/C ratio	CBTM Behaviour
Low	Low	Not relevant	Markedly stress-dependent (similar to that of granular materials)
Low	High	High	Asphalt- like (due to internal cohesion and temperature dependency)
High	Low	Low	Stiffer mixture, tending to shrinkage cracking (similar to CTMs).

1.3 FAM

The mechanical behaviour of asphalt concrete has been studied at different scales of observation (Fig. 1.3). At the mixture scale, asphalt concrete can be considered a particulate composite where coarse aggregate particles (inclusions) are dispersed in the fine aggregate matrix (FAM) phase. (Figure 1.4)

Several studies have shown that FAM properties affect the viscoelastic, fatigue and fracture behaviour of asphalt concrete mixtures as well as their moisture damage resistance. It was also shown that healing, oxidation and ageing occur in the FAM phase. Besides, FAM has been used to predict the overall behaviour of the mixture using multiscale computational models.

The FAM material is a mortar composed of fine aggregate, filler, bitumen and voids. Its grading distribution derives from the fine part of the mixture grading, with upper sieve size comprised between 1.18 and 2.36 mm (1) (Fig. 1.5).

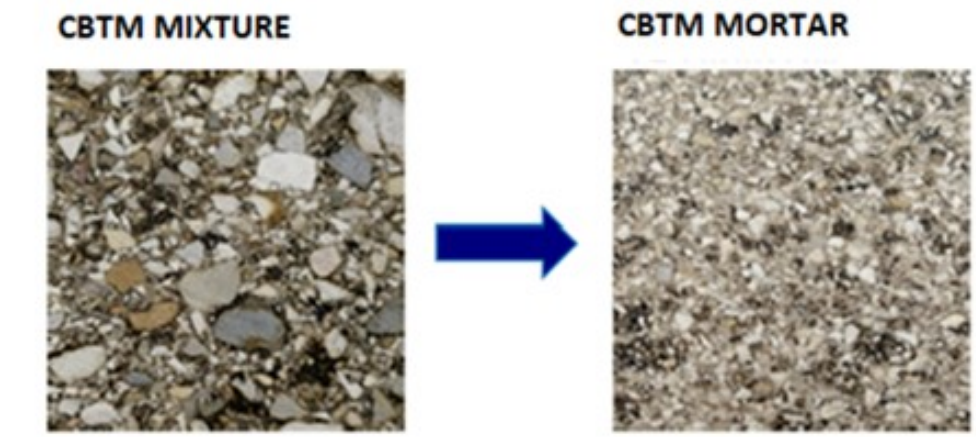

Figure 1.4: Mixture vs Mortar (macroscale)

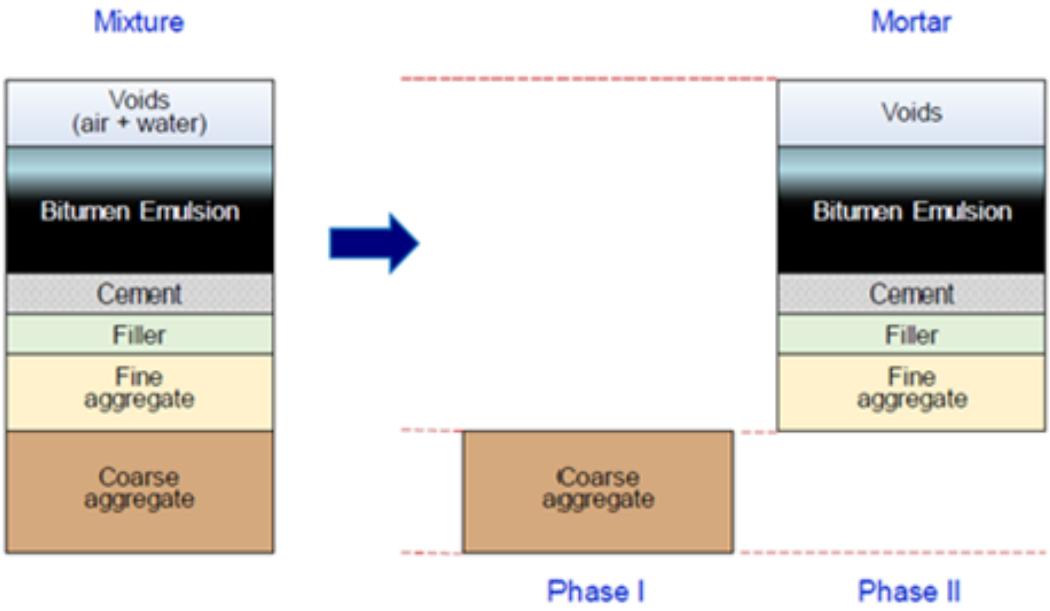

Figure 1.5: CBTM mixture and FAM mortar volumetric composition model

Still moving in the downscaling direction, two further scales of engineering interest can be considered:

- the mastic (at the cured state) or slurry (at the fresh state), is the FAM mortar binding matrix, obtained by removing fine aggregate and voids.

- the bitumen emulsion, is the binding agent of CBE (cold bitumen emulsion) materials along with the eventual cementitious binder. Bitumen emulsion is a composite material itself as the bitumen droplets are dispersed in water. (7)

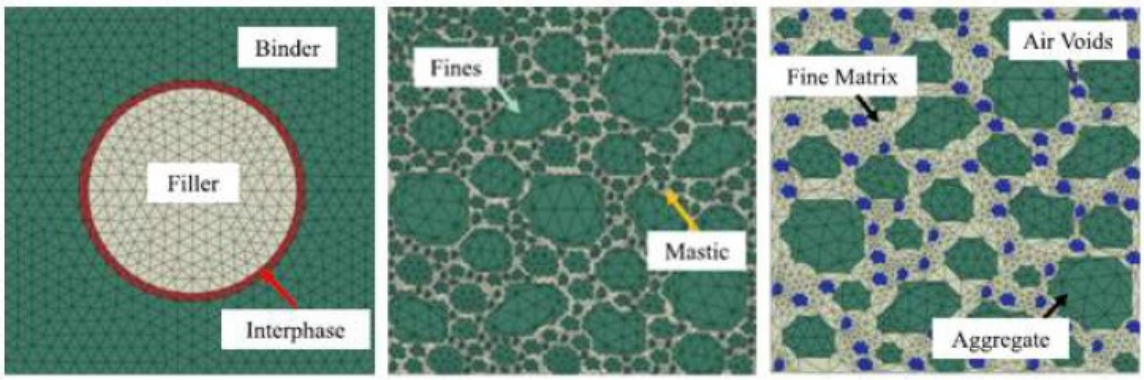

Figure 1.3: Study at different scales with FEM methodology, respectively: the mastic, the FAM and the mixture

Chapter 2.

Measuring complex modulus using the indentation test

In this Chapter will be described the methodology of an *indentation test*, applied to CBTMs. It represents an alternative tool that will lead to derive the complex (or dynamic) modulus, a parameter of fundamental importance to understand the materials LVE behaviour, as it provides information about the amount of energy lost (viscous portion) and stored (elastic portion).

2.1 Linear viscoelastic behaviour

The term *viscoelastic* is derived from the words "viscous" plus "elastic", that means, a viscoelastic material exhibits both elastic and viscous behaviour.

Linear viscoelastic materials are those for which exists a linear relationship between stress and strain (at any given time). Linear viscoelasticity is a theory describing the behaviour of such ideal materials, usually only applicable in the case of small deformations.

In the case of viscoelastic materials, mechanical characterization often consists of performing uniaxial tensile tests similar to those used for elastic solids, but modified so as to enable observation of the time dependency of the material response. Although many such viscoelastic tensile tests have been used, one most commonly encounters only three: creep, stress relaxation, and dynamic (sinusoidal) loading (9).

2.1.1 Creep

Figure 2.1 shows the typical response of a viscoelastic material to a creep recovery test, that is, to a steady uniaxial stress σ_0 and to the subsequent removal of that load.

At first, it suffers an instantaneous strain upon loading. This may include elastic and permanent plastic strain. The strain then increases over time and, this time-dependent response is known as *creep*. The strain usually increases with a decreasing rate. Some of the strain that accumulates during creep will be recoverable upon unloading and some will not.

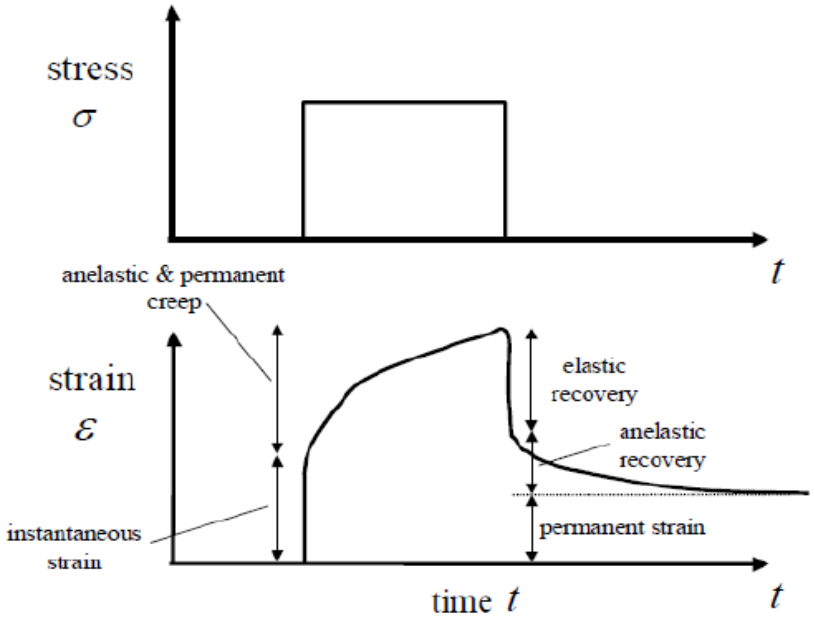

Figure 2.1: Creep

When unloaded, the instantaneous strain is recovered immediately.

More strain is then recovered over time, this is known as anelastic recovery (or delayed elastic recovery).

It is possible to define the creep compliance as follows:

$$J(t) = \frac{\epsilon(t)}{\sigma_0} \tag{2.1}$$

2.1.2 Stress relaxation

Another common test, easily conducted with displacement-controlled machines, consists of monitoring the time-dependent stress resulting from a steady strain (9).

Figure 2.2 shows an example of a dual behaviour to creep: the response, of a viscoelastic material to a r*elaxation tes*t. The material is subjected to a constant strain over time which will cause a decrease in the stress rate.

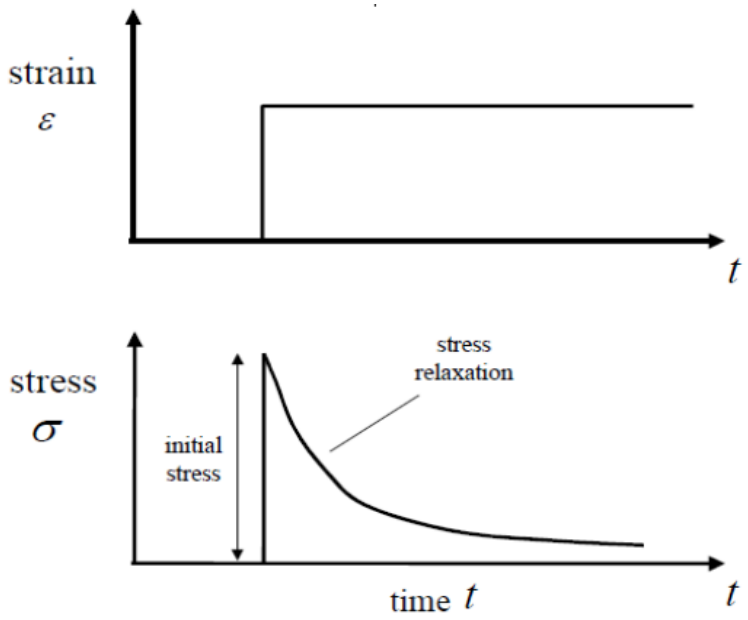

Figure 2.2: Relaxation test

Analogously with creep compliance, one may superimpose the relaxation curves by means of the relaxation modulus defined as (9).

$$E_{rel}(t) = \frac{\sigma(t)}{\epsilon_0} \tag{2.2}$$

2.1.3 Cyclic loading

Creep and stress relaxation tests are convenient for studying material response at long times (minutes to days), but less accurate at shorter times (seconds and less).

When a viscoelastic material is subjected to a sinusoidally varying stress, a steady state will eventually be reached, in which the resulting strain is also sinusoidal, having the same angular frequency but retarded in phase by an angle δ; this is analogous to the delayed strain observed in creep experiments.

The strain lags the stress by the phase angle δ and this is true even if the strain rather than the stress is the controlled variable.

If the origin along the time axis is selected to coincide with a time at which the strain passes through its maximum, the strain and stress functions can be written as

$$\epsilon = \epsilon_0 \cos \omega t \tag{2.3}$$

$$\sigma = \sigma_0 \cos(\omega t + \delta) \tag{2.4}$$

It is convenient to write the stress function as a complex quantity σ^* whose real part is in phase with the strain and whose imaginary part is 90◦ out of phase with it:

$$\sigma^* = \sigma_1 \cos \omega t + i\sigma_2 \sin \omega t \tag{2.5}$$

where $i = \sqrt{-1}$ and the asterisk denotes a complex quantity as usual (9).

It can be useful to visualize the observable stress and strain as the projection on the real axis of vectors rotating in the complex plane at a frequency ω. If we capture their positions just as the strain vector passes the real axis, the stress vector will be ahead of it by the phase angle δ as seen in Fig. 2.3.

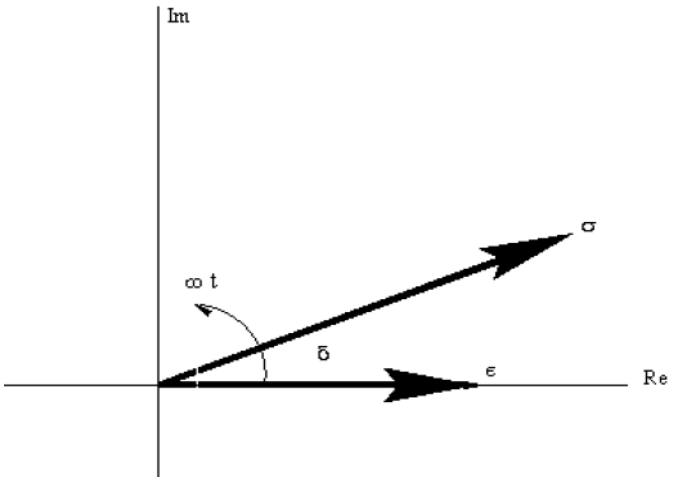

Figure 2.3: Representation in the complex plane

Figure 2.3 makes it easy to develop the relations between the various parameters in harmonic relations.

$$|\sigma^*| = \sigma_0 = \sqrt{\sigma_1^2 + \sigma_2^2} \tag{2.6a}$$

$$\tan \delta = \frac{\sigma_2}{\sigma_1} \tag{2.6b}$$

$$\sigma_1 = \sigma_0 \cos \delta \tag{2.6c}$$

$$\sigma_2 = \sigma_0 \sin \delta \tag{2.6d}$$

It is possible to use this complex form of the stress function to define two different dynamic moduli, both being ratios of stress to strain as usual but having very different molecular interpretations and macroscopic consequences. The first of these is the real or storage modulus, defined as the ratio of the in-phase stress to the strain:

$$E_1 = \frac{\sigma_1}{\epsilon_0} \tag{2.7}$$

The other is the imaginary or loss modulus, defined as the ratio of the out-of phase stress to the strain (9):

$$E_2 = \frac{\sigma_2}{\epsilon_0} \tag{2.8}$$

Similarly, it is possible to define shear storage and shear loss moduli, $\boldsymbol{G_1}$ and $\boldsymbol{G_2}$.

2.1.4 The Maxwell Spring-Dashpot Model

A convenient way of developing time-dependence of viscoelastic response relations while also helping visualize molecular motions employs spring-dashpot models. These mechanical analogues use "Hookean" springs, depicted in Fig. 2.5 and described by

$$\sigma = k\epsilon \tag{2.9}$$

where σ and ϵ are analogous to the spring force and displacement, and the spring constant k is analogous to the Young's modulus E $[N/m^2]$.

The entropic uncoiling process is fluidlike in nature, and can be modelled by a Newtonian dashpot also shown in Fig. 2.5, in which the stress produces not a strain but a strain rate:

$$\sigma = \eta\dot{\varepsilon} \tag{2.10}$$

Here the overdot denotes time differentiation and η is a viscosity with units of Ns/m^2(9).

Figure 2.5: Hookean springs and Newtonian dashpot

The Maxwell solid shown in Fig 2.6 is a mechanical model in which a Hookean spring and a Newtonian dashpot are connected in series.

The spring should be visualized as representing the elastic or energetic component of the response, while the dashpot represents the conformational or entropic component. In a series connection such as the Maxwell model, the stress on each element is the same and equal to the imposed stress, while the total strain is the sum of the strain in each element (9)

$$\sigma = \sigma_s = \sigma_d \tag{2.11}$$

$$\epsilon = \epsilon_s + \epsilon_d \tag{2.12}$$

The behavior is described analytically by the following equation:

$$\sigma(t) = \sigma_0 \exp\left(-\frac{t}{t_{rel}}\right) \tag{2.13}$$

Where $t_{rel} = \eta/E_0$.

Figure 2.6:Maxwell model

2.1.5 The Wiechert Model and Prony series

The Generalized Maxwell model, also known as the Wiechert model, represents the rheological model of stress relaxation $G(t)$. It consists of K_i parallel spring-damper elements and a supplementary parallel linear elastic spring (12) (Fig. 2.7).

It takes into account that the relaxation does not occur at a single time, but at a distribution of times since a real material does not relax with a single relaxation time as predicted by the previous models (9).

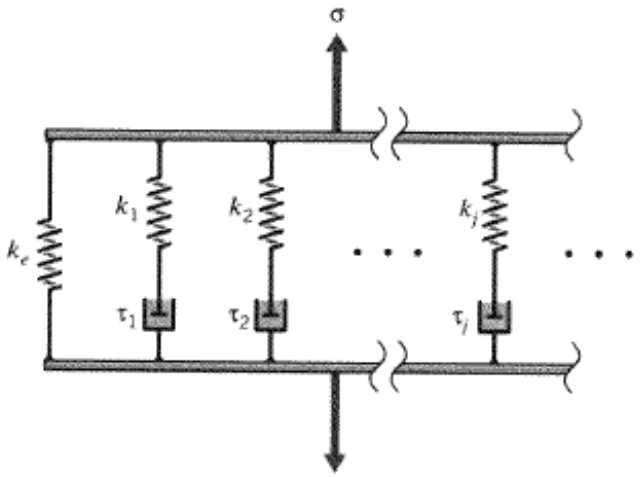

Figure 2.7: the Wiechert model

The Generalised Maxwell model can be represented mathematically by the Prony series equation:

$$G(t) = G_\infty + \sum_{k=1}^{K} G_k \exp\left(\frac{t}{\tau k}\right) \quad (2.14)$$

Where:

- G_∞ is the long term modulus once the material is totally relaxed. G_∞ equals zero when the considered material shows flowing. Otherwise, it tends to a finite positive limit (12).
- τ_k are the relaxation times: the higher their values, the longer it takes for stress to relax;
- G_k is the initial stiffness that every spring-damper element has.

2.1.6. Interconversion between LVE functions based on Prony series in frequency domain

An efficient and accurate numerical method of interconversion between linear viscoelastic material functions based on a Prony series representation is presented by S.W. Park & R.A.Schapery (13).

The uniaxial, nonaging, isothermal stress-strain equation for a linear viscoelastic material can be represented by the following integral

$$\sigma(t) = \int_0^t E(t-\tau)\frac{d\epsilon(t)}{d\tau}d\tau \quad (2.15)$$

called Boltzmann Superposition Integral that allows to calculate the stress output given an arbitrary strain input.

In fact, using integral approach, it is possible to describe not only linear viscoelasticity in terms of mechanical models constructed from linear springs and dashpots, but also the response of the material at time t as the sum of the responses to excitations imposed at all previous times.

The ability to sum these individual responses requires the material to obey a more general statement of linearity than we have invoked previously, specifically that the

response to a number of individual excitations be the sum of the responses that would have been generated by each excitation acting alone (9).
Matematically:

$$\sigma_1(t) = E_{rel}\,(t - \xi_1\,)\Delta\epsilon_1 \tag{2.16}$$

$$\sigma_2(t) = E_{rel}\,(t - \xi_2)\Delta\epsilon_2 \tag{2.17}$$

where the small strain $\Delta\epsilon_1$ is applied at a time $\xi 1$ previous to t (the same for $\sigma_2(t)$).
If the material is linear, the total stress at time t due to both strain increments together can be obtained by superposition of these two individual effects:

$$\sigma(t) = \sigma_1(t) + \sigma_2(t) = E_{rel}\,(t - \xi_1\,)\Delta\epsilon_1 + E_{rel}\,(t - \xi_2)\Delta\epsilon_2 \tag{2.18}$$

As the number of applied strain increments increases so as to approach a continuous distribution, 2.18 leads to Eq. 2.15 (9).

Equation 2.15 is based on the mathematical properties governing all linear nonaging systems. As seen, the stress-strain equation may be expressed in a differential operator form based on a mechanical model consisting of linear springs and dashpots: The generalized Maxwell model or Wiechert model can be described by Equation 2.14.

If one takes into account that creep compliance can be described by Voigt model, from Eq. 2.15 the following integral relationship between the uniaxial relaxation modulus $E(t)$ and creep compliance $D(t)$ is found:

$$\int_0^t E(t-\tau)\frac{dD(t)}{d\tau}d\tau = 1 \quad (t > 0) \tag{2.19}$$

It is possible to define the operational modulus and the compliance as follows

$$\check{\mathrm{E}}(s) = \int_0^\infty E(t)e^{-st}\,dt \tag{2.20}$$

$$\check{\mathrm{D}}(s) = \int_0^\infty D(t)e^{-st}\,dt \tag{2.21}$$

Where the integrals represent the Laplace transform of $E(t)$ and $D(t)$ respectively. Complex material functions arise from the response to a steady-state sinusoidal loading and are related to the operational functions as follows:

$$E^*(\omega) = \check{\mathrm{E}}(s) \,\big|\, s \to i\omega \tag{2.22}$$

$$D^*(\omega) = \check{\mathrm{D}}(s) \,\big|\, s \to i\omega \tag{2.23}$$

The real and imaginary parts are:

$$E^*(\omega) = E_1(\omega) + iE_2(\omega) \tag{2.24}$$

$$D^*(\omega) = D_1(\omega) + iD_2(\omega) \tag{2.25}$$

The operational and the components of complex material functions based on the relationship described above and the Prony series representations (replacing E with G) are given by:

$$G_1(\omega) = G_e + \sum_{i=1}^{m} \frac{\omega^2 \rho_i^2 G_i}{\omega^2 \rho_i^2 + 1} \tag{2.26}$$

$$G_2(\omega) = \sum_{i=1}^{m} \frac{\omega \rho i G_i}{\omega^2 \rho_i^2 + 1} \tag{2.27}$$

Where the real part $G_1(\omega)$ is called shear storage modulus and the imaginary part $G_2(\omega)$ is called shear loss modulus.

The storage and loss modulus in viscoelastic materials measure the stored energy, representing the elastic portion, and the energy dissipated as heat, representing the viscous portion.

2.2 Relaxation modulus obtained from indentation test

In this experimental study, to evaluate the viscoelastic properties of cold mixing asphalt, a spherical indentetion test was carried out in the Laboratory of *School of Architecture and the Built Environment (ABE)* of the KTH Royale Institute of Technology (Stockholm, Sweden); the procedure, developed by Fadil et al. (2018), allows to determine shear relaxation function $G(t)$ from test mesurements.

A basic sketch of the spherical indentation test setup is shown in Figure 2.8. During the test a relatively rigid spherical indenter is pressed into the flat specimen in a displacement-controlled mode, while indentation depth, $h(t)$, and the contact load, $P(t)$ are continuously recoded during the whole testing period.

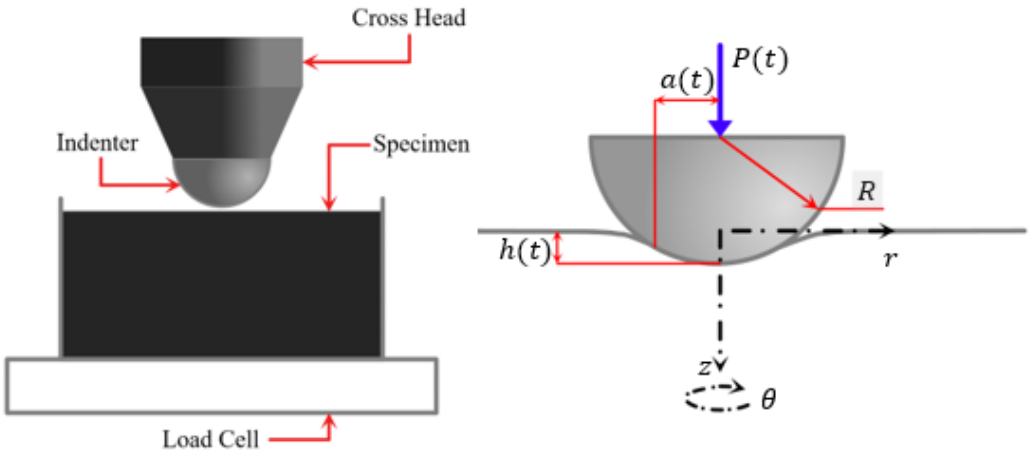

Figure 2.8: Sketch of an indentation test setup

Fig 2.8 shows the parameters used in the analysis method:

- h is the indentation depth;
- P is the contact load;
- a is the contact area radius, related to $h(t)$ as follows:

$$a = \sqrt{h \cdot R} \tag{2.28}$$

- R is the curvature of the spherical indenter.

At arbitrary non decreasing loading, for a frictionless indentation of a rigid spherical indenter into a linear elastic half space, we can consider a solution based on Hertz solution (10).

$$P = \frac{8}{3}\frac{G \cdot a^3}{(1-\nu)\cdot R} \tag{2.29}$$

Where G is the shear relaxation modulus.
The viscoelastic counterpart of this equation may be obtained by utilising Lee's and Radok's method of functional integrals (11).

For the case, of the constant viscoelastic Poisson's ratio i.e. $\nu(t) = \nu_o$, the relationship between the measured $h(t)$ and $P(t)$ is as follows

$$P(t) = \frac{8}{3(1-\nu_o)}\sqrt{R}\int_0^t G(t-\tau) \times \frac{dh^{\frac{3}{2}}(\tau)}{d\tau} d\tau \tag{2.30}$$

where:

- $\nu(t) = \nu o$ is the Poisson's ratio;
- τ is a dummy integration variable.

$h(t)$ is defined by two stage loading history, consisting of the loading stage where $h(t)$ is increased monotonically to the target indentation depth h_t followed by the second stage where the indentation depth is kept constant:

$$h(t) = \begin{cases} \frac{t}{t_r} h_t - P(t) * C_m & for\ t \le t_r \\ h_t - P(t) * C_m & for\ t \ge t_r \end{cases} \tag{2.31}$$

where:

- C_m is the machine compliance;
- t_r is the time when target h is reached.

The shear relaxation modulus $G(t)$ is obtained from the $P(t)$ and $h(t)$ measured during the test by solving numerically the integral Equation 2.30.

It is defines as a relaxation that occurs during test in which the material undergoes a state of constant deformation ε observing over time the decline of the tensional state defining in terms of $\sigma(t)$.

The diagram in Figure 2.9 shows the procedure used in order to obtain the $G^*(\omega)$ starting from the indentation depth h and the contact load P.

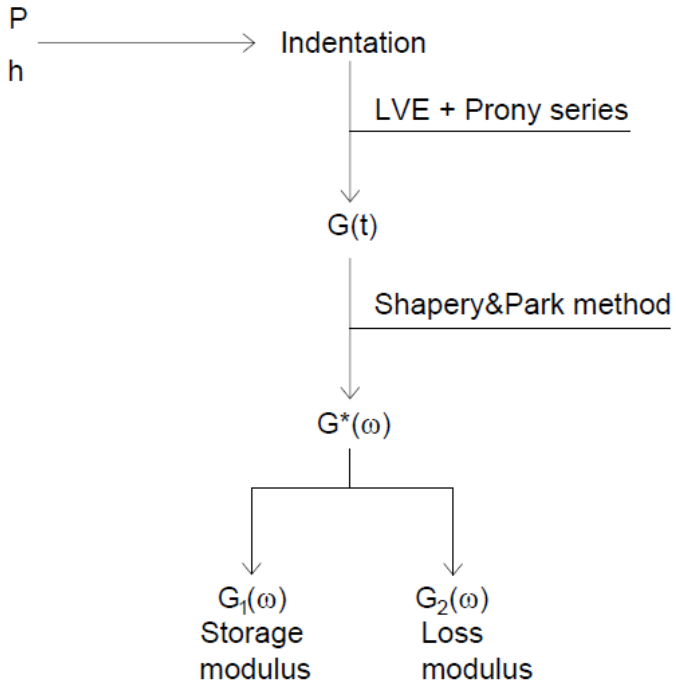

Figure 2.9: procedure adopted to calculate G(ω)*

Chapter 3.
Materials and Methods

The following Chapter will firstly illustrate the materials used in the experimental study and their physical and chemical properties, as well as the mixtures and mortars produced with them, according to two different grading distributions. Then, it will describe the test procedures and instrumentations used for the sample's realization and compaction and the execution of the indentation test for mechanical characterization.
The tests were carried out in the Laboratory of *School of Architecture and the Built Environment (ABE)* of the KTH Royale Institute of Technology (Stockholm, Sweden).

3.1 Materials

Mixtures and FAM mortars were obtained by using a set of materials, according to the ones used for the of CBTM mixtures, briefly described in Chapter 1.

3.1.1 Aggregates

RA aggregate had been crushed in order to obtain a material with a nominal maximum dimension of 16 mm (RA 0/16). Laboratory sieving operations allowed obtaining two further fractions:

- passing the 2 mm sieve (RA 0/2);
- passing the 16 mm and sieve retained on the 2 mm sieve (RA 2/16).

The fine natural aggregate was crushed limestone sand with a nominal maximum dimension of 2 mm, and the filler was finely ground limestone powder (7).
Fig. 3.1 represents the grading distribution of the various aggregate sources.

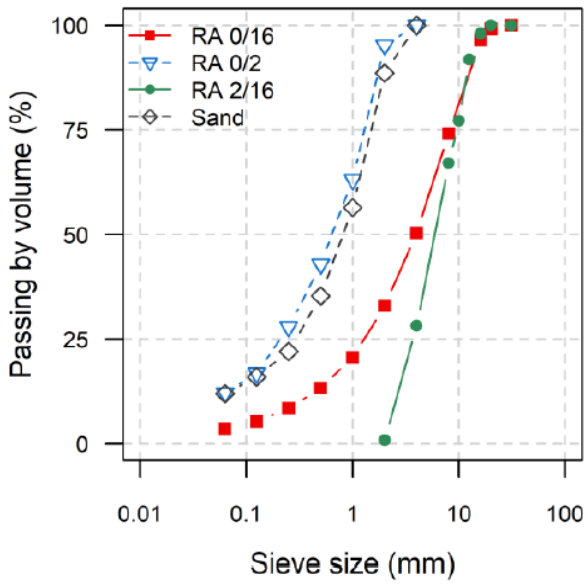

Figure 3.1: Grading distribution of aggregates

Tables 3.1, 3.2, 3.3, 3.4 and 3.5 summarise the main properties of aggregates.

Table 3.1: Properties of RA 0/16

Property	**Standard**	**Symbol**	**Unit**	**Value**
Upper aggregate size	EN 933-1	D	mm	16
Passing the 0.063	EN 933-1	f	%	5.6
Particle density	EN 1097-6	ρ_a	kg/m^3	2482
Water absorption	EN 1097-6	WA_{24}	%	1.14
Flakiness index	EN 933-3	FI	%	7.3
Shape Index	EN 933-4	SI	%	5.7
Crushed aggregate particle	EN 933-5	C	%	100
Sand Equivalent	EN 933-8	SE	%	70.6
Resistance to fragmentation	UNI EN 1097-2	LA	%	17
Resistance to freezing and thawing	EN 1367-1	ΔLA	%	-1.4
Limit Liquid	UNI CEN ISO/TS 17892-12	W_L	%	ND
Plasticity index	UNI CEN ISO/TS 17892-12	IP	-	NP
Soluble binder content (with respect aggregates)	12697-1	S	%	5.0
Fragmentation test by Proctor (10/14)		PCS	%	6.8

Table 3.2: Properties of RA 0/2

Property	Standard	Symbol	Unit	Value
Upper aggregate size	EN 933-1	D	mm	2.0
Passing the 0.063	EN 933-1	f	%	16.9
Particle density	EN 1097-6	ρ_a	kg/m^3	2424
Water absorption	EN 1097-6	WA_{24}	%	1.32
Soluble binder content (with respect aggregates)	12697-1	S	%	8.3

Table 3.3: Properties of RA 2/16

Property	Standard	Symbol	Unit	Value
Upper aggregate size	EN 933-1	D	mm	16
Passing the 0.063	EN 933-1	f	%	0
Particle density	EN 1097-6	ρ_a	kg/m^3	2550
Water absorption	EN 1097-6	WA_{24}	%	1.14
Soluble binder content (with respect aggregates)	12697-1	S	%	3.2

Table 3.4: Properties of fine aggregate

Property	Standard	Symbol	Unit	Value
Upper aggregate size	EN 933-1	D	mm	2
Passing the 0.063	EN 933-1	f	%	12.2
Particle density	EN 1097-6	ρ_a	kg/m^3	2732
Water absorption	EN 1097-6	WA_{24}	%	1.50

Table 3.5: Properties of filler

Property	Standard	Symbol	Unit	Value
Upper aggregate size	EN 933-1	D	mm	0.125
Passing the 0.063	EN 933-1	f	%	45.3
Particle density	EN 1097-6	ρ_a	kg/m^3	2650
Rigden voids	EN 1097-4	*v*	%	23.8
Blaine finesses	EN 196-6	*s*	cm^2/g	3400

Properties of filler

3.1.2 Bitumen emulsions

The bitumen emulsion employed is classified as C60BP10 according to the current standard UNI-EN 13808 (7), and produced with SBS modified bitumen mixed with a small amount of SBS latex.

It is a cationic emulsion with residual bitumen content equal to 60%. Table 3.6 shows the main characteristics of the emulsion and residual bitumen.

Table 3.6: characteristics of the emulsion and residual bitumen

Property	Standard	Unit	Value
Emulsion			
Binder content	EN 1428	%	60
Density		kg/m^3	1015
pH value	EN 12850	-	2.2
Viscosity at 40 °C – efflux time	EN 12846-1	s	40
Adhesivity: water immersion test	EN 13614	%	90
Breaking behaviour: mineral filler method	EN 13075-1		190
Mixing stability with cement	EN 12848	%	< 2
Residual bitumen			
Penetration at 25 °C	EN 1426	dmm	100
Softening point	EN 1427	°C	60

3.1.3 Hydraulic binders and water

The cements used in this experimental study were two:

- Sulfoaluminous cement (CSA), not standardised within the European standards framework;
- Portland-slag cement (PSC) type II/B-S with strength class 52.5N (EN 197-1);

These two types of cement are innovative compared to the classic Portland cement normally used in construction practice.

CSA has rapid setting and hardening, very high 28 days strength. It also has a lower pH compared to conventional Portland-based cements. PSC has ordinary early strength, but a high 28 days strength (7).

Tables 3.7 and 3.8 show the main characteristics and chemical composition of the cements.

Table 3.7: characteristics of CSA and PSC

Property		**CSA**	**PSC**
Volumetric mass	g/cm^3	2.90±0.03	3.09±0.01
Blaine fineness	cm^2/g	5700±200	4090±100
Rigden voids	%	33.5	33.4
Cumulative <90µm	%	99.5	99.5
pH		11-12	12-13.5
Initial setting time*	min	15	180
Final setting time*	min	25	245
Compressive strength @2 days *	MPa	45±2	20±2
Compressive strength @28 days*	MPa	80±3	56±3

*Standard mortar

Table 3.8: Chemical composition of CSA and PSC

Component	**CSA**	**PSC**
CaO	40.00	55.54
Al_2O_3	25.00	6.67
SiO_2	7.00	25.64
Fe_2O_3	1.20	2.26
MgO	3.50	4.28
Na_2O	0.50	0.36
K_2O	0.50	0.71
TiO_2	0.30	0.44
P_2O_5	0.08	0.07
Mn_2O_3	0.15	n.c.
SrO	0.60	n.c
SO_3	20.30	2.49

Water was added to improve the workability and compatibility of mixtures and to make possible the cement hydration process. During mixing the total water W_{tot} is differentiated into two categories:

- Emulsion water $w_{em,}$ which is part of the contribution of free water w_{free};

- Additional external water w_{add} , a fraction of the additional water is absorbed by the aggregate permeable voids w_{abs}, (i.e water needed for aggregates to reach the SSD condition) while the remaining fraction, along with the emulsion water, was identified as intergranular water w_i.

3.2 Mixtures and FAM composition

The samples preparation starts from four CBTM mixtures compositions, obtained considering:

- 2 grading distributions: DG (Dense graded) and GG (Gap graded curve);
- 2 high strength cementitious binder types: CSA and PSC (described above).

DG represents a continuous curve with NMAS 16 mm, derived from the Fuller-Thompson reference distribution; GG is a gap-graded distribution with NMAS 16 mm, derived from specifications for stone mastic asphalt. Its coarse fraction was constituted by RA 2/16, whereas the fine fraction was natural aggregate (7).

3.2.1 Mixtures

Tables 3.9 and 3.10 describe the composition by mass and by volume of the investigated mixtures.

Table 3.9: Composition by mass of mixtures

Aggregate		Cement		Bitumen (residual)	
Grading curve	Composition (%)	Type	Dosage (%)*	Type	Dosage (%)*
DG	80% RA 0/16 17% sand 3% filler	CSA	2.5	BP	3.0 %
		PSC	2.5	BP	3.0 %
GG	70% RA 2/16 20% sand 10% filler	CSA	2.5	BP	3.0 %
		PSC	2.5	BP	3.0 %

*by dry aggregate mass Voids: 9.5 %

Table 3.10: Composition by volume of mixtures

	DG		GG	
	CSA Volume (%)	PSC Volume (%)	CSA Volume (%)	PSC Volume %
RA-ssd coarse (2/16)	45,1	45,2	58,8	58,9
Sand-ssd coarse (2/4)	2,5	2,6	2,9	2,9
RA - ssd fine (0/2)	22,2	22,2	0,0	0,0
Sand-ssd fine (0/2)	10,6	10,6	12,9	12,9
Filler	2,3	2,3	7,9	7,9
Cement	1,8	1,6	1,8	1,7
Bitumen	6,0	6,0	6,2	6,2
W (additional+emulsion)	6,7	6,7	6,0	6,0
Air	2,8	2,8	3,5	3,5
sum	100,0	100,0	100,0	100,0

3.2.2 FAM

Tables 3.11 and 3.12 describe the composition of mortars investigated.

Table 3.13: composition by mass of mortars

Aggregate		Cementitious Binder		Emulsion dosage	Total water dosage*	Voids volume V_m
Grading curve	Composition (%)	Type	Dosage (%)*	Dosage (%)	Dosage (%)	(%)
DG	61% RA 0/2 31% sand 7% filler	CSA PSC	5.9 %	11.8 %	6.5%	13.2%
GG	63% sand 37% filler	CSA PSC	9.5%	19 %	9.1%	18.4 %

*by dry aggregates mass

Table 3.12: composition by volume of mortars

	DG		GG	
	CSA Volume (%)	PSC Volume (%)	CSA Volume (%)	PSC Volume (%)
RA-ssd coarse (2/16)	-	-	-	-
Sand-ssd coarse (2/4)	-	-	-	-
RA - ssd fine (0/2)	45,0	45,1	-	-
Sand-ssd fine (0/2)	21,5	21,5	36,7	36,8
Filler	4,7	4,7	22,3	22,4
Cement	3,5	3,3	5,1	4,8
Bitumen	12,2	12,2	17,5	17,5
W (additional+emulsion)	9,1	9,1	12,8	12,8
Air	4,1	4,1	5,7	5,7
sum	100,0	100,0	100,0	100,0

Figures 3.3 and 3.4 depicts the different grading distribution respectively for DG and GG (FAM and mixtures)

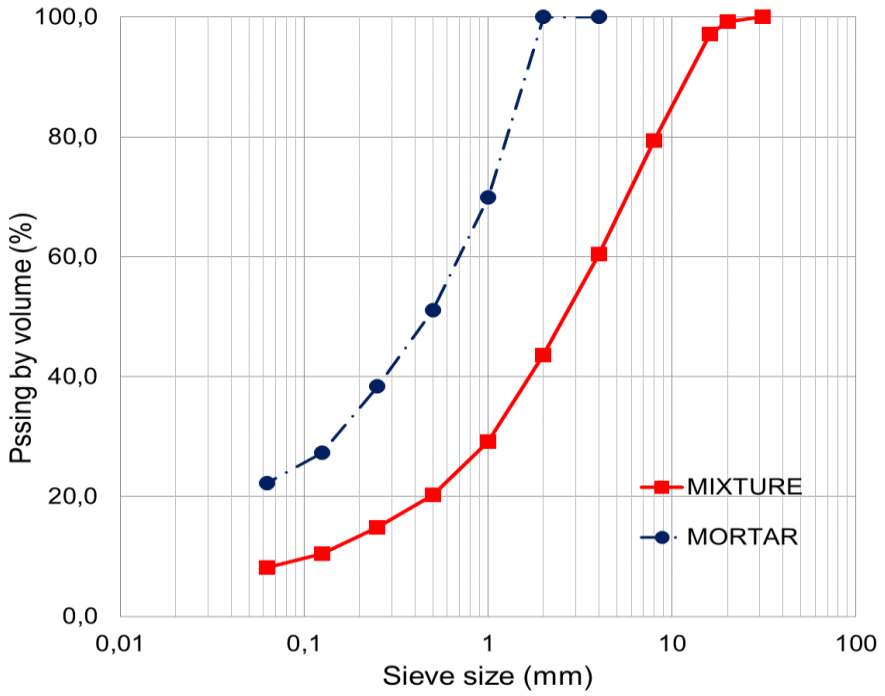

Figure 3.2: DG grading distribution

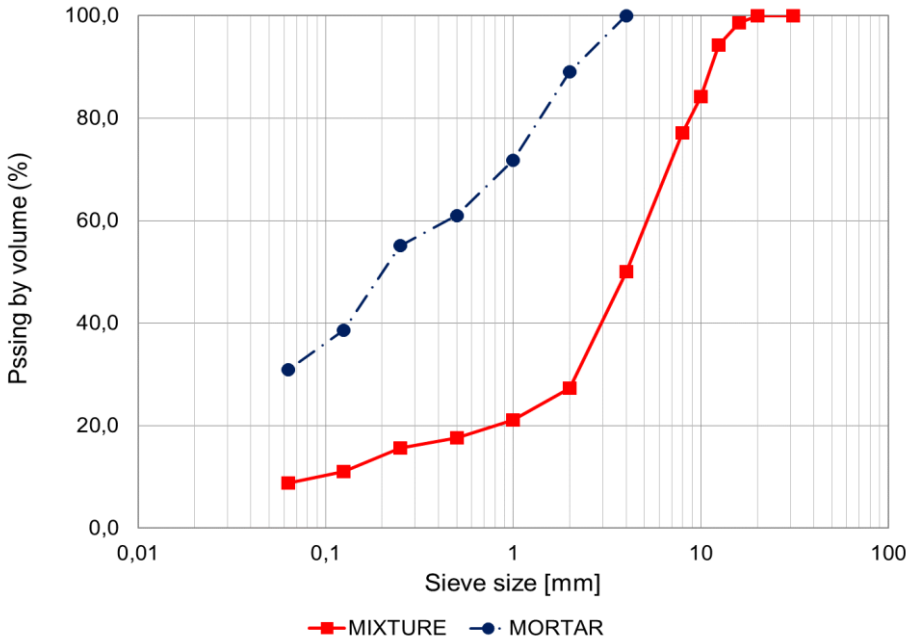

Figure 3.3: GG grading distribution

3.3 Mixing, compaction and curing

The mixing, compaction and curing procedures of mixtures and FAM mortars were carried out at the "Laboratorio Strade e Trasporti" of DICEA at *Università Politecnica delle Marche.*

Mixing

The mixing was performed in two stages using mechanical mixer (Fig. 3.4): The primary mixing, (preparation of the fine aggregate to achieve the saturated surface dry (SSD) condition), and secondary mixing, (addition of the binders to the SSD aggregates)

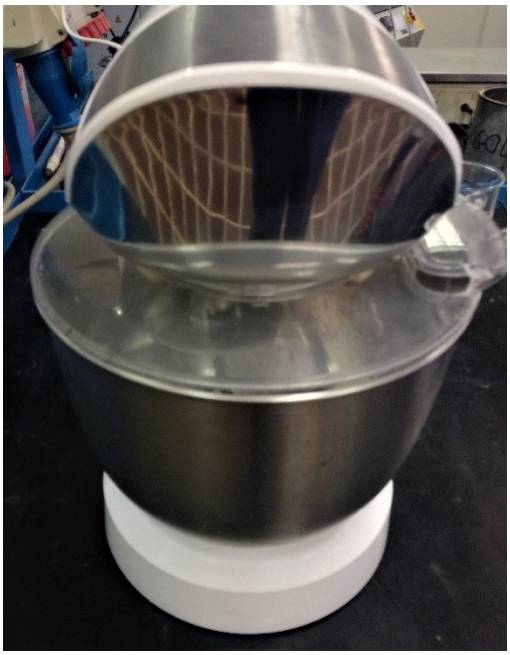

Figure 3.4: mechanical mixer

First, aggregates were dried until reaching constant mass, at (105 ± 2) °C for natural aggregate and (40 ± 2) °C for RA. Then, was added the amount of water to achieve the SSD condition and this fine aggregate mixture was stored in a sealed plastic bag for at least 12 h at room temperature (Figures 3.5a-b)

Figure 3.5: a) addition of water b) sealing of the mixture in a plastic bag

In the secondary mixing, it was added:

- the required amount of cement and it was mixed for about 1 min;
- half of the required amount of bitumen emulsion and it was mixed for 1 min;
- the remaining amount of bitumen emulsion and it was mixed for 1 min. (14)

Water was added after 8 minutes, bitumen emulsion after 11 minutes. After the whole process, the particle coating was checked by visual esamination. (Fig. 3.6a-e)

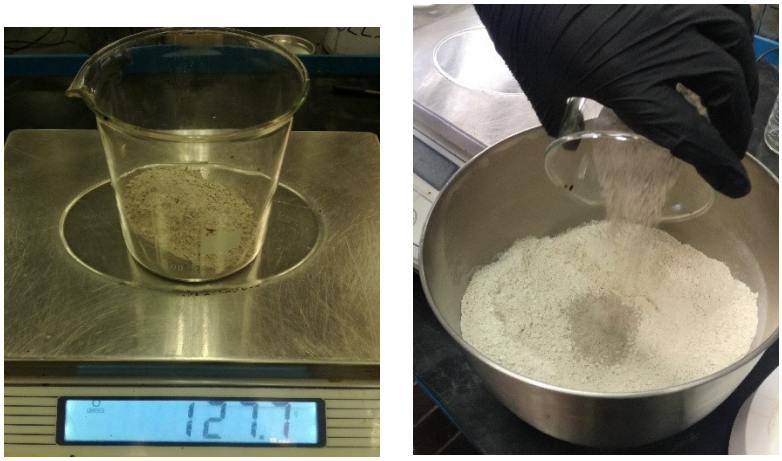

Figure 3.6: a- b) weighing and addition of the cement; c-d) addition of the first and second part of bitumen emulsion; e) aspect of the mixture from the end of the mixing.

Compaction

Compaction of mixtures and mortar specimens started immediately after the mixing end and was performed using a *Superpave gyratory compactor (SGC)*. The adopted protocol required constant pressure of 600 kPa, gyration speed of 30 rpm and an inclination angle of 1.25° (7).

The compaction procedure was the following: a paper disk was put in the mould with a diameter of 100 mm. For each specimen, the mortar blend was mixed by hand before pouring the material in the mould (to be sure obtaining homogeneous specimens); then, a paper disk was included above the mixture in the mould and was checked the total weight. Now, the mould is ready to be inserted in the gyratory compactor, as seen in Figure 3.7a-b.

Figure 3.7: a) pouring of the mixture in the mould; b) compaction using SGC

At each gyration, the height of the specimens was measured, allowing monitoring the volumetric properties of materials. To check possible material loss during compaction, the mass of the mould containing the loose material before compaction was compared with the mass of the mould containing the compacted specimen (7).

When the compaction was finished, the specimen was extruded from the mould and weighed, as shown in Fig. 3.8a-b.

Figure 3.8: a) extrusion of the specimen; b) weighing of the specimen after the compaction

Immediately the specimen was stored in a climatic chamber to start the curing process and register the starting curing time;

Curing

The curing of mixtures and FAM mortar specimens was carried out in a climate chamber at controlled temperature and RH. The curing temperature was (25 ± 2) °C, the curing time was three months (long-term curing).

3.4 Indentation test

The specimens described above were subjected to the indentation test in order to obtain the complex shear modulus.

The test equipment is powered by *MTS Material Testing Systems* and ensures a full spectrum of material or component tests. Figure 3.9a describes the load unit assembly and the size of all components (Table 3.13). Figure 3.9b shows the climatic chamber included in the load unit assembly.

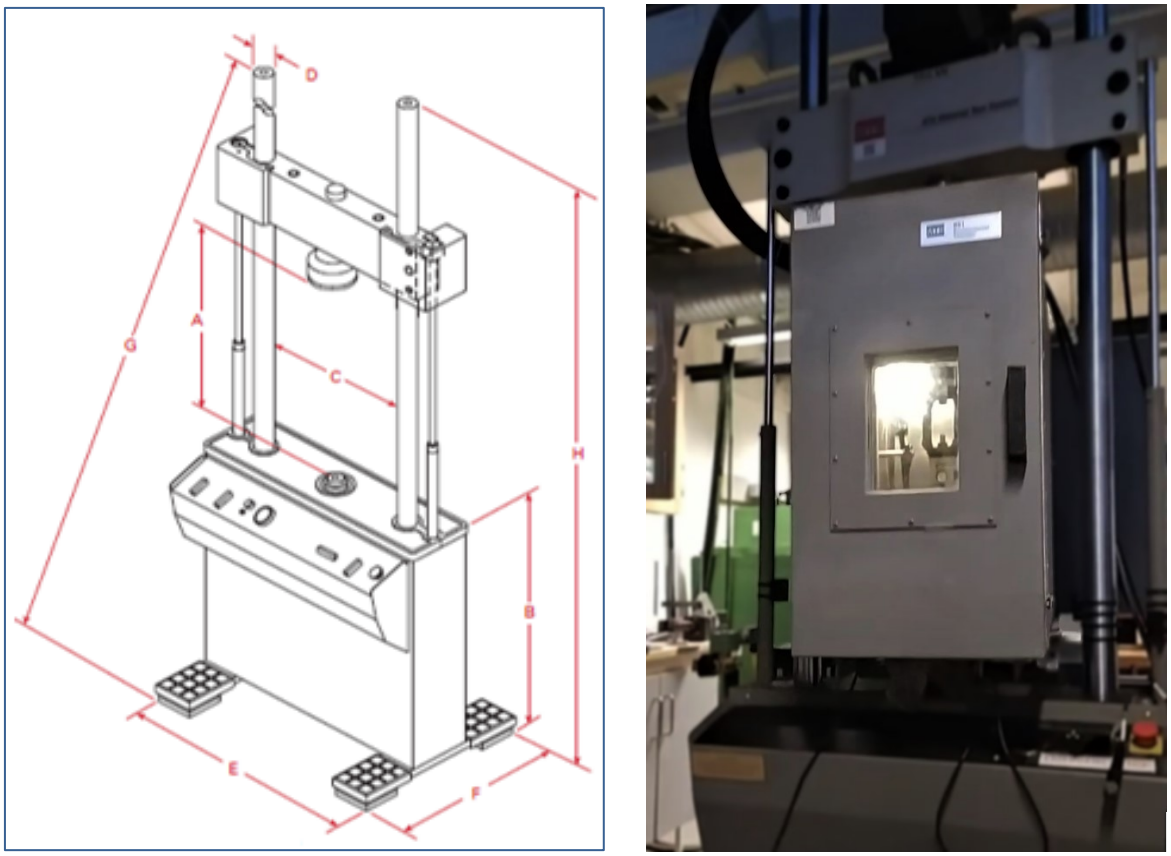

Figure 3.9: a) MTS load unit assembly; b) climatic chamber

Table 3.13:Specifications by Frame Configuration

Load unit specifications

Model	318.10	318.25	318.50
Force capacity (maximum)	100 kN (22 kip)	250 kN (55 kip)	500 kN (110 kip)
Available actuator ratings	15, 25, 50, 100 kN (3.3, 5.5, 11, 22 kip)	100, 250 kN (22, 55 kip)	250, 500 kN (55, 100 kip)
Vertical test space* (A)	1308 mm (51.5 in)	1625 mm (64 in)	2108 mm (83 in)
Working height (B)	889 mm (35 in)	889 mm (35 in)	889 mm (35 in)
Column spacing (C)	533 mm (21 in)	635 mm (25 in)	762 mm (30 in)
Column diameter (D)	64 mm (2.5 in)	76 mm (3 in)	102 mm (4 in)
Base width (E)	864 mm (34 in)	1003 mm (39.5 in)	1245 mm (49 in)
Base depth (F)	610 mm (24 in)	762 mm (30 in)	914 mm (36 in)
Diagonal Clearance (G)	2718 mm (107 in)	3251 mm (128 in)	3835 mm (151 in)
Overall Height (H)	2540 mm (100 in)	3023 mm (119 in)	3581 mm (141 in)
Stiffness†	2.6 x 10^8 N/m (1.5 x 10^6 lb/in)	4.3 x 10^8 N/m (2.4 x 10^6 lb/in)	7.5 x 10^8 N/m (4.3 x 1 10^6 lb/in)
Weight	500 kg (1100 lb)	910 kg (2000 lb)	1770 kg (3900 lb)

The 810 system employs MTS Model 318 load unit assemblies that are force rated up to 500 kN. This floor mounted frame has high axial and lateral stiffness that improves test accuracy and system performance.

The crosshead-mounted load cell provides an accurate force reading for measurement and control. The displacement transducer is integral to the actuator for position measurement and control. In contact with the floor, two isolator pads are placed to dampen external vibrations (15).

Two indenters of different sizes (Fig. 3.10a-b) have been used in order to have two different areas of contact. The contact area radius is related to the indentation depth h by Eq. 2.28, thus obtaining $a = 2{,}52\ mm$ for the small indenter and $a = 6{,}32\ mm$ for the big one.

Figure 3.10: a) big indenter $a = 6.32\ mm$; b) small indenter $a = 2.52\ mm$

Samples preparation

The samples have been cut into two parts to make perfectly flat the surface on which the indenter will act. Before inserting the samples into the climatic chamber, on each half, a grid is drawn ($2\ x\ 2\ cm$) in order to have the adjacent indentations at a distance of at least $10 \cdot a_{max}$ from each other. The grid identifies 9 squares that will correspond to 9 measurements with small indenter (Fig. 3.11).

Each sample has been tested 9 times, indicating each measurement with the alphanumeric code from A1 to C3. When using the large indenter, it is not necessary to draw the grid as less precision is required.

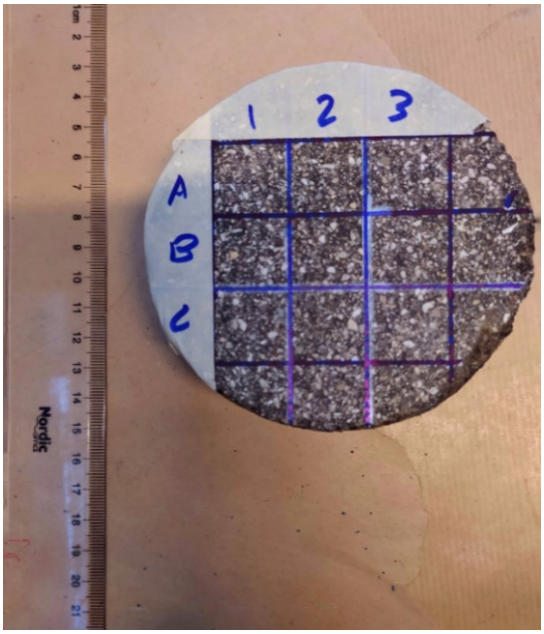

Figure 3.11: Grid 2 x 2 cm for the small indenter

Test procedure

It is possible to enter all the test parameters by a software powered by MTS (displacements, upper and lower limit of the applied force, dwell time, indentation depth etc..) and display them throughout the whole duration of the test.

Specifically, a displacement-controlled load was applied to indenter, reaching a fixed indention depth of 0.4 mm within 1 second. The load was held constant for 200 s, the reaction force $P(t)$ and relaxation graph were continuously recorded (Fig. 3.12a-b-c). A remote control can use to adjust the height of the indenter above the sample, positioned on the lower load cell. (Fig. 3.13)

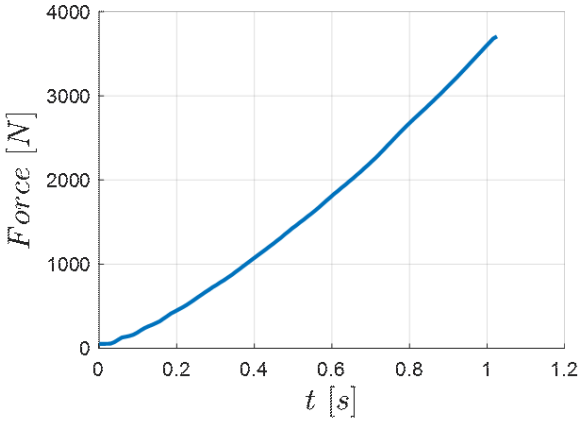
Force [N]
4000
3000
2000
1000
0
0
0.2
0.4
0.6
0.8
1
1.2
t [s]

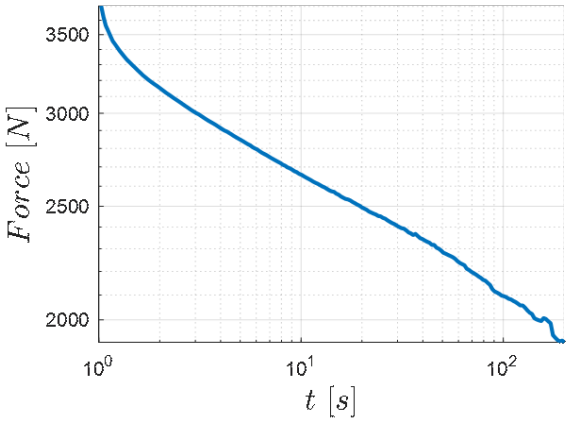
Force [N]
3500
3000
2500
2000
10^0
10^1
10^2
t [s]

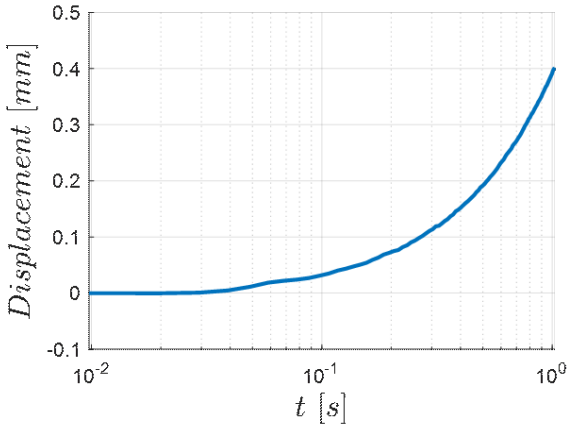
Displacement [mm]
0.5
0.4
0.3
0.2
0.1
0
-0.1
10^-2
10^-1
10^0
t [s]

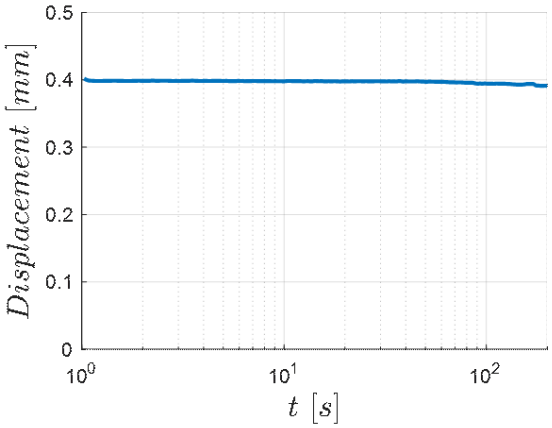
Displacement [mm]
0.5
0.4
0.3
0.2
0.1
0
10^0
10^1
10^2
t [s]

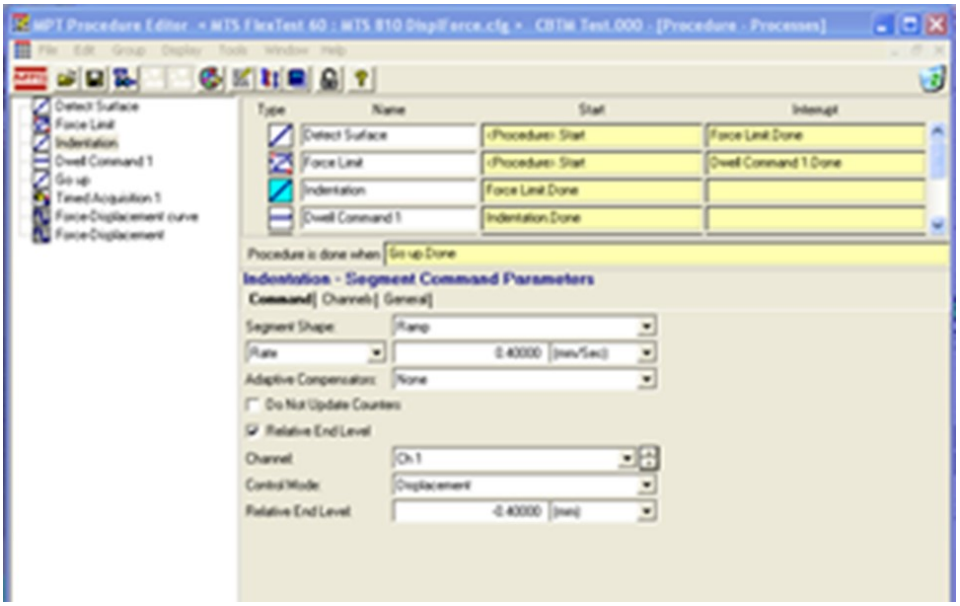
Type
Name
Start
Interrupt
Detect Surface
Force Limit
Indentation
Dwell Command 1
Force Limit Done
Dwell Command 1 Done
Indentation Done
Indentation - Segment Command Parameters
Segment Shape
Ramp
Adaptive Compensation
None
Do Not Update Counters
Relative End Level
Channel
Control Mode
Displacement

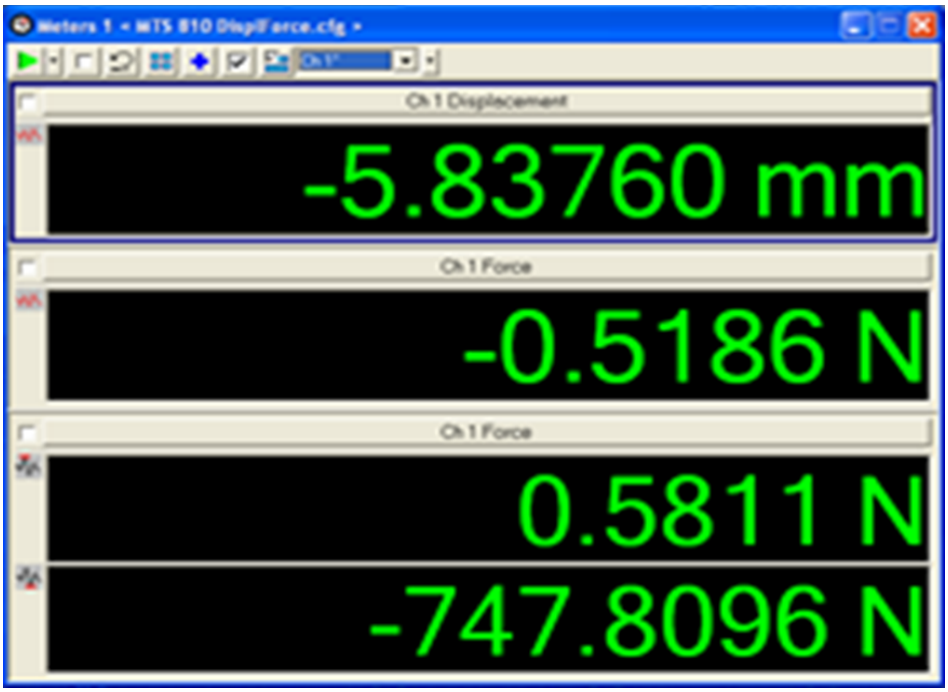

Figure 3.12: a) relaxation curves b) test parameters interface; c) different channels to monitor test parameters

Figure 3.13: sample placed on the lower load cell

3.5 Experimental programme

The experimental programme includes two main phases. The first run was carried out by testing only a part of the total samples available, to give an idea of the order of magnitude of $G(t)$ that would be obtained by testing the CBTMs with the indentation test. It was decided to test the two half of the sample at two different temperatures, 5°C and 25°C, using only the small indenter. the results have been compared with those previously obtained at the "Laboratorio Strade e Trasporti" of DICEA at *Università Politecnica delle Marche.*.

In the second run, tests were completed on the remaining samples at 5°C and 25°C, adding also the temperature of 15°C to facilitate the construction of mastercurves. Only the small indenter has been used so far.

After that, tests was repeated on all samples available at temperatures of 5°C, 15°C, 25 °C using the big indenter, to verify if a different area of contact would influence the value of the $G(t)$, previously obtained with the small one. Table 3.14 summarises the test performed conditions definitively adopted.

.

Table 3.14: test performed conditions

Temperatures	5°C, 15°C, 25°C
Indentation depth	0.4 mm
Dwell time	200 s
Sample's conditioning time	3 hours

The results obtained from the indentation test have been compared with those obtained through cyclic uniaxial compression tests. $E^*(\omega)$ was measured using an AMPT PRO system (Fig. 3.14a-b-c), performed at Laboratory of DICEA at *Università Politecnica delle Marche.*

Tested specimens had 75 mm in diameter. These were obtained by coring 150 and 100 mm SGC specimens of mixtures and mortars, respectively, after long-term curing. The equipment measured the axial stress with a load cell. Three LVDT, placed 120° apart measured the axial strain in the middle part of the specimen, considering a measuring base of 70 mm.

The testing temperatures were 5, 15, 25, 35, 45 and 55 °C. The testing frequencies were 10, 5, 1, 0.5, 0.1 Hz and the target strain amplitude was 30·10-6°mm/mm. 20 loading cycles were applied at each test frequency (7).

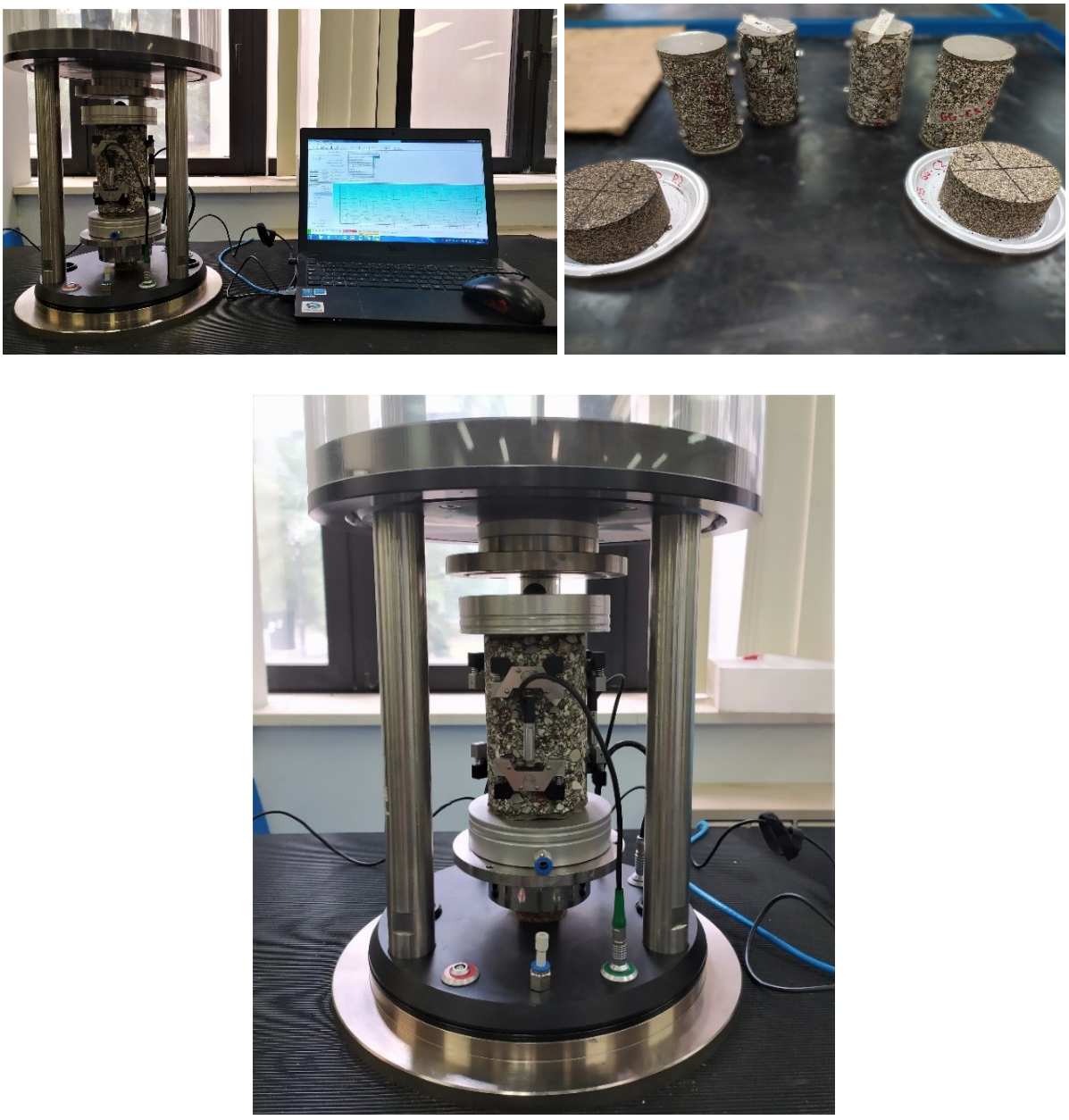

Figure 3.14: a) AMPT PRO device; b) mixtures specimens;

c) testing configuration detail

Each sample, according to its characteristics, has been coded as follow:

- FAM or MIX, based on the mixture or mortar that are being considered;
- CC or GG, according to the type of grading curve (CC corresponds to DG);

- C2 or C3, according to the type of cement involved (C2 corresponds to CSA and C3 corresponds to PSC);
- S1, S2, S3 represent the specimen number;
- 5C, 15C, 25C indicate the test temperature they were subjected;
- Big or small indicate the indenter's size.

Fig. 3.15 shows an example of samples coded as described above:

Figure 3.15: sample named with alphanumerical code

Chapter 4.

Results and analysis

In the final Chapter, it is explained operationally the procedure that, by performing the indentation test and through the theoretical aspects mentioned in Chapter 2, has led to determine $G^*(\omega)$. Then, all the results obtained are reported and commented and some considerations are made regarding the use of this methodology comparing it with the classic complex modulus tests.

4.1 Analysis on one specimen

After completing the test as explained in Chapter 3, the first parameter to be calculated is relaxation modulus $G(t)$. As seen in the integral Equation 2.30, it is a function of $P(t)$ continuously recorded during the test, and $h(t)$ increasing it quickly and linearly for $1\ s$, and then keeping it fixed.

The resolution of the integral is done through a pre-set script of the *Matlab* software. Figure 4.1a presents an example of $G(t)$ measured with indentation tests, measured on FAM mortar, dense graded curve, PSC cement type, performed with the small indenter at temperature of 5 °C (FAM_CC_C3_S2_small_5C) . Figure 4.1b shows the value of $G(t)$ using the small indenter and after $1\ s$, on the surface of the same sample divided into 9 squares,

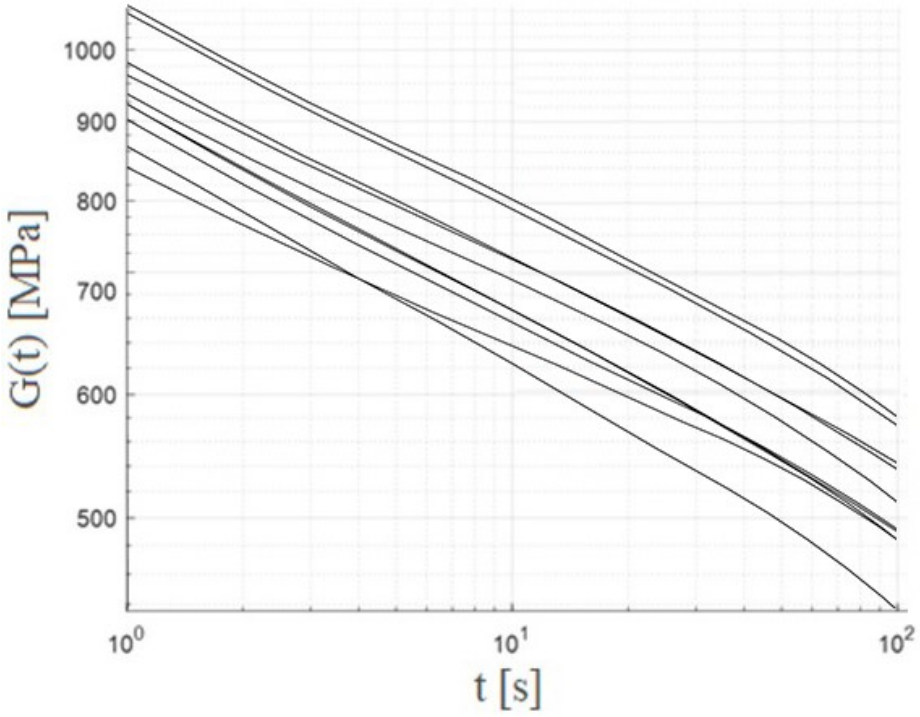

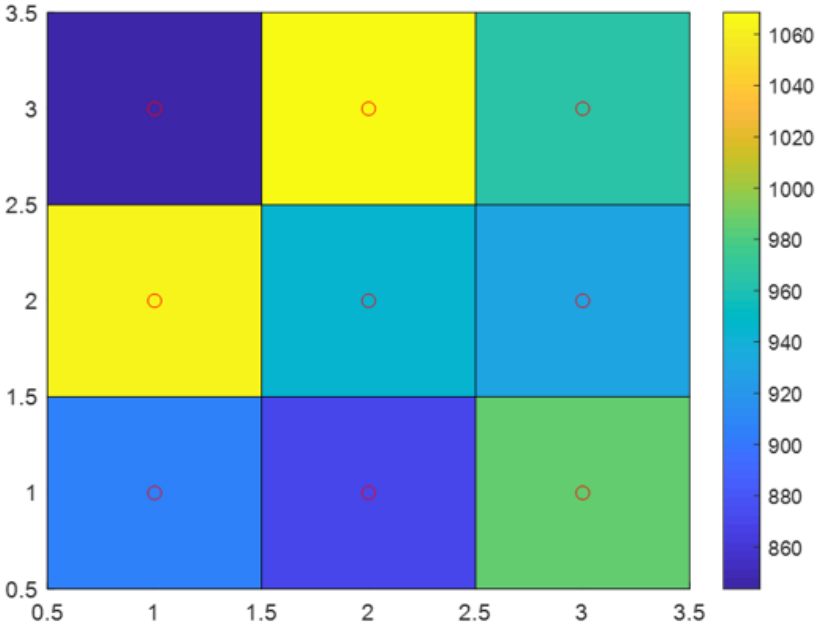

Figure 4.1: a) $G(t)$ *obtained from the indentation tests for the FAM mortar, dense graded curve, PSC cement type, performed with the small indenter at temperature of 5 °C (FAM_CC_C3_S2_small_5C); b)* $G(t = 1\ s)$ *distribution on the surface of sample.*

As can be seen in Figure 4.1, $G(t)$ measured in all the tests decreases with time, following approximately a power-law function. At the same time, the measurements are accompanied by significant scatter (Fig 4.1b), mostly due to the heterogeneity of the material. It can be noticed that the distribution does not follow any specific pattern and is thus caused by random variation of the material composition.

Once the values of $G(t)$ have been obtained, with the aid of another *Matlab* script in which Schapery and Park solution is used, it is possible to derive complex shear modulus $G^*(\omega)$ (Fig. 4.2)

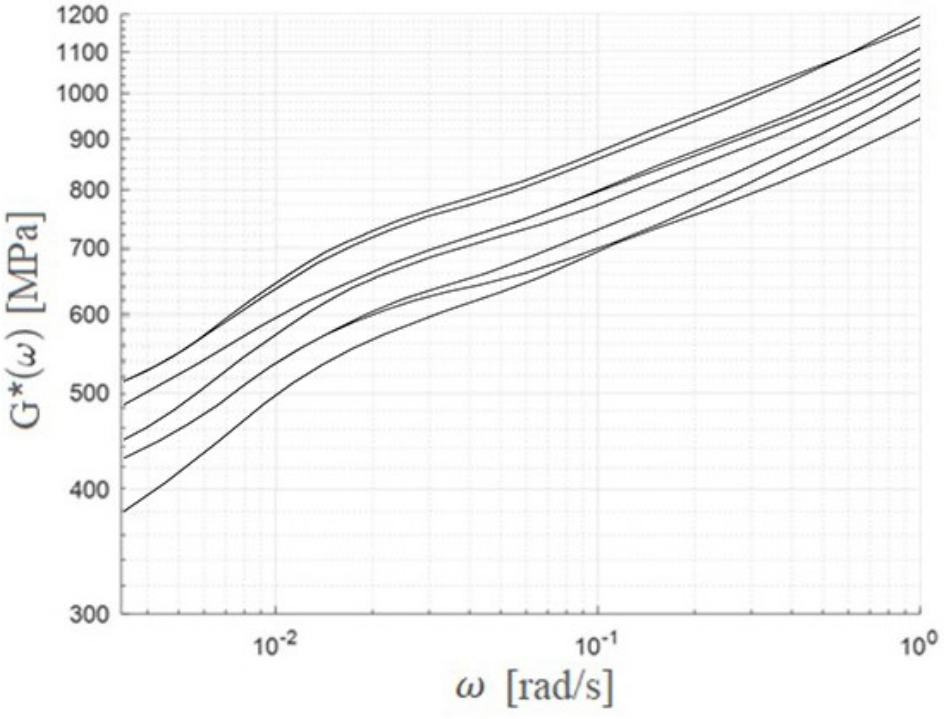

Figure 4.2: $G^*(\omega)$ values

At this point, $G^*(\omega)$ has been converted to the complex Young's modulus E^*, with the assumption of constant Poisson's ratio of 0.35. Figure 4.3 shows the results obtained, highlighting the average value of the 9 measurements.

The error bars represent 95% confidence interval (CI), that is an interval delimited by two limits L_{inf} (lower limit) and L_{sup} (upper limit) that assumes a probability (1- α) of containing the true population mean (where α represents the error probability). The CI

has been calculated in fifteen points on the frequency axis that have been arbitrarily selected.

CI was calculated with the *t*-distribution

$$CI = \bar{X} \pm t^* \frac{s}{\sqrt{n}} \tag{4.1}$$

where:

- $\bar{X}$ is the sample mean;
- t^* is the upper $(1-\alpha)/2$ critical value for the *t*-distribution;
- s is the sample's standard deviation;
- n is the number of measurments.

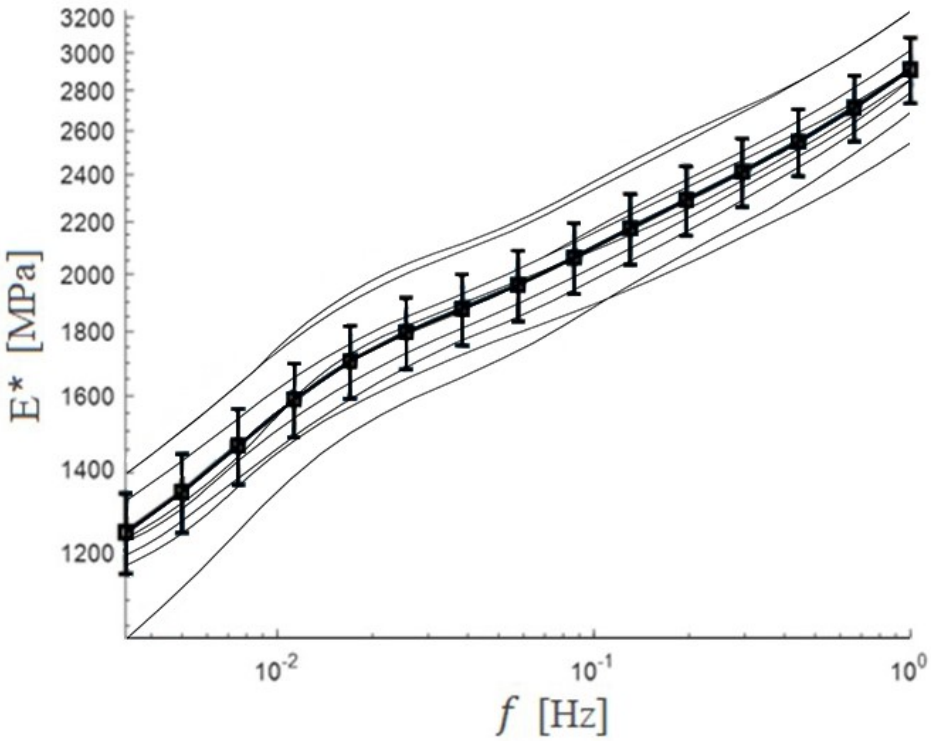

*Figure 4.3: E*values, the black curve refers to the average value of the 9 measurements. Error bars which indicate CI are also reported*

Repeating the same procedure at temperatures of 15 °C and 25 °C, three isothermal curves are constructed, as a function of frequency (Figure 4.4)

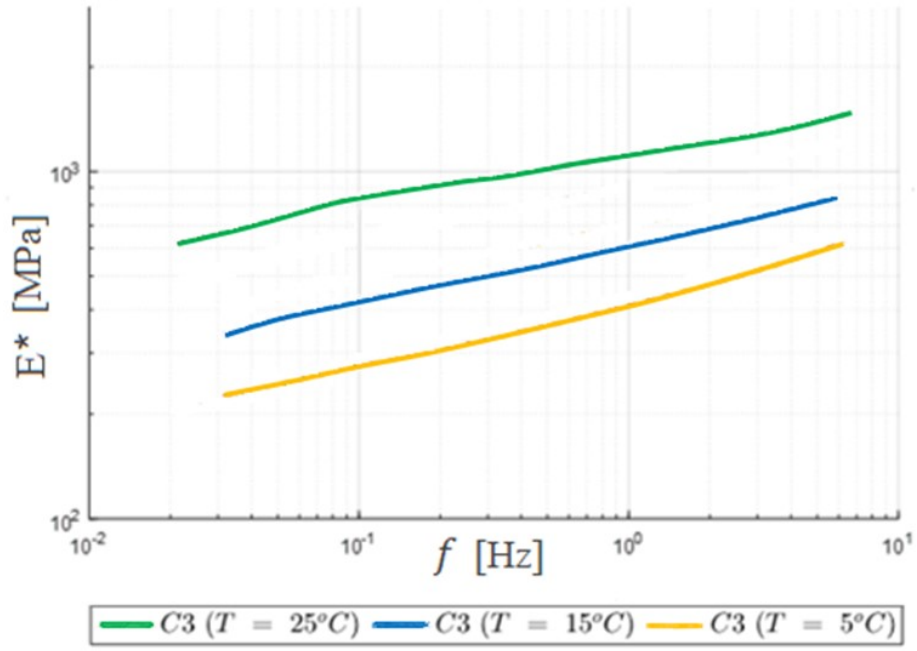

Figure 4.4: Isothermal curves for FAM_CC_C3

Once the isothermal curves have been obtained, it is possible to proceed with the construction of master curves at a given reference temperature, in this case $T_{ref} = 25$ °C.

The construction was carried out using the principle of time-temperature superposition, through the determination of the *shift factors* reported in Table 4.1 according to the empirical relationship of William-Landel-Ferry (WLF) (Fig. 4.5a-b).

Table 4.1: shift factors for CC_C3 material

Shift factors		
5 °C	15 °C	25 °C
2,8387	1,0662	0

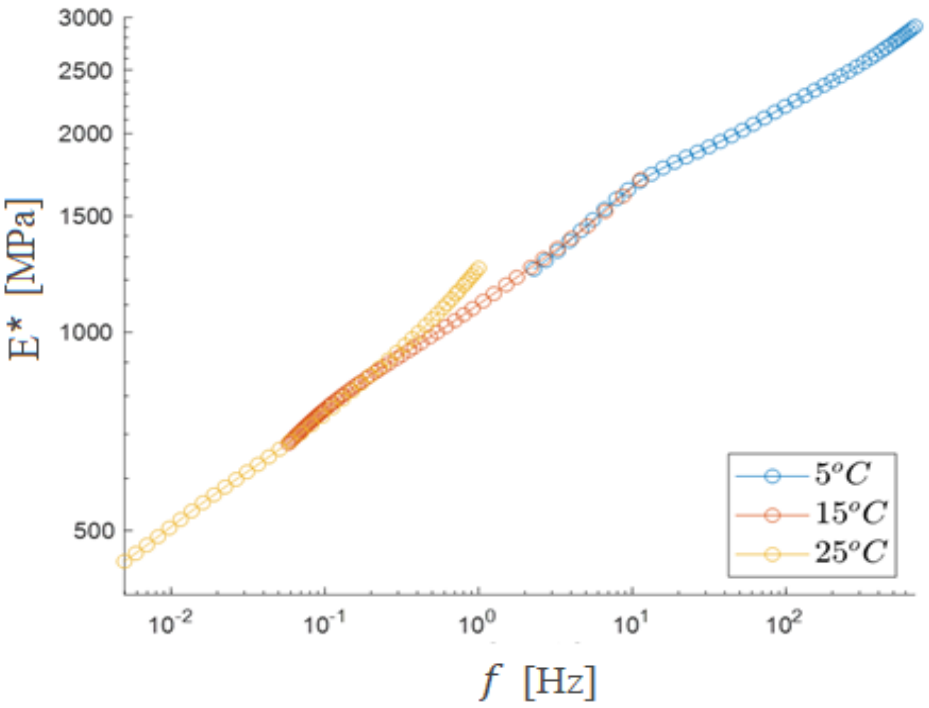

*Figure 4.5: a) Overlapping of E*curves at three temperatures*

To construct the mastercurve in Fig 4.4b, a *Matlab* script has been used, it allows to fit the sigmoidal function, described by the following equation

$$\log(E^*) = \delta + \frac{\alpha}{1 + e^{\beta - \gamma(\log(\omega) + \log(a_T))}} \qquad (4.2)$$

where:

- a_T is the shift factor;
- $\delta, \alpha, \beta, \gamma$ are fitting parameters;
- $\omega = 2\pi f$

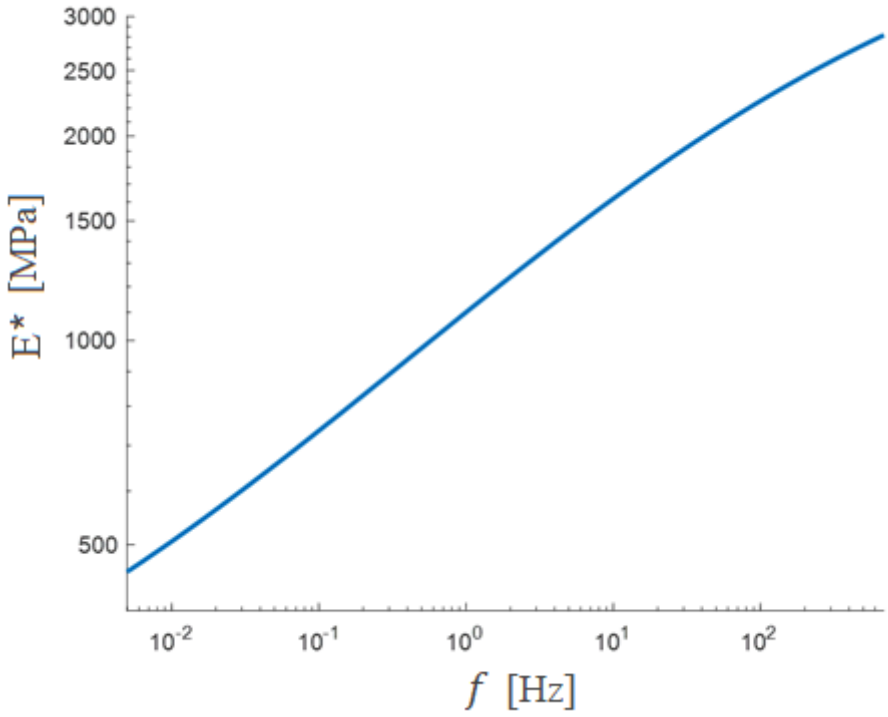

Figure 4.5: b) Master curve of FAM_CC_C3_S2_5C_small

4.2 Preliminary tests

It is necessary to consider two aspects before proceeding with the execution of the indentation test, to be sure that the results obtained are reliable.

4.2.1 Machine compliance

Whenever a testing machine is subjected to a force, the whole system (frame, load cell, grips, couplings, and specimen) experiences some degree of deformation.

To determine the displacement due only to the specimen deformation, machine compliance (deformations associated with the load frame, load cell, and grips) must be considered from this measurement. Note that machine compliance is specific to each system and is dependent on the forces a given system is subjected to (16).

The indentation depth was measured by using the piston's position sensor. The machine compliance was measured in order to calculate the actual indentation depth in this setup.

This has been achieved by removing the steel indenter from the setup and loading the piston of the load frame against the base of the setup. Therefore, it was assumed that all the deformation measured at this arrangement was due to the machine compliance. The measured machine compliance was $0.051\ \mu m/N$.

This arrangement assumes a linear machine compliance that acts as a spring, consequently, the indentation depth was considered to be the difference between the displacement as measured with the piston position and the deformation in the machine at the measured load level.

4.2.2 Linearity check

A linearity tests was carried out on a test specimen at room temperature, using the small indenter. The indentation depth was increased from 0.1 mm to 0.6 mm. At 0.6 mm the measured apparent stiffness appears to decrease.

Therefore, 0.4 mm was chosen as the optimal value between reliable load measurement above the load cell's measurement error and high loads that may introduce non-linear material behaviour, due to the concentrations of stress and strain under the indenter.

4.3 First run testing

The first run test was performed at temperatures of 5 °C and 25 °C, using only the small indenter, on both Mixtures and FAM.

4.3.1 Mixtures

Figure 4.6a-b shows the results obtained for the mixtures in the first run. The mixtures have been grouped according to grading distribution.

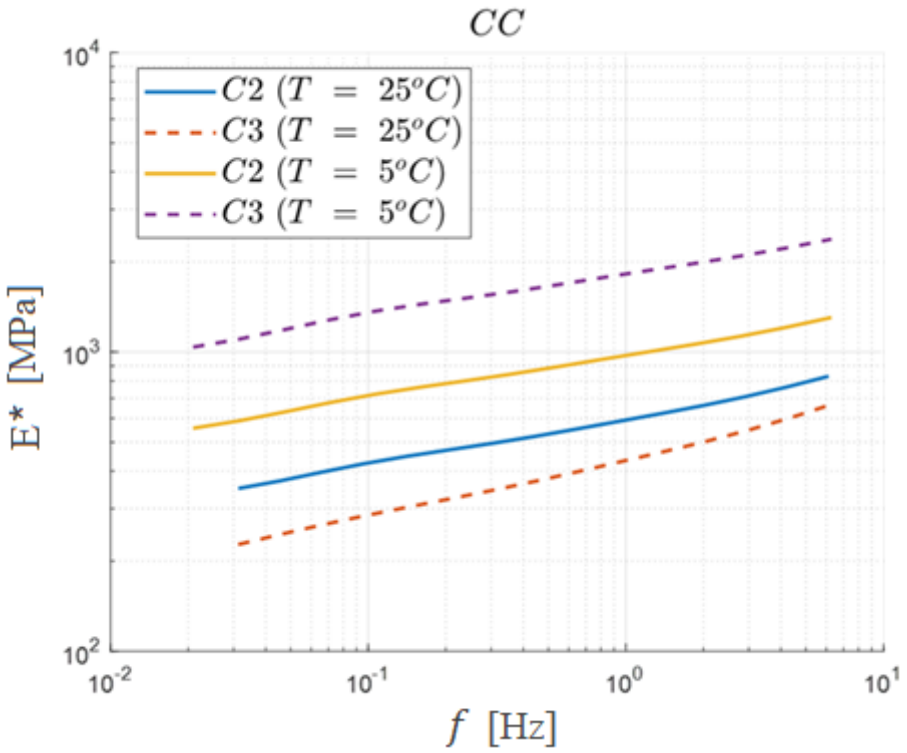
CC
C2 (T = 25°C)
C3 (T = 25°C)
C2 (T = 5°C)
C3 (T = 5°C)
E* [MPa]
f [Hz]
10^4
10^3
10^2
10^-2
10^-1
10^0
10^1

a

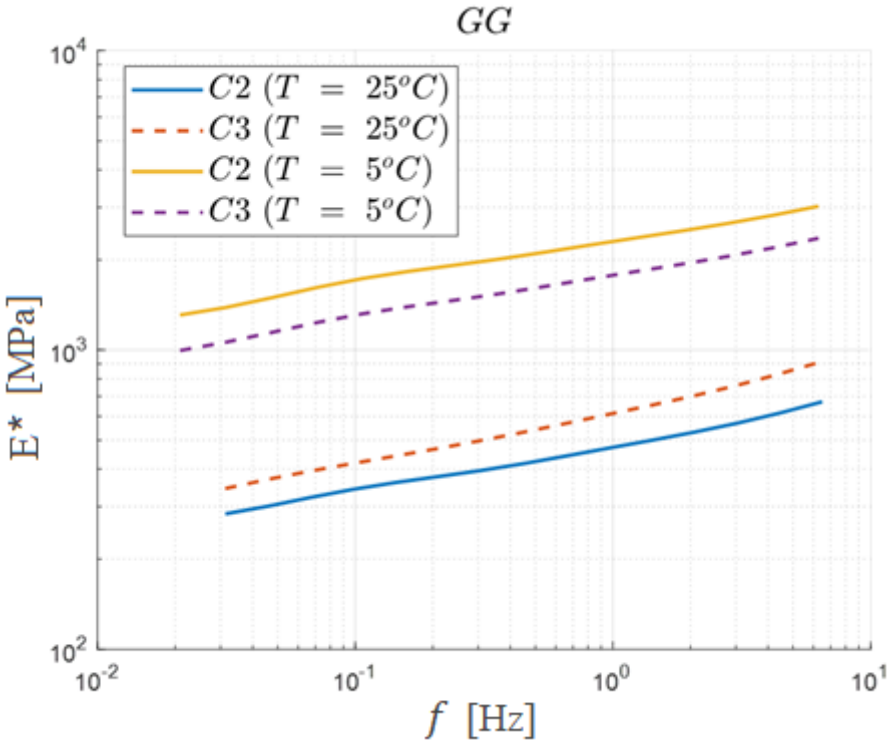

b)

Figure 4.6: Isothermal curves of Mixtures for different types of grading distribution: a) dense graded; b) gap graded

By analysing the results obtained for Mixtures, the results $of\ E^*$ are physically consistent: it increases as the temperature decreases and the frequency increases

4.3.2 FAM

Figure 4.7a-b shows the results obtained for the FAM in conclusion of the first run. The FAM have been grouped according to the type of grading distribution and the following graphs compare the two different types of cement.

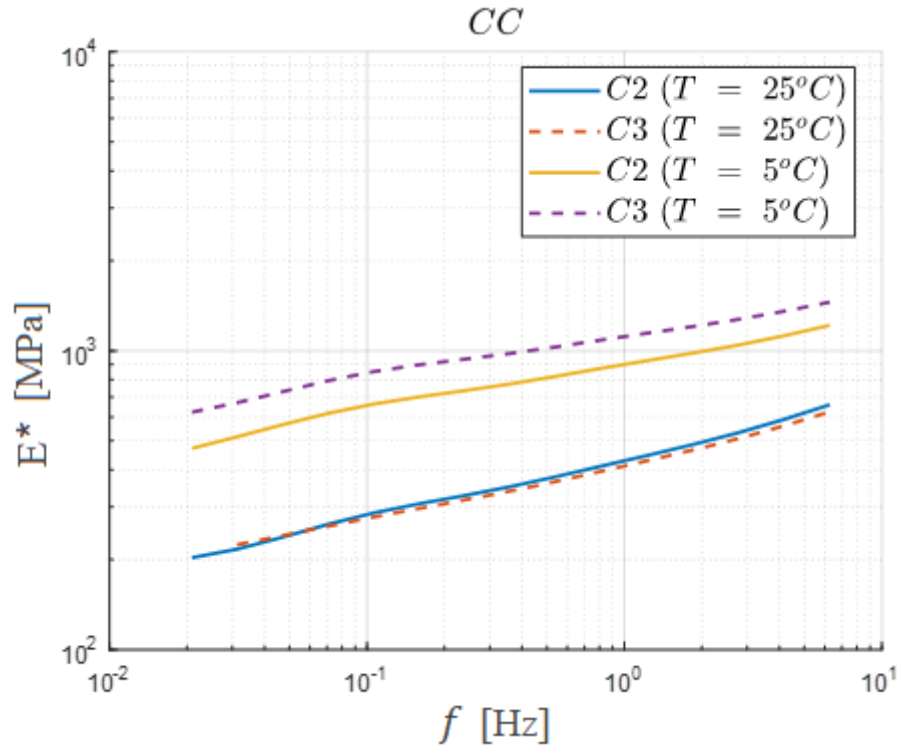
CC
C2 (T = 25°C)
C3 (T = 25°C)
C2 (T = 5°C)
C3 (T = 5°C)
E* [MPa]
f [Hz]
10^4
10^3
10^2
10^-2
10^-1
10^0
10^1

a)

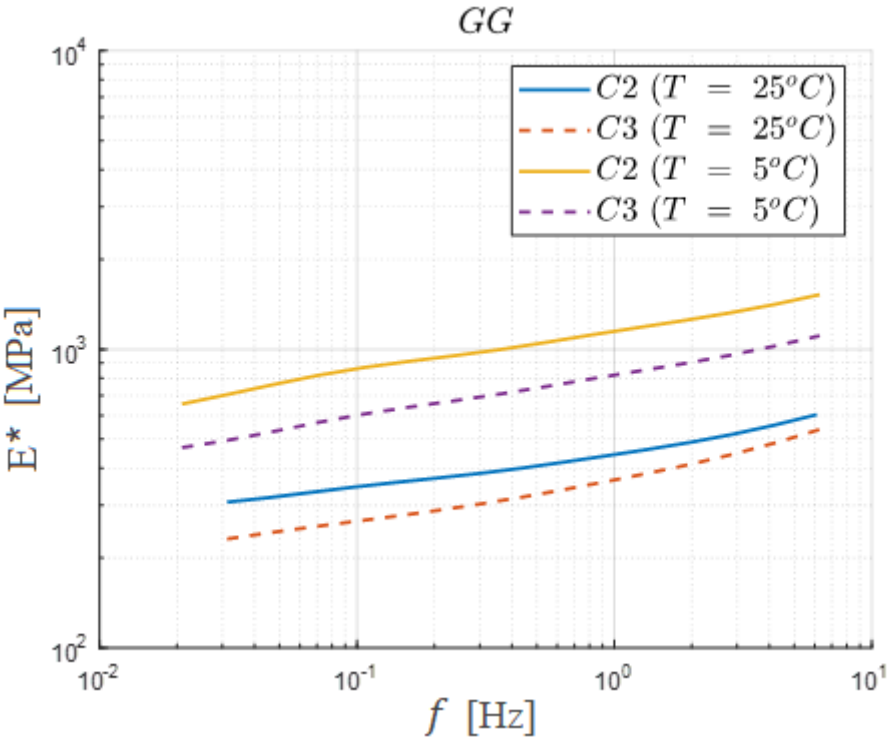
GG
C2 (T = 25°C)
C3 (T = 25°C)
C2 (T = 5°C)
C3 (T = 5°C)
E* [MPa]
f [Hz]
10^4
10^3
10^2
10^-2
10^-1
10^0
10^1

b)

Figure 4.7: Isothermal curves of FAM for different types of grading distribution: a) dense graded; b) gap graded

Also for FAM, the results $of\ \ E^*$ are confirmed physically consistent.

4.3.3 Statistical analysis

A statistical analysis was carried out to verify the dispersion of the measurements obtained with the small indenter on Mixtures and FAM. This has been done on the values of the shear relaxation modulus $G(t)$ at $t = 1$ s.

The Figure 4.8 and 4.9 compare the eight materials investigated in the first run. A box plot representing $G\ (t = 1)$ values is used, reporting the statistical parameters of the Minimum, Maximum, Median, first and third Quartile.

Table 4.2 report the average, the standard deviation and the interquartile range (IQR) of $G(t = 1)$ values.

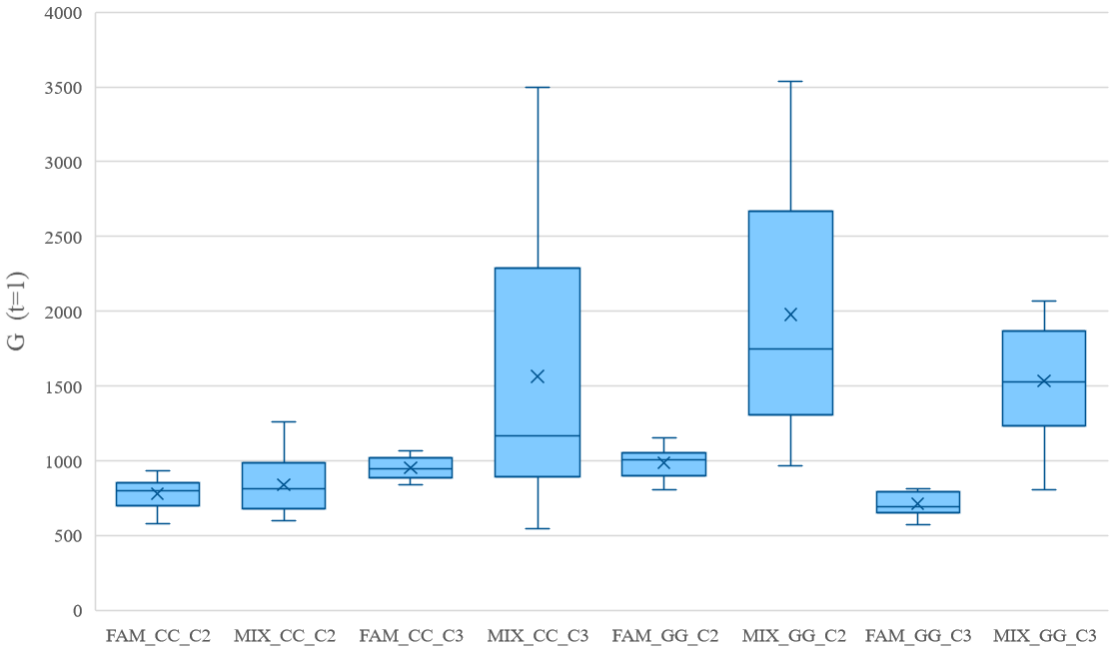

Figure 4.8: box plot representing G(t=1), at temperature of 5 °C, with the small indenter

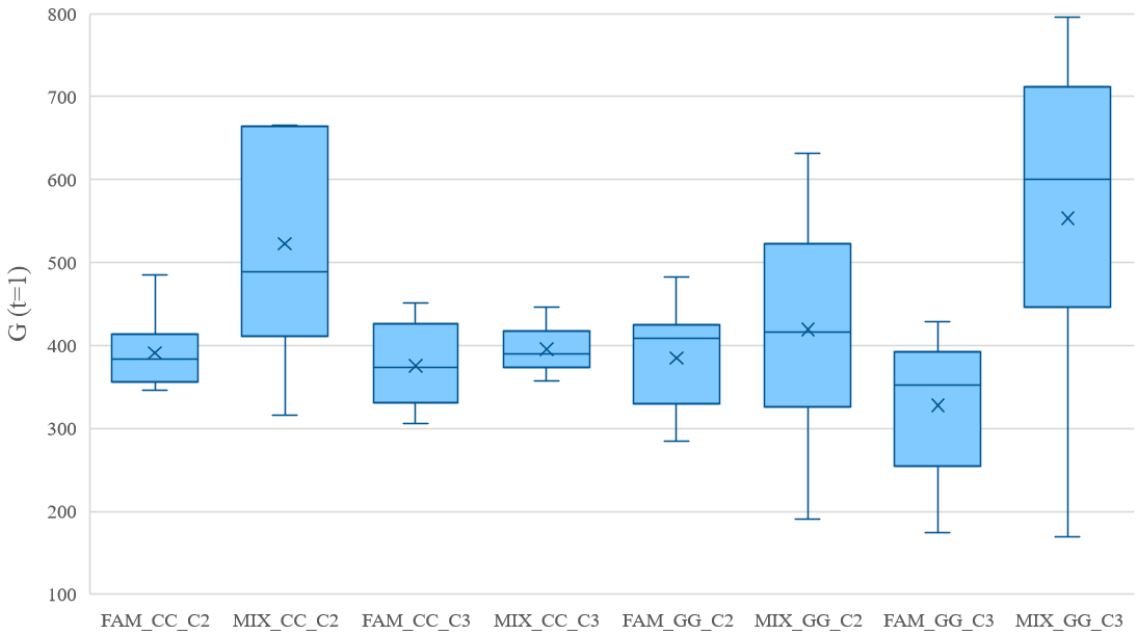

Figure 4.9: box plot representing G(t=1), at temperature of 25 °C, with the small indenter

Table 4.2: statistical parameters of first run testing

	5 °C_small indenter			25 °C_ small indenter		
ID	average	standard dev.	IQR	average	standard dev.	IQR
-	[MPa]	[MPa]	[MPa]	[MPa]	[MPa]	[MPa]
FAM_CC_C2	781	113	155	391	43	57
MIX_CC_C2	840	208	308	523	131	254
FAM_CC_C3	953	78	186	375	51	95
MIX_CC_C3	1564	966	1397	396	28	44
FAM_GG_C2	986	108	153	385	63	96
MIX_GG_C2	1978	858	1363	419	135	198
FAM_GG_C3	712	83	163	328	83	139
MIX_GG_C3	1536	420	637	553	191	266

By analysing the plots of $G\ (t = 1)$ and paying attention to the IQR values, they show a difference between Mixtures and FAM. The mortars have given better results with the small indenter since there is more homogeneity on the same sample: the values of the IQR are lower than that of the corresponding mixture, as shown in the graphs in Figure 4.10a-b.

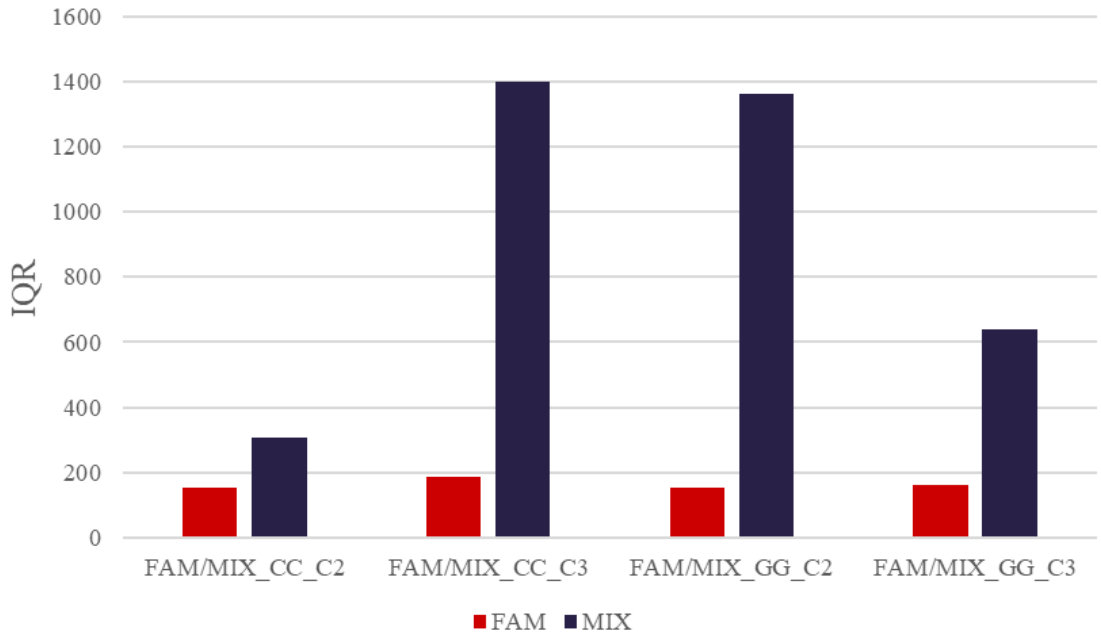

a)

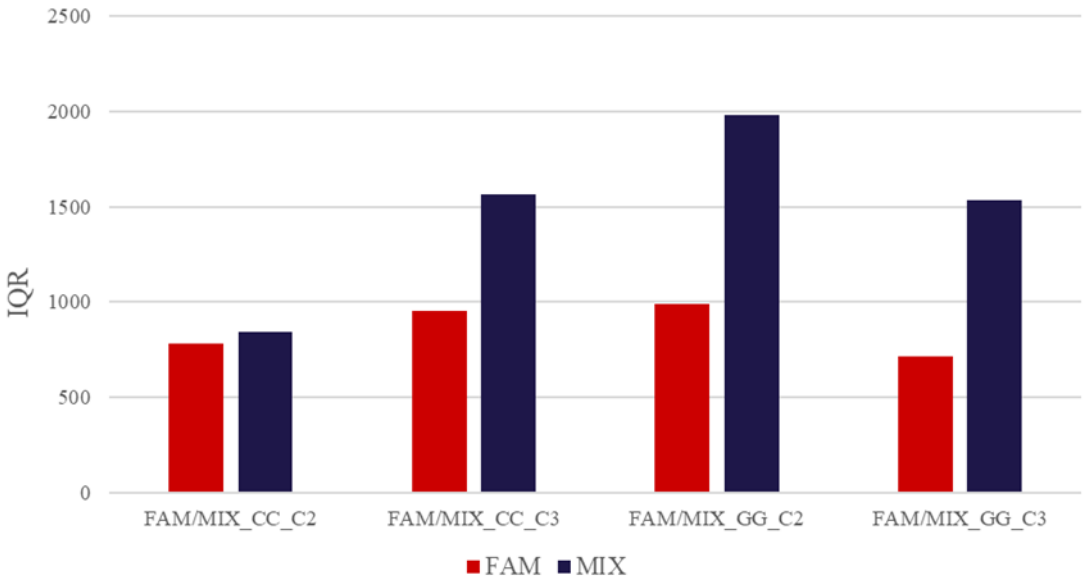

b)

Figure 4.10: a) IQR values for temperatures of 5 °C; b) IQR values for temperatures of 25 °C

From the comparison of the average values of $G\ (t = 1)$ (Fig. 4.11a-b), it can be noted that the value is always higher for the Mixtures than the corresponding FAM. This is due to the fact that in the FAM there is a lack of coarse aggregate while in the mixtures it comes into play giving a higher stiffness to the material.

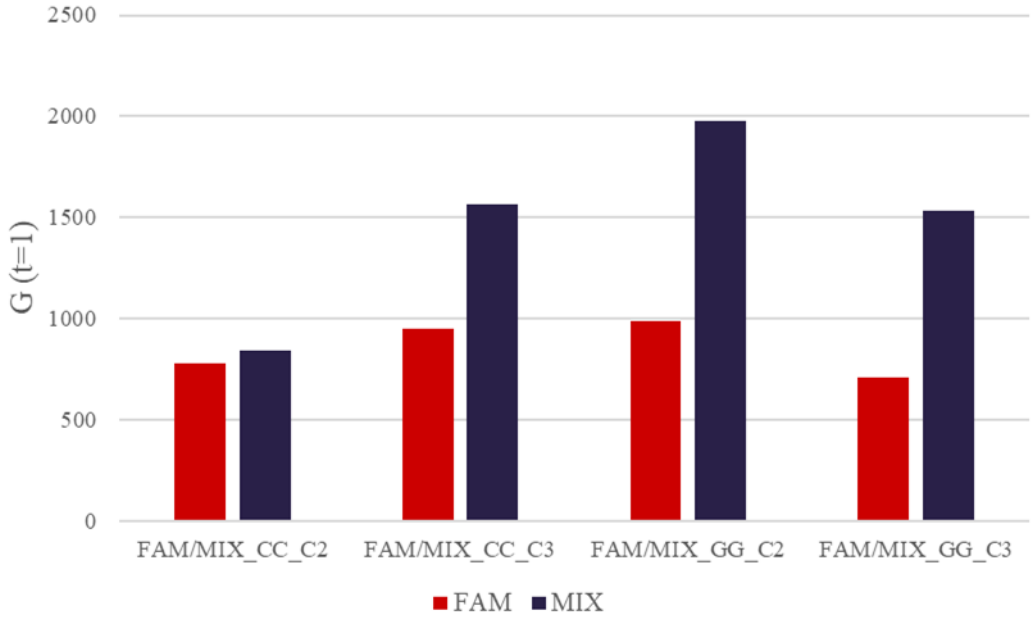

a)

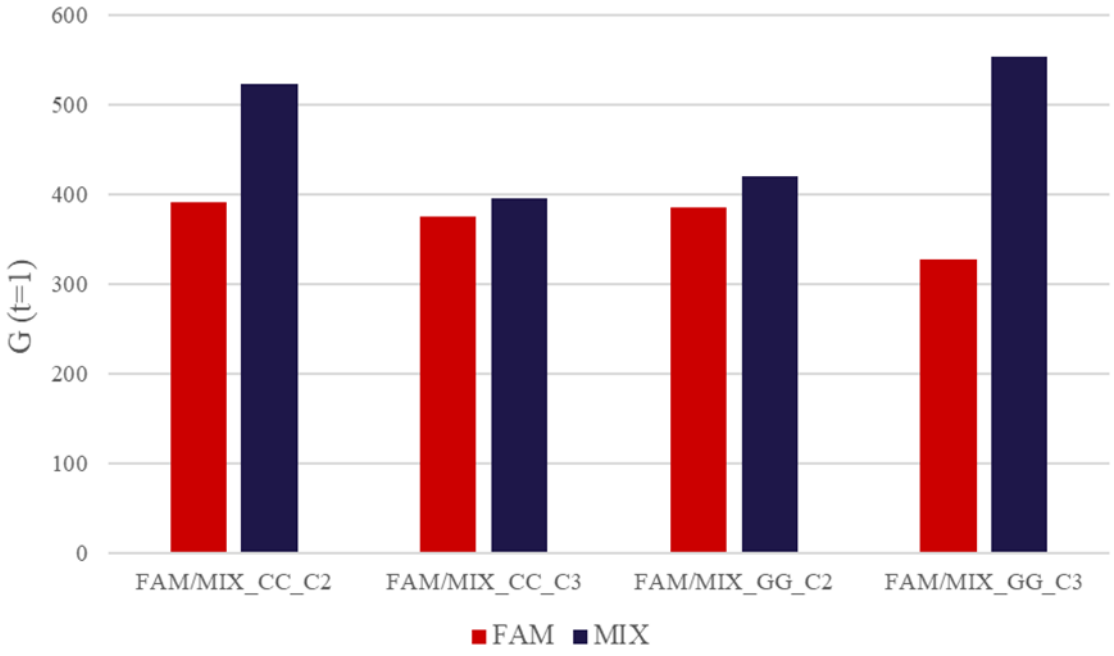

b)

Figure 4.11: a) average of G (t=1) for temperature of 5 °C; b) average of G(t=1) for temperature of 25 °C

Figures 4.12 and 4.13 show the box plots of 95% confidence interval of E^* values.

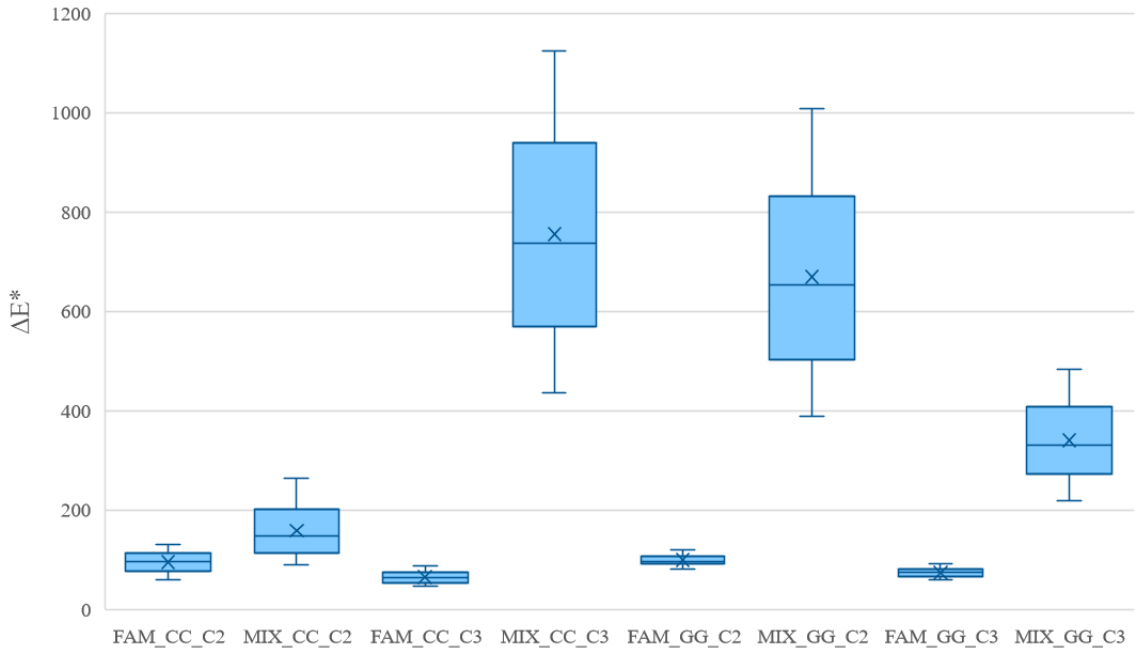

Figure 4.12: box plot representing ΔE values at temperature of 5 °C, with the small indenter*

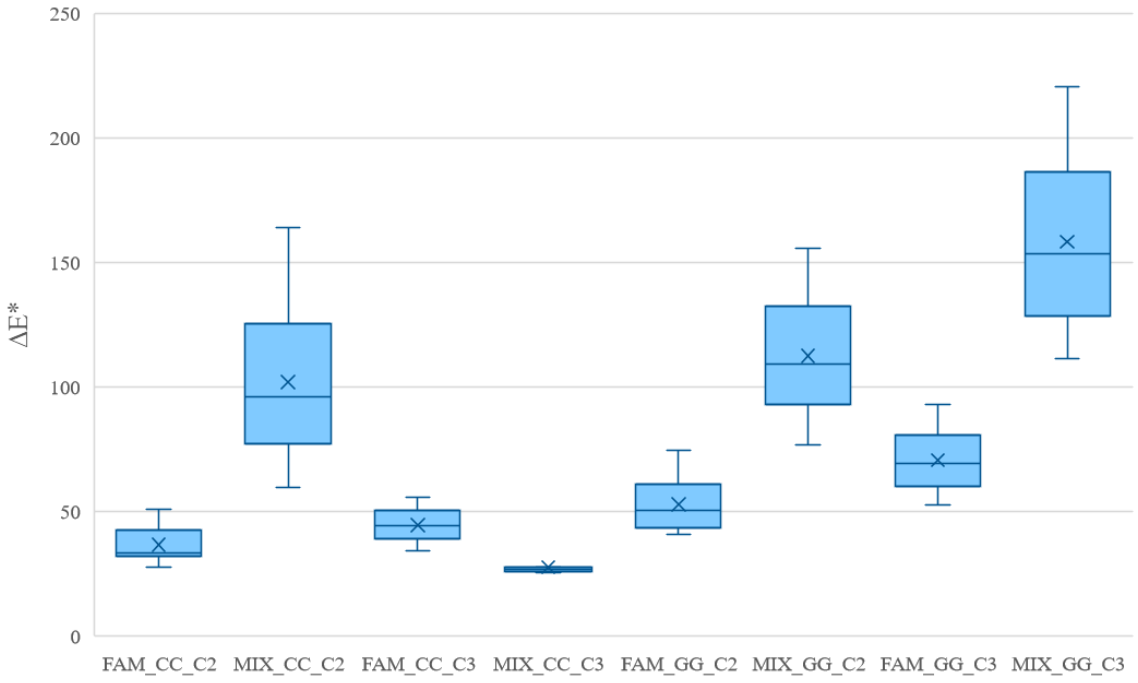

Figure 4.13: box plot representing ΔE values at temperature of 25 °C, with the small indenter*

It follows that the above considerations are confirmed. Although this statistical analysis has been conducted on the values of E^* that, not being directly measured by the test and having been subject to a margin of error given by the application of mathematical models, it is still useful since it represents the whole duration of the test, not only after 1 s.

4.3.4 Summary of first run testing

From the first run, it is clear that the results $of\ \ E^*$ are physically consistent: it increases as the temperature decreases and the frequency increases. However, a variability of the results was noted, so a statistical analysis has been conducted.

By analysing the values for $G(t = 1)$ and 95% CI of the E^* values, the statistical analysis shows that the behaviour described by the small indenter is strongly influenced by the portion of surface involved by the indenter itself, thus being susceptible to the heterogeneity of the samples (as it is also shown in Figure 4.1b) and by the difference between FAM and Mixtures. Thus, the scale effect plays an important role, due to the

presence of the coarse aggregate which has the same order of magnitude as the small indenter.

It has also emerged that the scatter of the FAM values is much smaller than that of the Mixtures, for this reason, from the results obtained at the end of the first run it has been decided to repeat the test with the big indenter.

4.4 Second run testing

The second run tests was performed adding the temperature of 15 °C with the small indenter; then, tests were carried out at temperatures of 5 °C, 15 °C and 25 °C with the big indenter, on both FAM and Mixtures.

4.4.1 Mixtures

Figure 4.14 and 4.15 show the results obtained for the Mixtures in the second run. The Mixtures have been grouped according to grading distribution.

Tables 4.3, 4.4, 4.5, 4.6 report the ID of the samples on which each test was performed.

It is important to specify on which sample the test has been carried out since, when tests are performed on different samples, at the variability already seen in the first run also adds the one due to the difference between different samples.

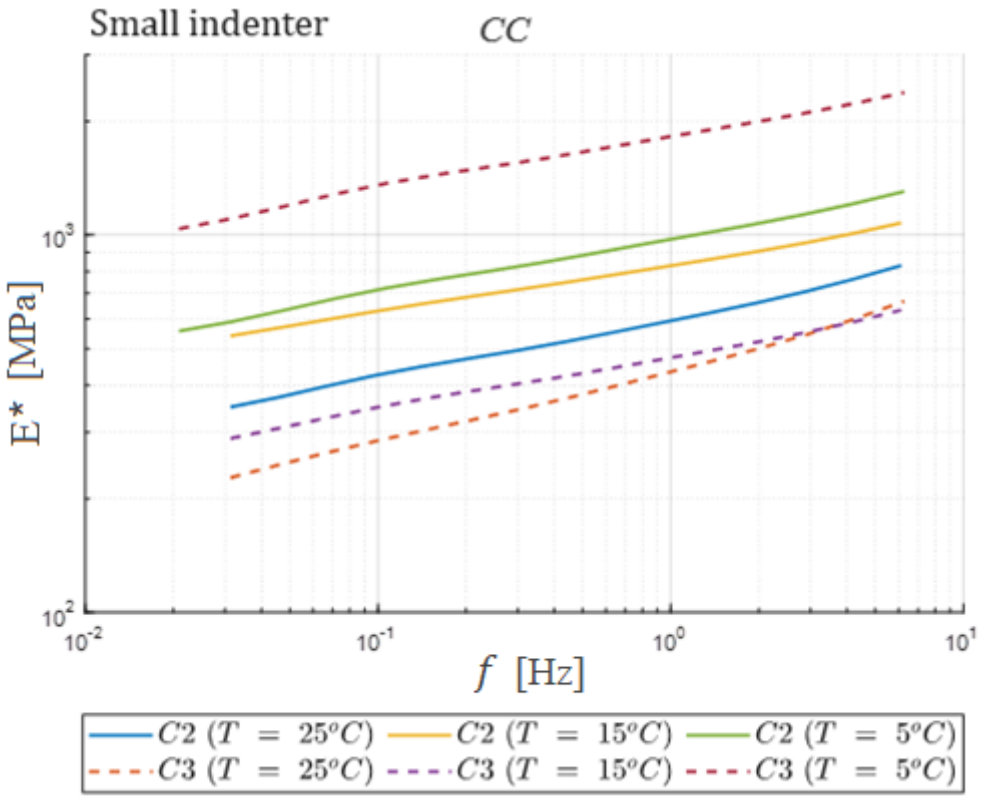

Figure 4.14: Isothermal curves of Mixtures for dense graded distribution and small indenter

Table 4.3: ID of dense graded samples

CC_C2_5 °C	S2	face b
CC_C2_15 °C	S3	
CC_C2_25 °C	S2	face a
CC_C3_5 °C	S1	face a
CC_C3_15 °C	S3	
CC_C3_25 °C	S1	face b

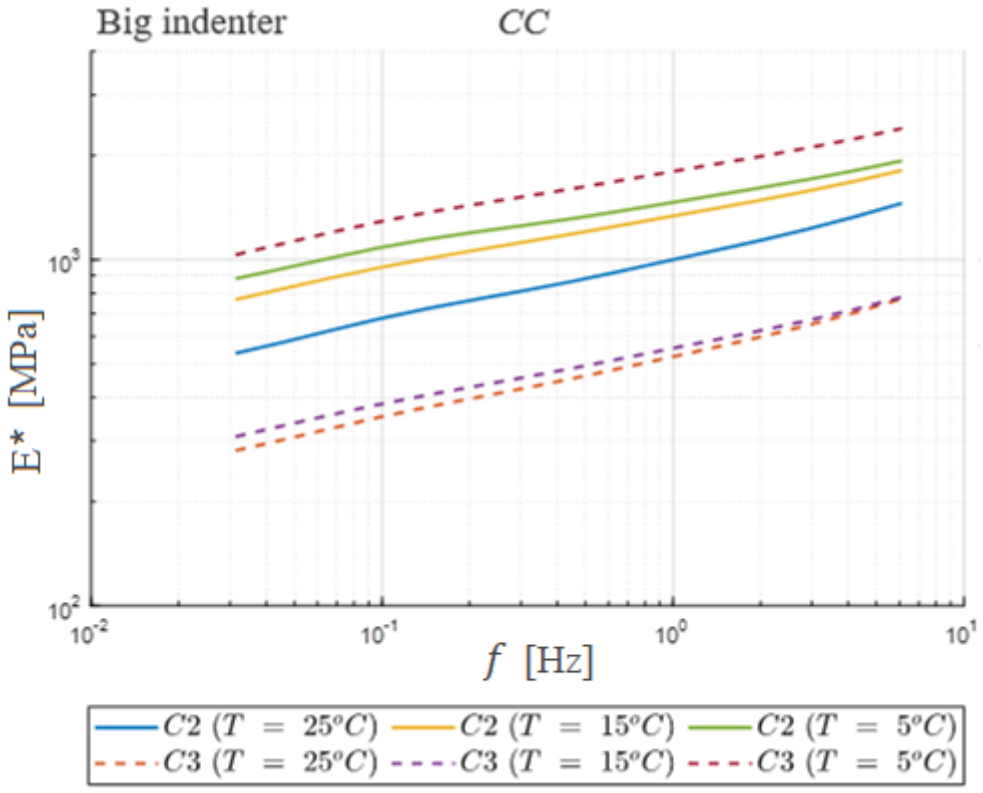

b)

Figure 4.15: Isothermal curves of Mixtures for dense graded distribution and big indenter.

Table 4.4: ID of dense graded samples

CC_C2_5 °C	S1	face b
CC_C2_15 °C	S2	
CC_C2_25 °C	S1	face a
CC_C3_5 °C	S2	face a
CC_C3_15 °C	S2	
CC_C3_25 °C	S2	face b

Figures 4.16 and 4.17 show the results obtained with the same set up but using a gap graded distribution.

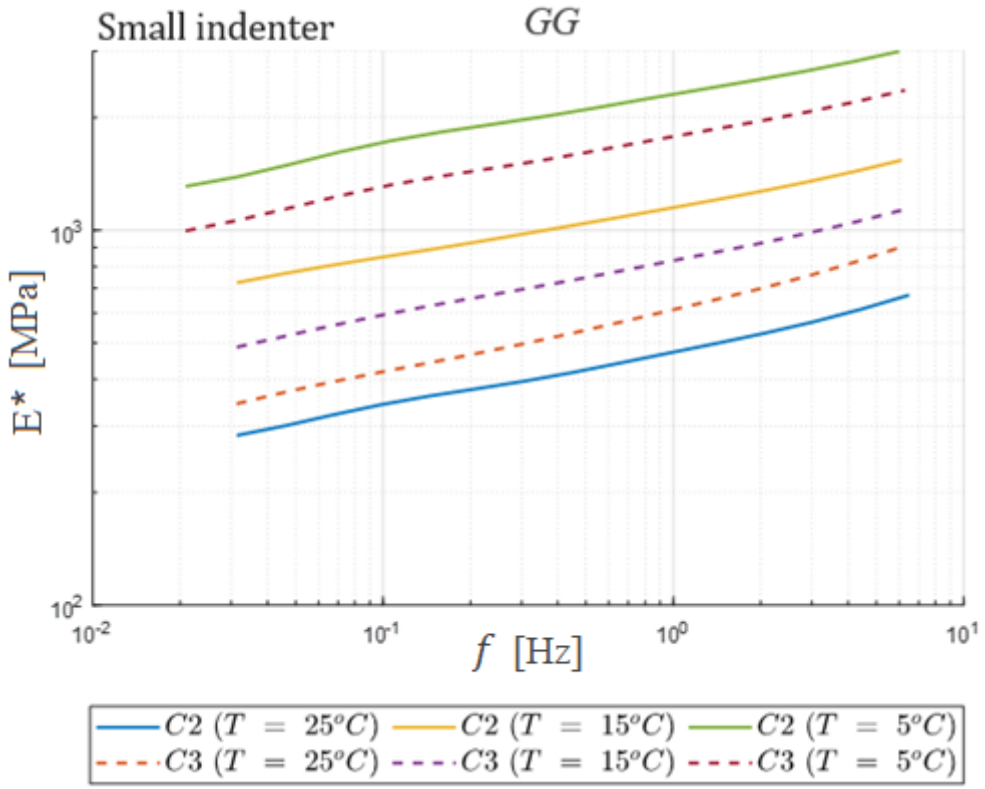

Figure 4.16: Isothermal curves of Mixtures for gap graded distribution: and small indenter.

Table 4.5: ID of gap graded samples

GG_C2_5 °C	S2	face a
GG_C2_15 °C	S3	
GG_C2_25 °C	S2	face b
GG_C3_5 °C	S2	face a
GG_C3_15 °C	S3	
GG_C3_25 °C	S2	face b

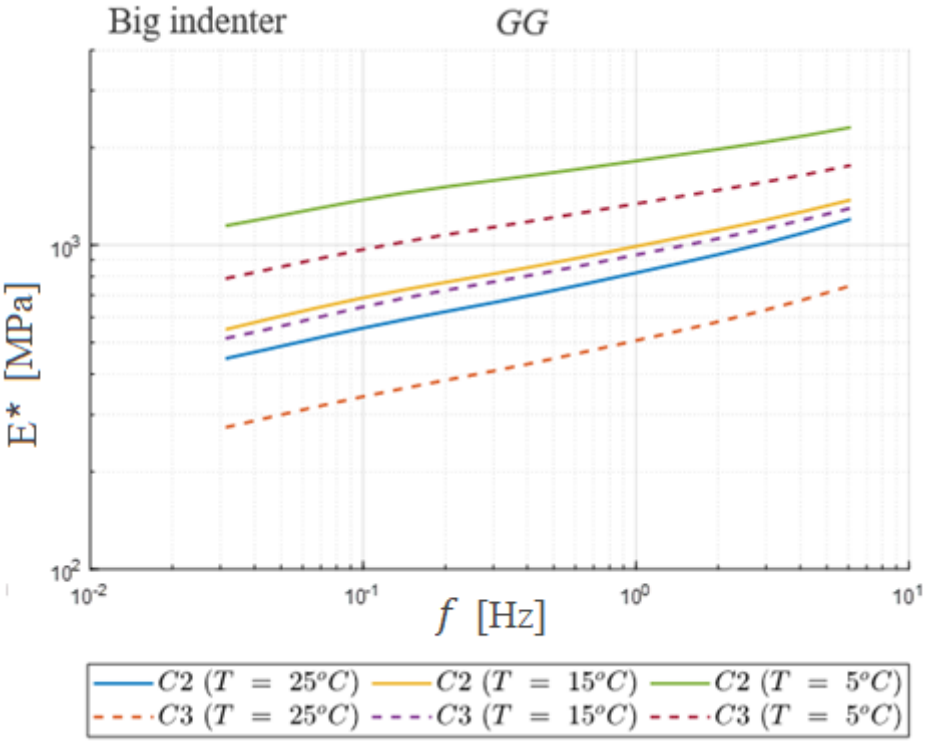

Figure 4.17: Isothermal curves of Mixtures for gap graded distribution and big indenter.

Table 4.6: ID of dense graded samples

GG_C2_5 °C	S1	face a
GG_C2_15 °C	S2	
GG_C2_25 °C	S1	face b
GG_C3_5 °C	S1	face a
GG_C3_15 °C	S2	
GG_C3_25 °C	S1	face b

4.4.2 FAM

Figures 4.18 and 4.19 show the results obtained for the FAM in the second run. The FAM have been grouped according to grading distribution.

Tables 4.7, 4.8, 4.9, 4.10 report the ID of the samples on which each test was conducted.

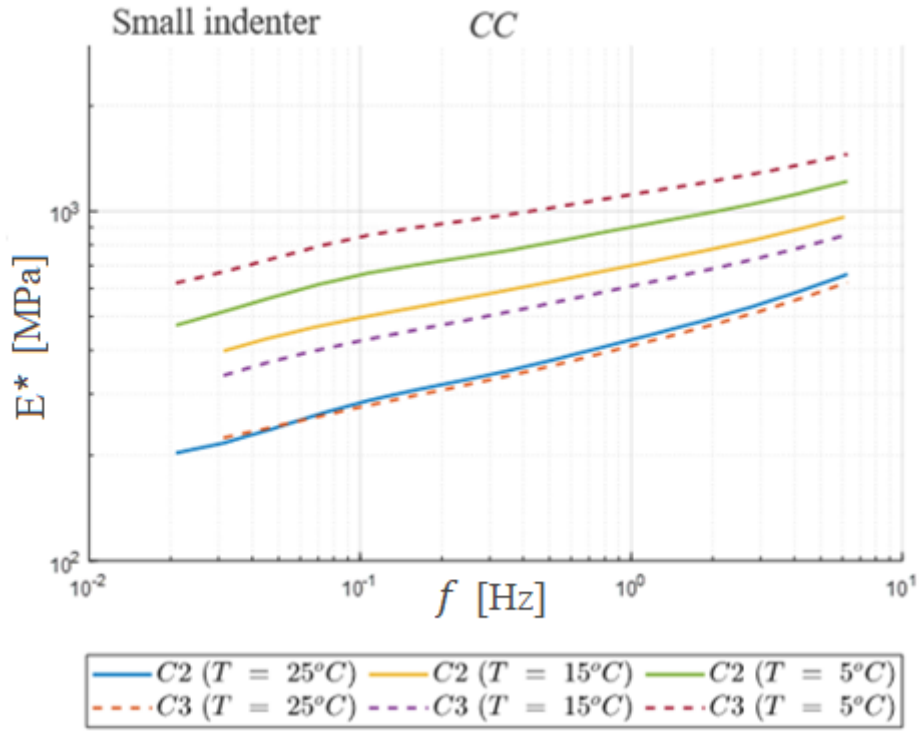

Figure 4.18: Isothermal curves of FAM for dense graded distribution and small indenter.

Table 4.7: ID of dense graded samples

CC_C2_5 °C	S2	face b
CC_C2_15 °C	S3	face c
CC_C2_25 °C	S2	face a
CC_C3_5 °C	S1	face a
CC_C3_15 °C	S3	face c
CC_C3_25 °C	S1	face b

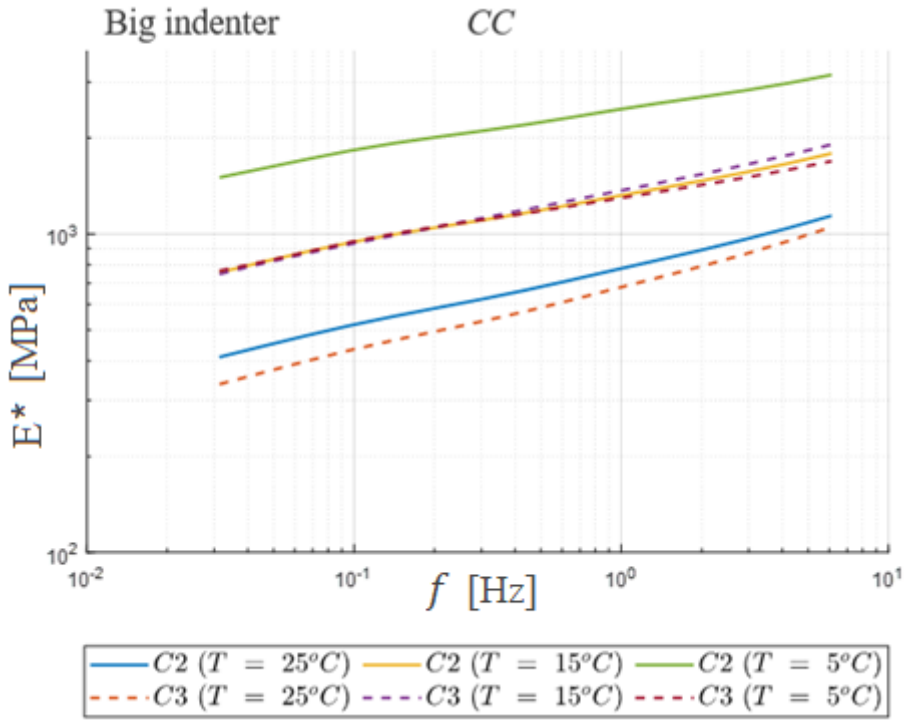

Figure 4.19: Isothermal curves of FAM for dense graded distribution and big indenter.

Table 4.8: ID of dense graded samples

CC_C2_5 °C	S1	
CC_C2_15 °C	S3	face d
CC_C2_25 °C	S3	
CC_C3_5 °C	S1	
CC_C3_15 °C	S3	face d
CC_C3_25 °C	S3	

Figures 4.20 and 4.21 show the results obtained with the same set up but using a gap graded distribution.

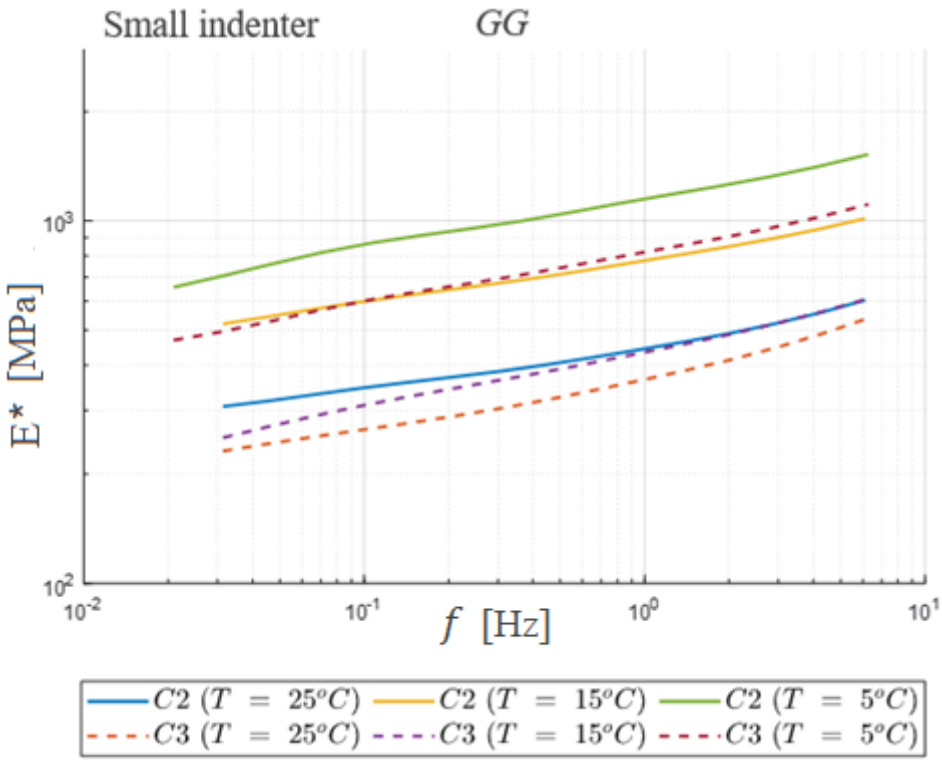

Figure 4.20: Isothermal curves of FAM for gap graded distribution and small indenter.

Table 4.9: ID of gap graded samples

GG_C2_5 °C	S2	face a
GG_C2_15 °C	S3	face c
GG_C2_25 °C	S2	face b
GG_C3_5 °C	S2	face a
GG_C3_15 °C	S3	face c
GG_C3_25 °C	S2	face b

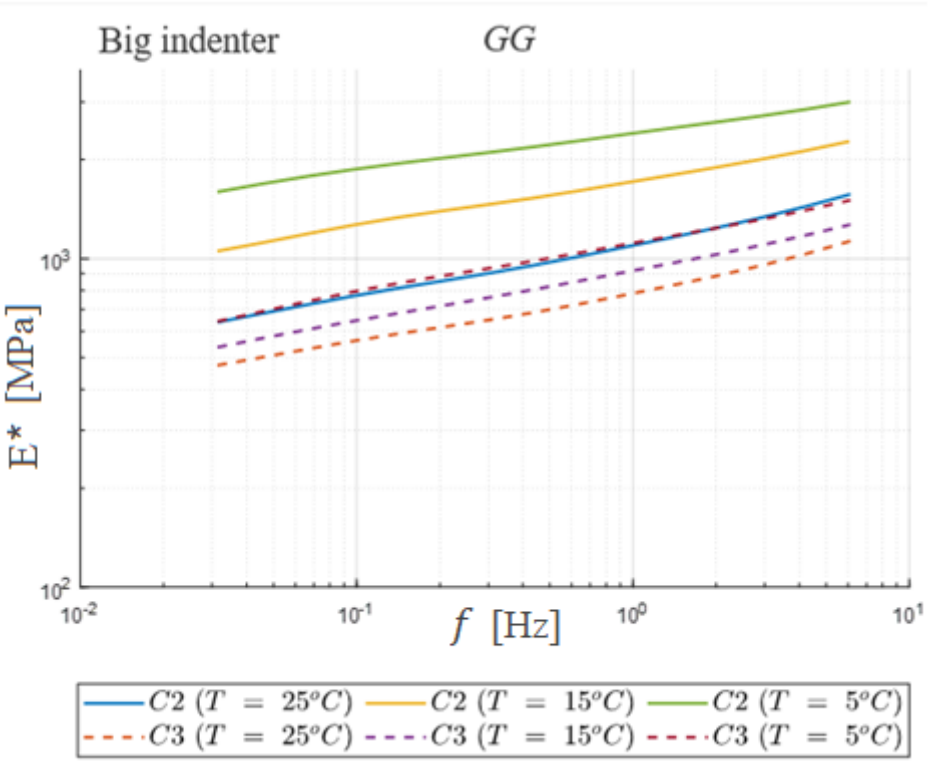

Figure 4.21: Isothermal curves of FAM for gap graded distribution and big indenter.

Table 4.10: ID of gap graded samples

GG_C2_5 °C	S1	
GG_C2_15 °C	S3	face d
GG_C2_25 °C	S3	
GG_C3_5 °C	S2	
GG_C3_15 °C	S3	face d
GG_C3_25 °C	S3	

4.4.3 Statistical analysis

A statistical analysis was carried out in the second run, using the results obtained with the big indenter (6.32 mm) at temperatures of 5 °C, 15 °C and 25 °C.

Figure 4.22, 4.23 and 4.24 show the box plot using the same procedure described for the first run tests. Table 4.11 reports the average, the standard deviation and the interquartile range of $G(t = 1)$ values.

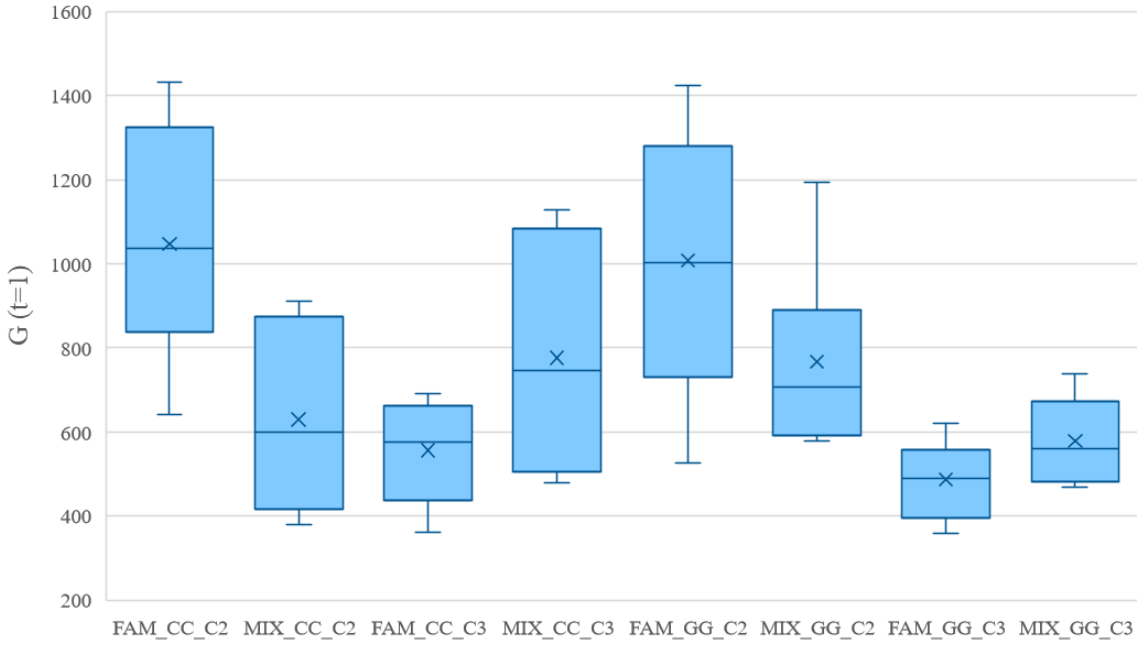

Figure 4.22: box plot representing G(t=1)values at temperature of 5 °C and using the big indenter

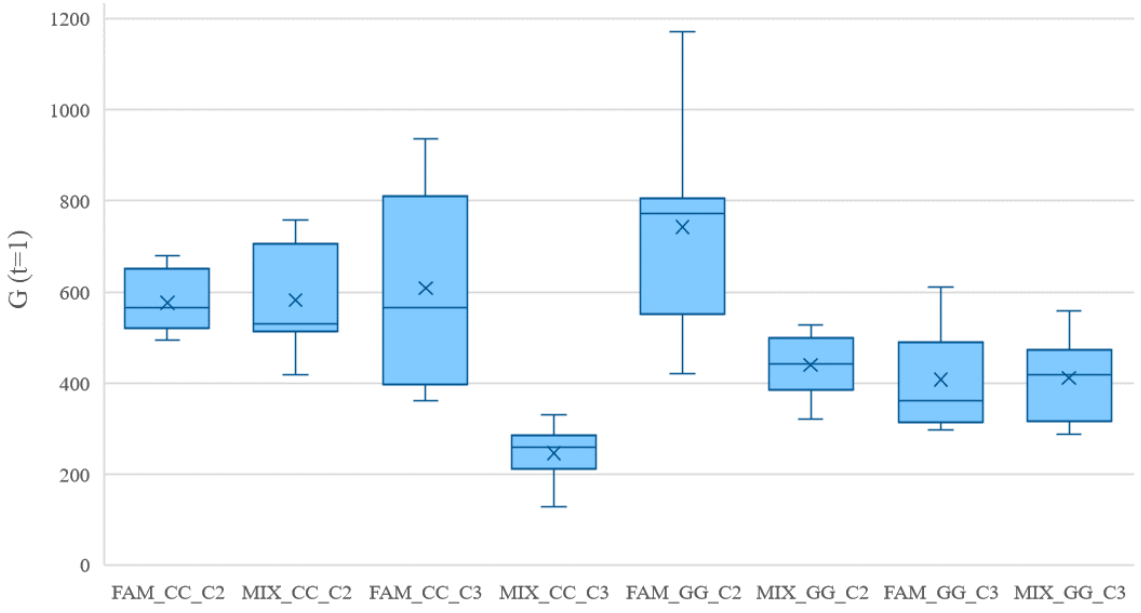

Figure 4.23: box plot representing G(t=1) values at temperature of 15 °C, with the big indenter

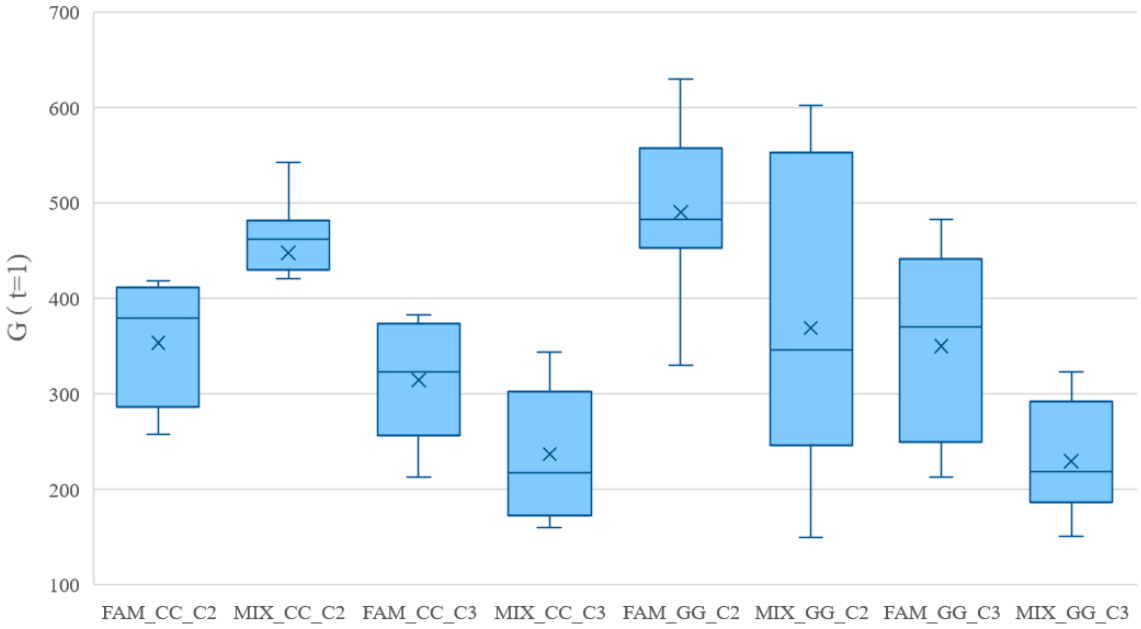

Figure 4.24: box plot representing G(t=1) values at temperature of 25 °C, with the big indenter

Table 4.11: statistical parameters of second run testing

	5 °C_big indenter			15 °C_big indenter			25 °C_big indenter		
ID	average	standard dev.	IQR	average	standard dev.	IQR	average	standard dev.	IQR
-	[MPa]	[MPa]	[MPa]	[MPa]	[MPa]	[MPa]	[MPa]	[MPa]	[MPa]
FAM_CC_C2	1048	276	488	577	68	130	354	66	125
MIX_CC_C2	630	226	458	582	119	176	447	76	50
FAM_CC_C3	557	124	226	608	223	413	314	63	117
MIX_CC_C3	777	276	578	246	61	72	237	69	129
FAM_GG_C2	1007	313	349	743	225	255	490	89	105
MIX_GG_C2	767	210	299	440	69	115	369	165	308
FAM_GG_C3	487	91	164	408	110	176	350	100	192
MIX_GG_C3	579	105	185	412	92	158	230	60	105

The following plots in Figure 4.25 a-b-c, and 4.26a-b-c show a comparison of the values of $G(t = 1)$ and IQR.

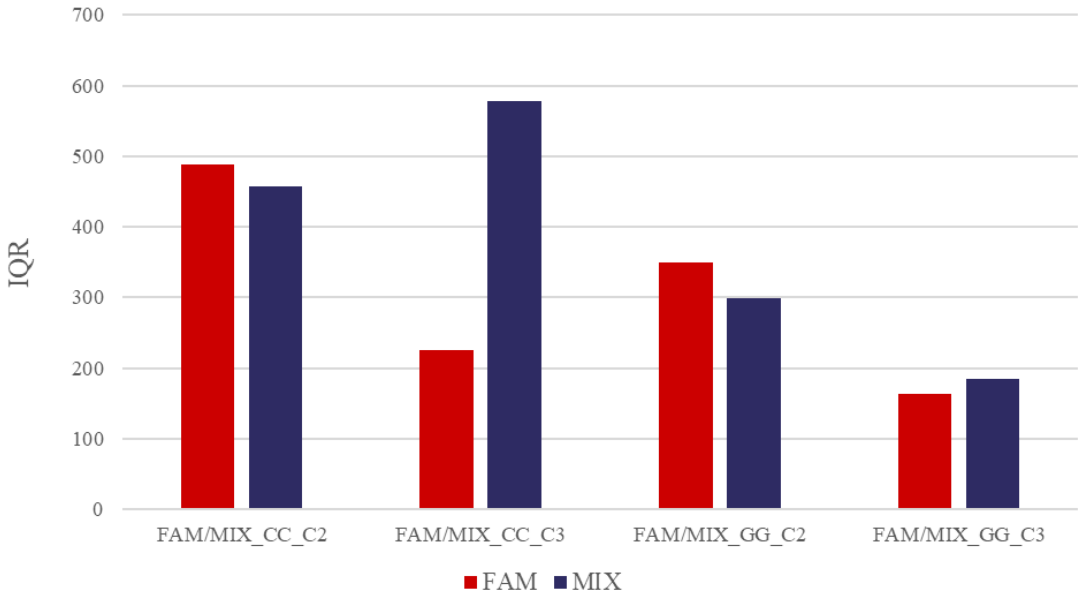
700
600
500
400
300
200
100
0
IQR
FAM/MIX_CC_C2
FAM/MIX_CC_C3
FAM/MIX_GG_C2
FAM/MIX_GG_C3
FAM
MIX

a)

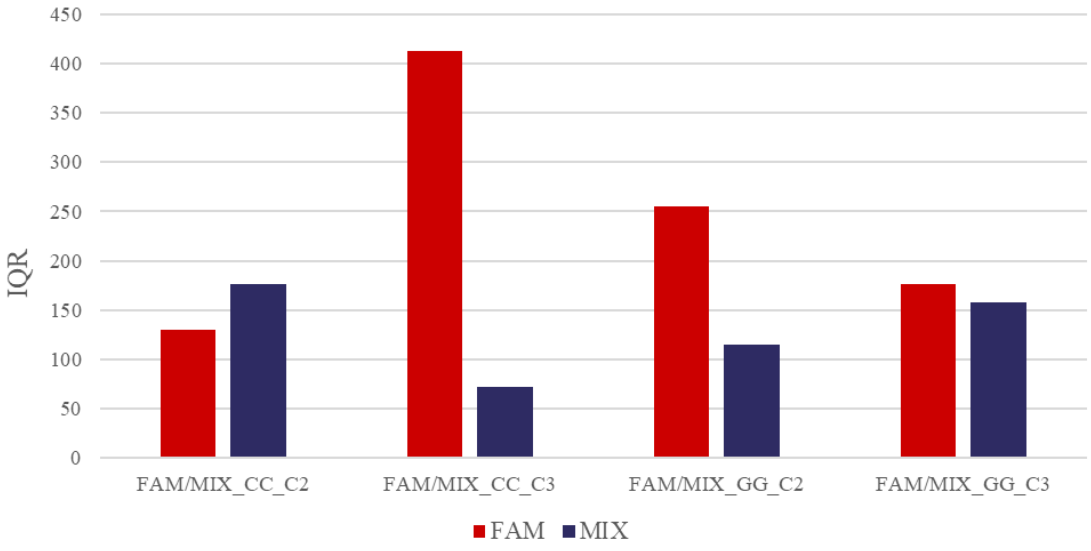
450
400
350
300
250
200
150
100
50
0
IQR
FAM/MIX_CC_C2
FAM/MIX_CC_C3
FAM/MIX_GG_C2
FAM/MIX_GG_C3
FAM
MIX

b)

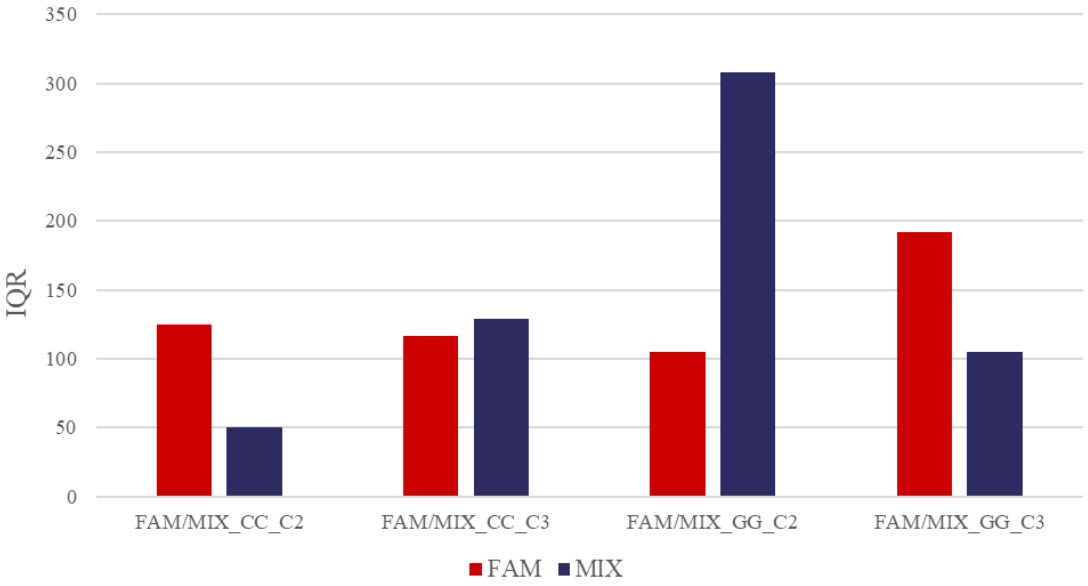

c)

Figure 4.25: IQR values: a) temperature of 5 °C; b) temperature of 15 °C; c) temperature of 25 °C

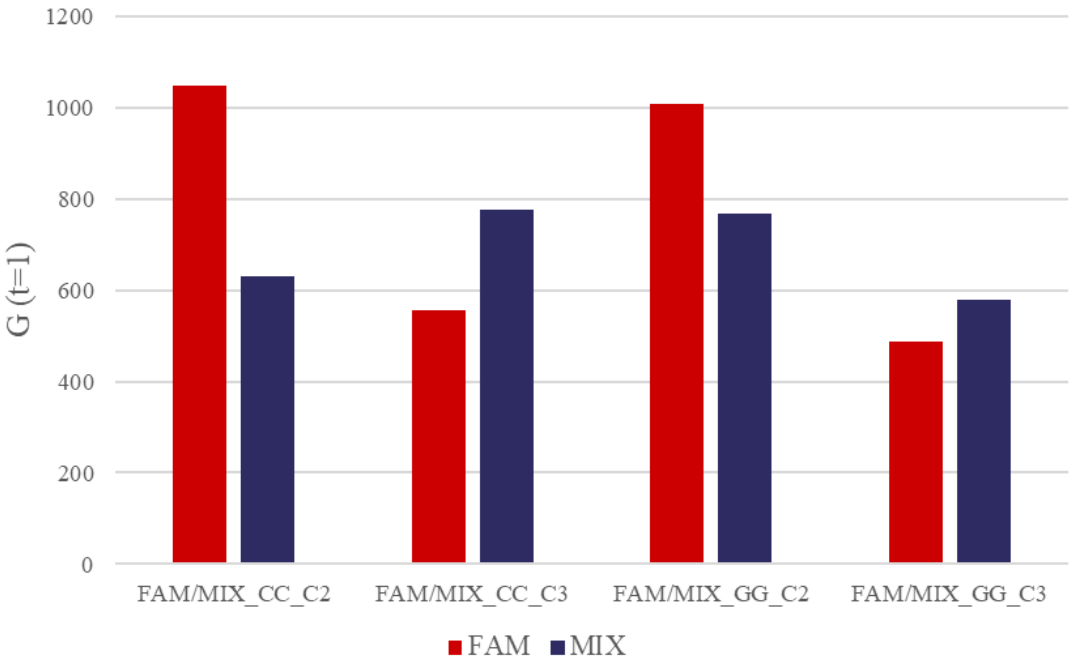

a)

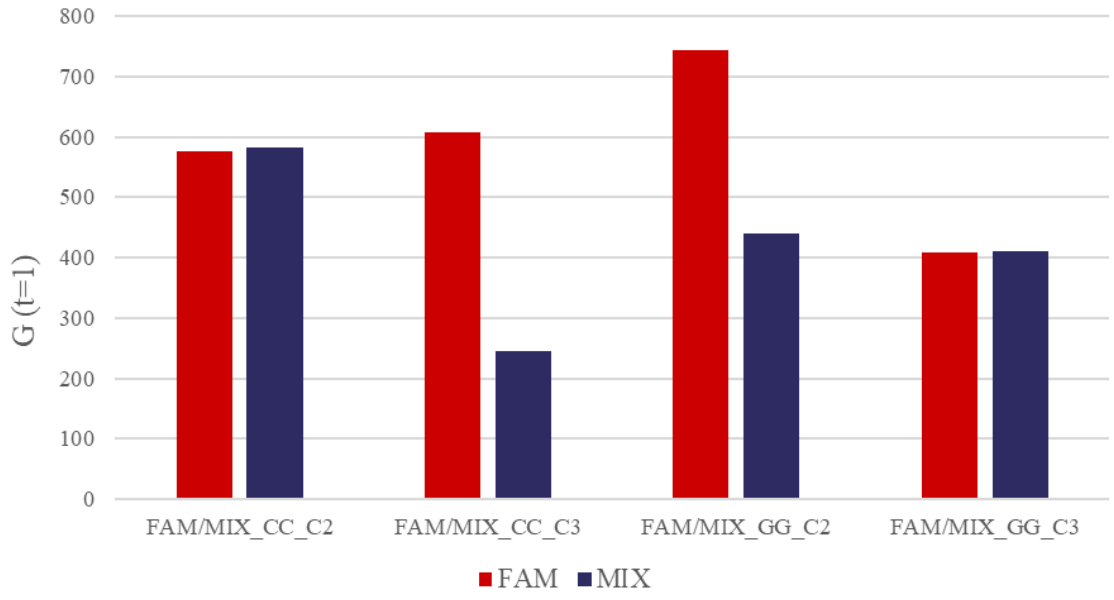

b)

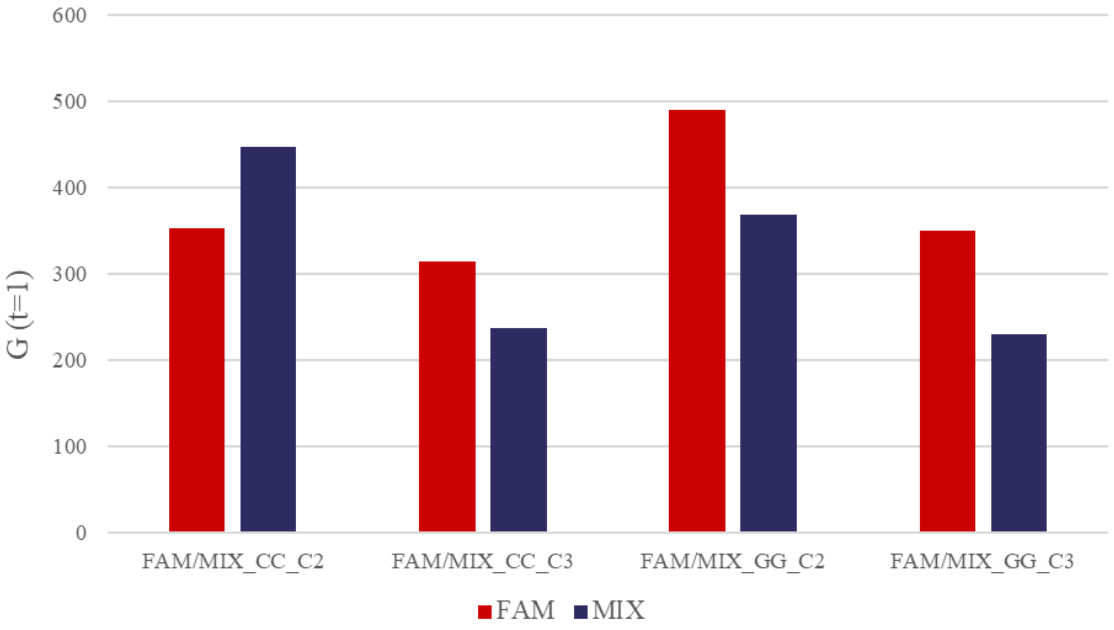

c)

Figure 4.26: average values of G (t=1): a) temperature of 5 °C; b) temperature of 15 °C; c) temperature of 25 °C

With the use of the big indenter, by analysing the previous values, it can be noticed a greater homogeneity between Mixtures and FAM than that of the first run.

Figures 4.27, 4.28 and 4.29 show the box plots of 95% confidence interval of E^* values.

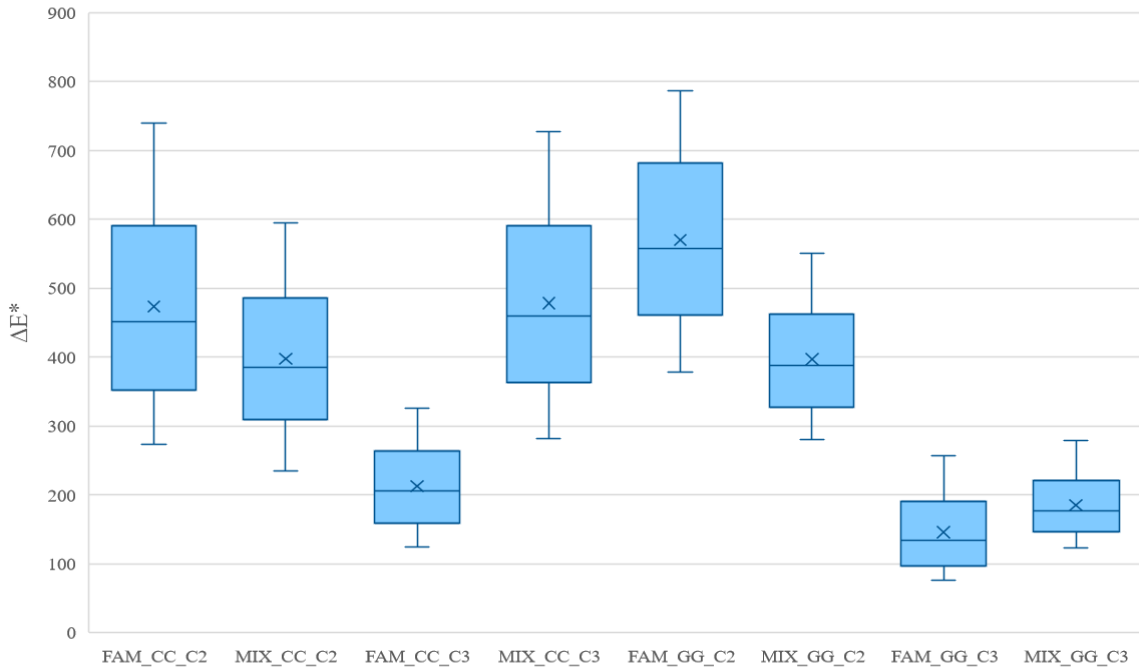

Figure 4.27: box plot representing ΔE values at temperature of 5 °C, with the big indenter*

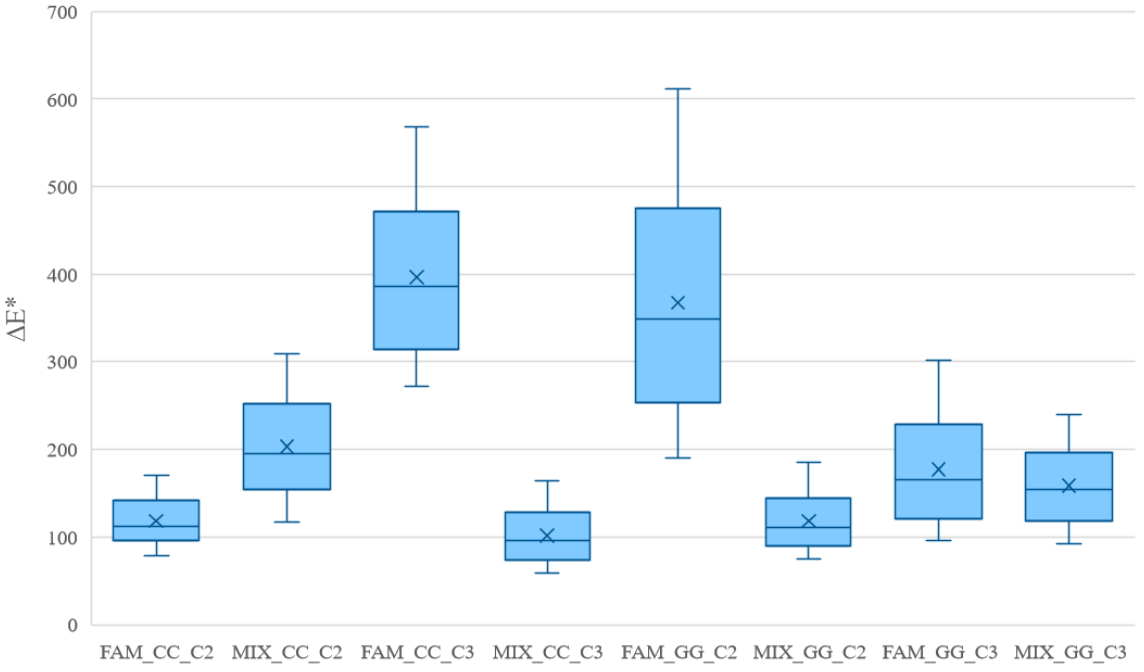

Figure 4.28: box plot representing ΔE values at temperature of 15 °C ,with the big indenter*

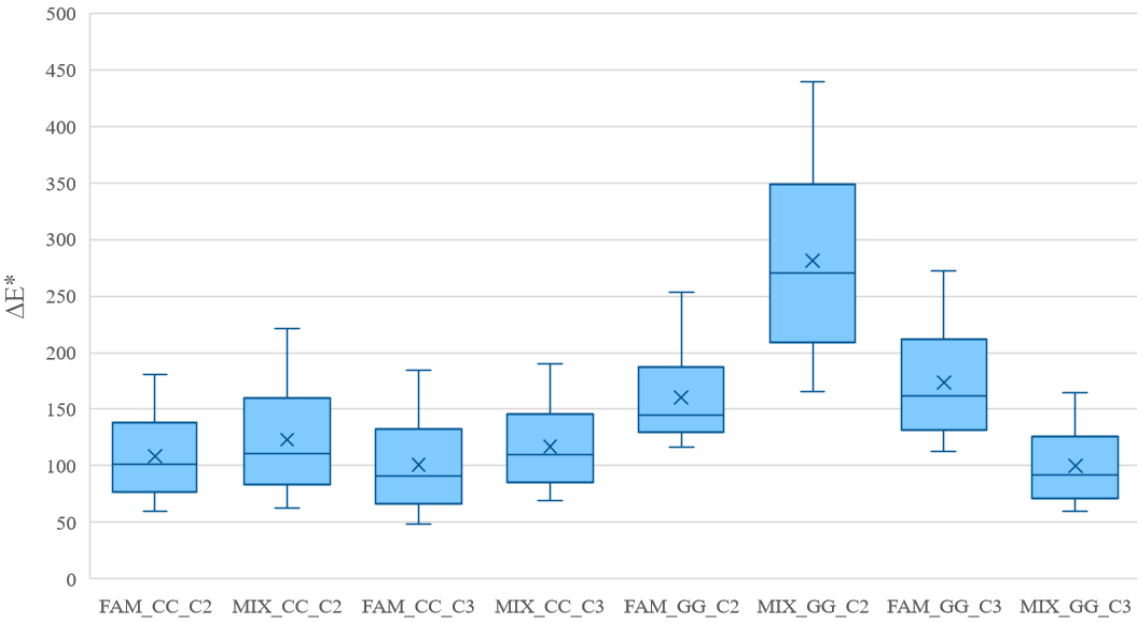

Figure 4.29: box plot representing ΔE values at temperature of 25 °C, with the big indenter*

Also analysing the ΔE^* values, it follows that the above considerations are confirmed.

4.4.4 Mastercurves

Figures 4.30, 4.31, 4.32 and 4.33 show the mastercurves constructed with the values obtained from indentation test, for FAM and Mixtures, with small and big indenter. Table 4.12, 4.13, 4.14, 4.15 report the shift factors.

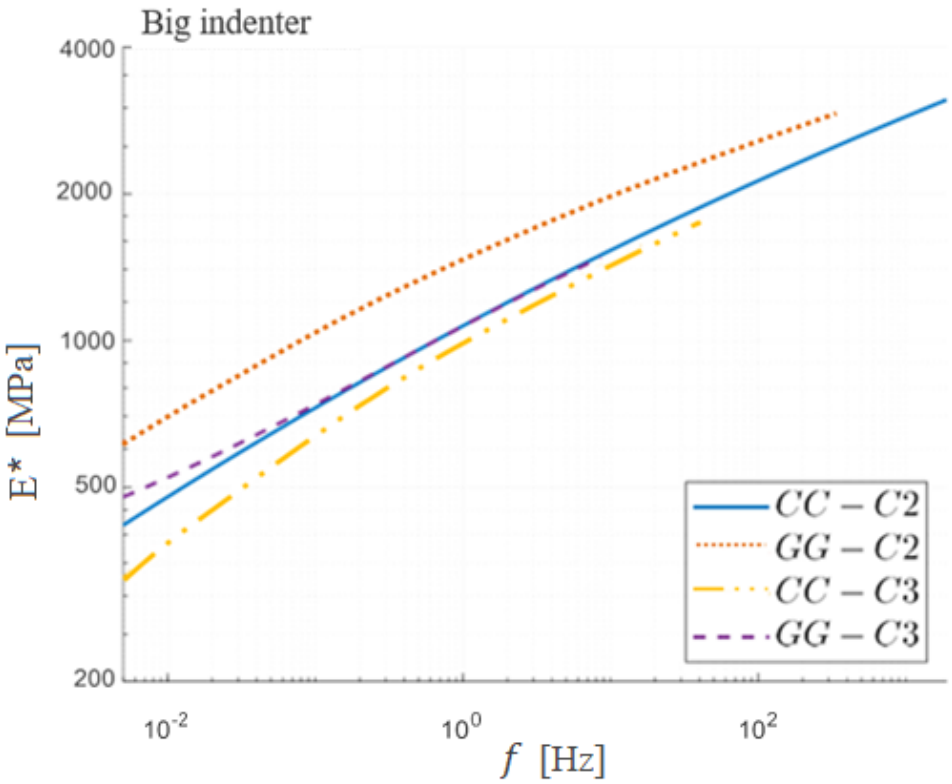

Figure 4.30: Mastercurves of FAM with big indenter.

Table 4.12: shift factors for FAM with big indenter

Material	5 °C	15 °C	25 °C
CC_C2	3,2872	1,4135	0
GG_C2	2,5656	1,3307	0
CC_C3	1,5653	1,629	0
GG_C3	0,9448	0,4027	0

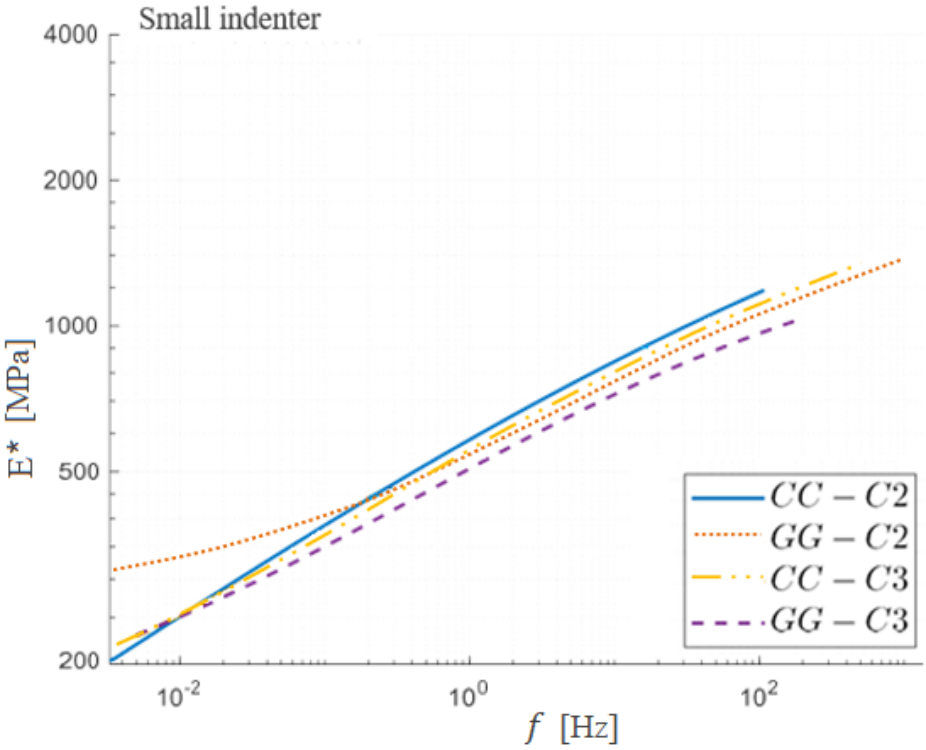

Figure 4.31: Mastercurves of FAM with the small indenter

Table 4.13: shift factors for FAM with small indenter

Material	5 °C	15 °C	25 °C
CC_C2	2,0345	1,327	0
GG_C2	3,1261	1,8792	0
CC_C3	2,8387	1,0662	0
GG_C3	2,2398	0,4097	0

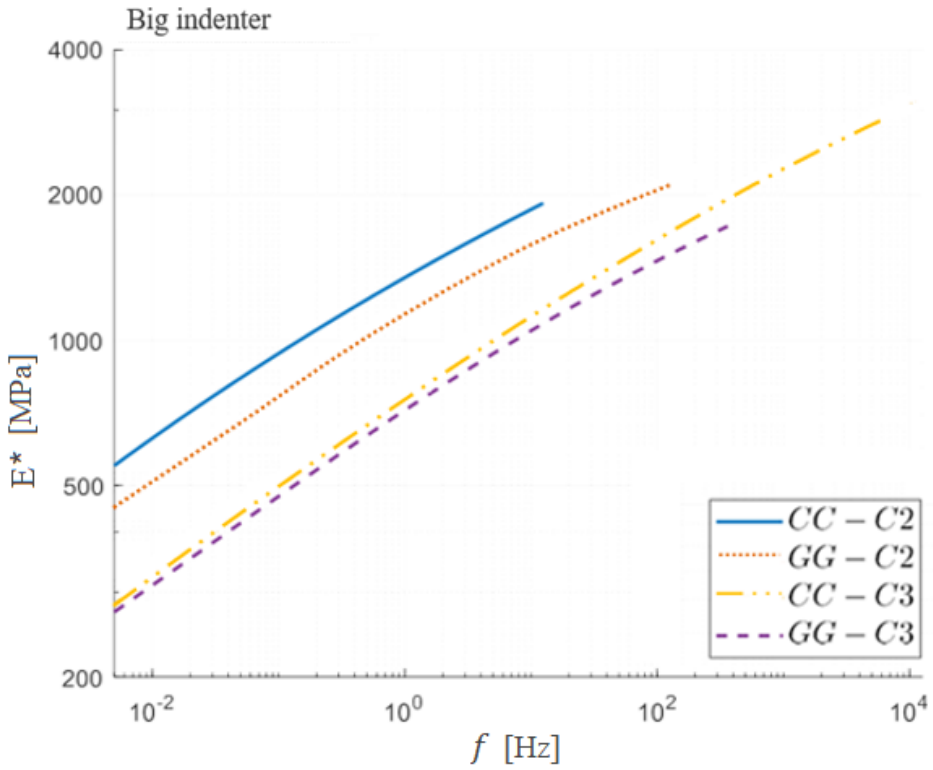

Figure 4.32: Mastercurves of Mixtures with big indenter.

Table 4.14: shift factors for Mixtures with big indenter

Material	5 °C	15 °C	25 °C
CC_C2	1,1091	0,8062	0
GG_C2	2,3256	0,4844	0
CC_C3	3,1122	0,0847	0
GG_C3	2,5706	1,5128	0

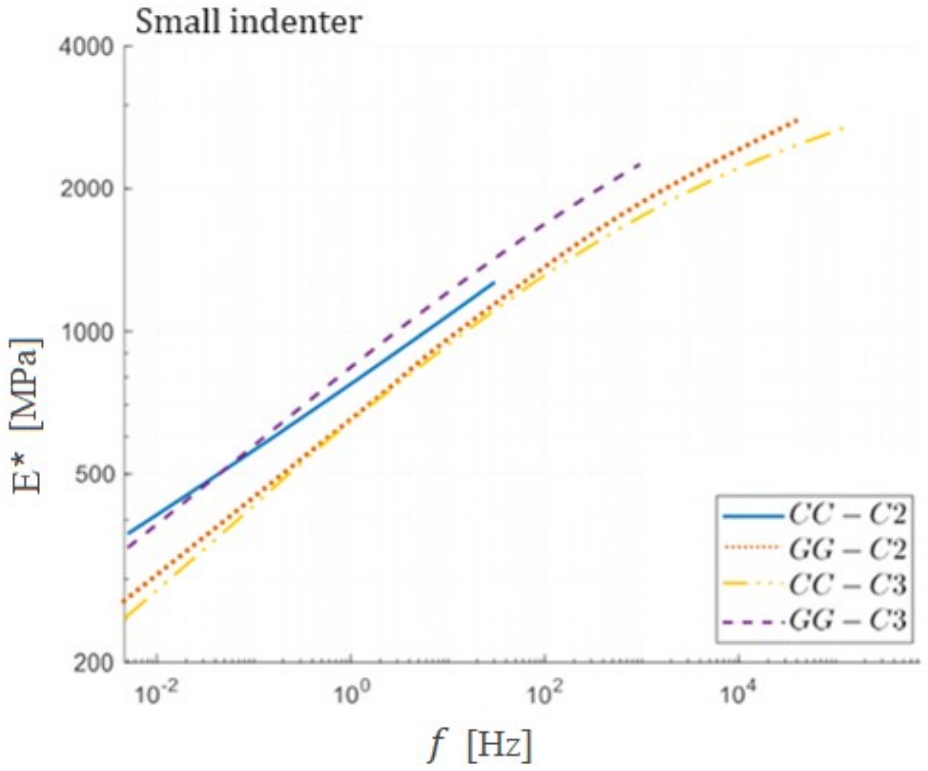

Figure 4.33: Mastercurves of Mixtures with small indenter

Table 4.15: shift factors for FAM with small indenter

Material	5 °C	15 °C	25 °C
CC_C2	1,4842	1,0528	0
GG_C2	4,3459	2,3059	0
CC_C3	3,8684	0,0334	0
GG_C3	2,9839	0,8154	0

The mastercurves have been built up respect to different samples, due to the characteristics of the test itself, so they are reported emphasizing the fact that they may be subject to a certain margin of error and variability.

4.4.5 Summary of second run testing

From the analysis of the results of the second run testing, the physical consistency of the values of E^* highlighted at the end of the first run is confirmed.

However, a further variability is introduced by the fact that tests at different temperatures are not carried out on the same specimen (this is the reason why some

isothermal curves overlap each other). Even if the material is the same, there is always an inhomogeneity between the different samples. The indentation test is very sensitive even to a minimum change of material. The impossibility of carrying out all tests on the same sample is due to the fact that, since this is a semi-destructive test, the mark caused by the indenter could modify the mechanical characteristics of the surface, making the subsequent measurements unreliable. This reason also influences the construction of the mastercurves, making it difficult to build on the same sample.

From the statistical analysis conducted on the results of $G(t = 1)$ of the second run, it is clear that, for the investigated materials, the big indenter ensures a greater homogeneity between FAM and Mixtures.

By analysing the values of the standard deviation, it follows that for FAM, the choice of indenter is less influential in terms of results dispersion. Instead, for the Mixtures, it is preferable to use the large indenter since the small one leads to a dispersion of the results too high.

4.4.6 Comparison between FAM and Mixtures

The figures 4.34, 4.35, 4.36, 4.37, 4.38, 4.39, 4.40, 4.41 compare the values of the complex Young's modulus E^* between Mixtures and FAM.

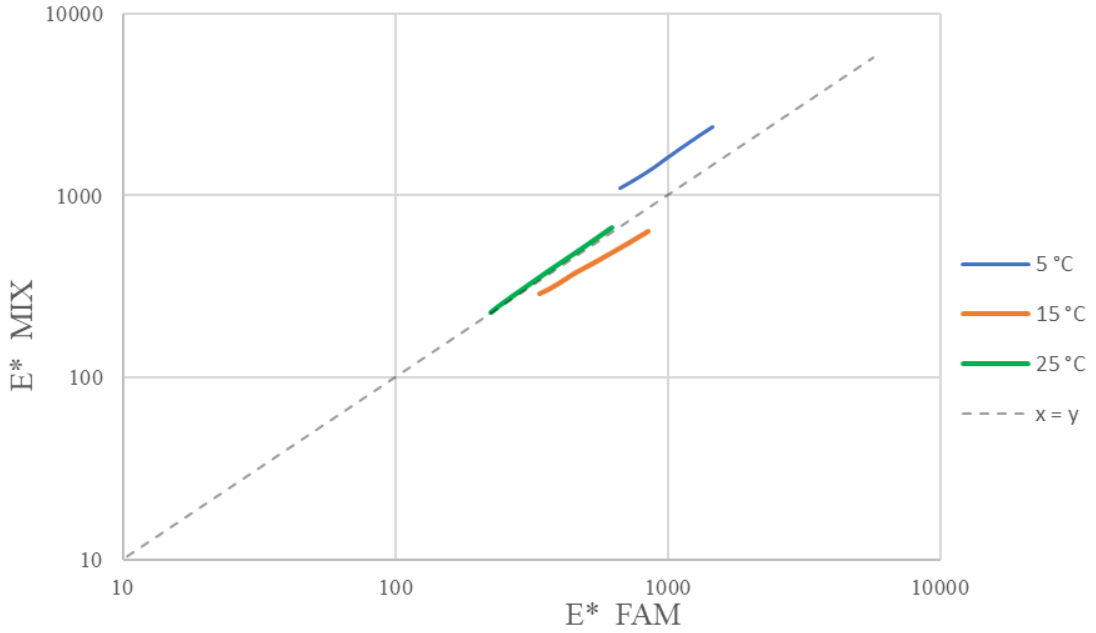

Figure 4.34: CC_C3 material and small indenter

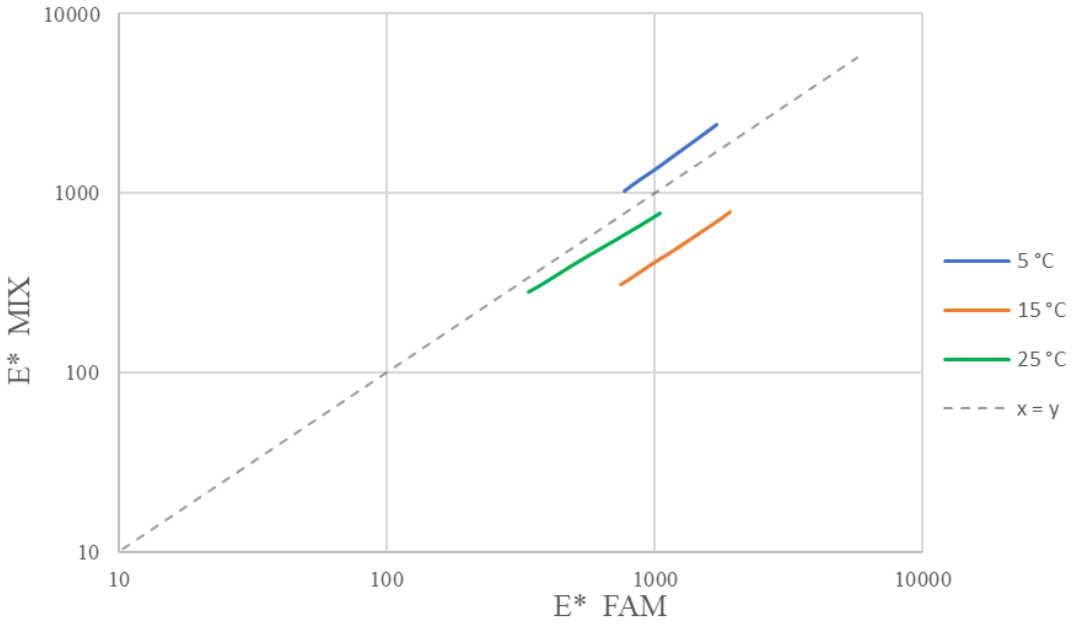

Figure 4.35: CC_C3 material and big indenter

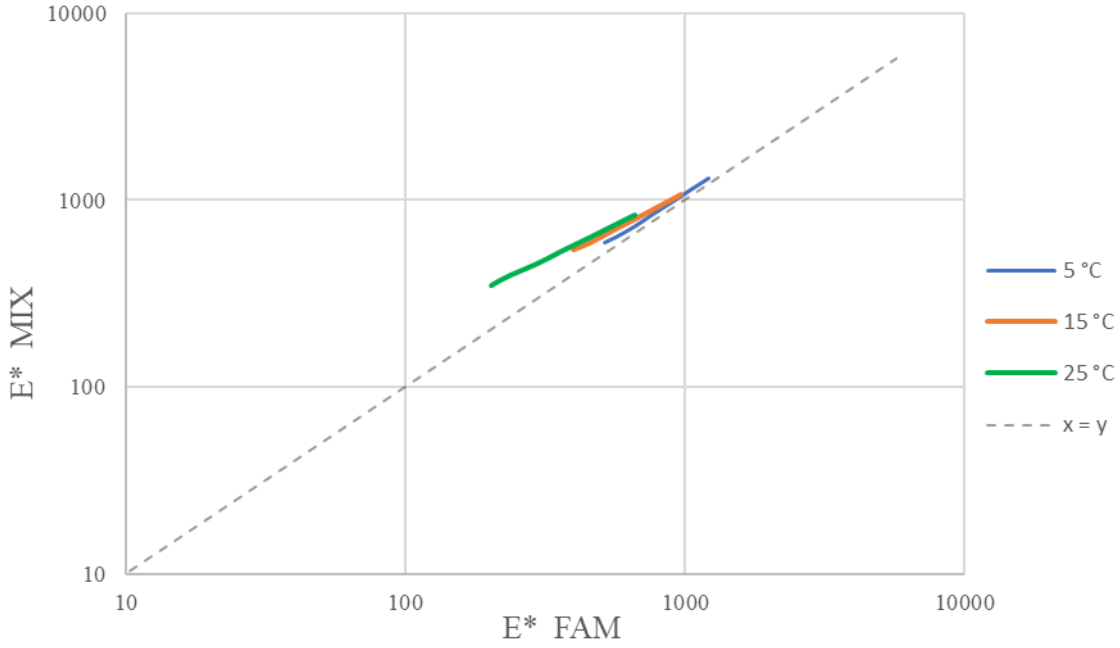

Figure 4.36: CC_C2 material and small indenter

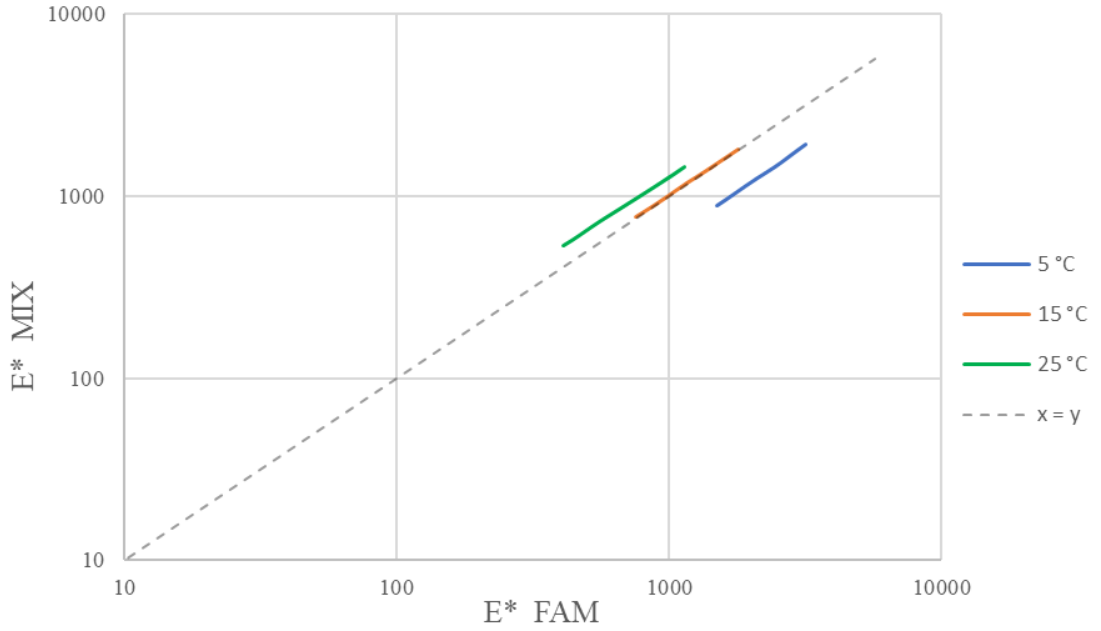

Figure 4.37: CC_C2 material and big indenter

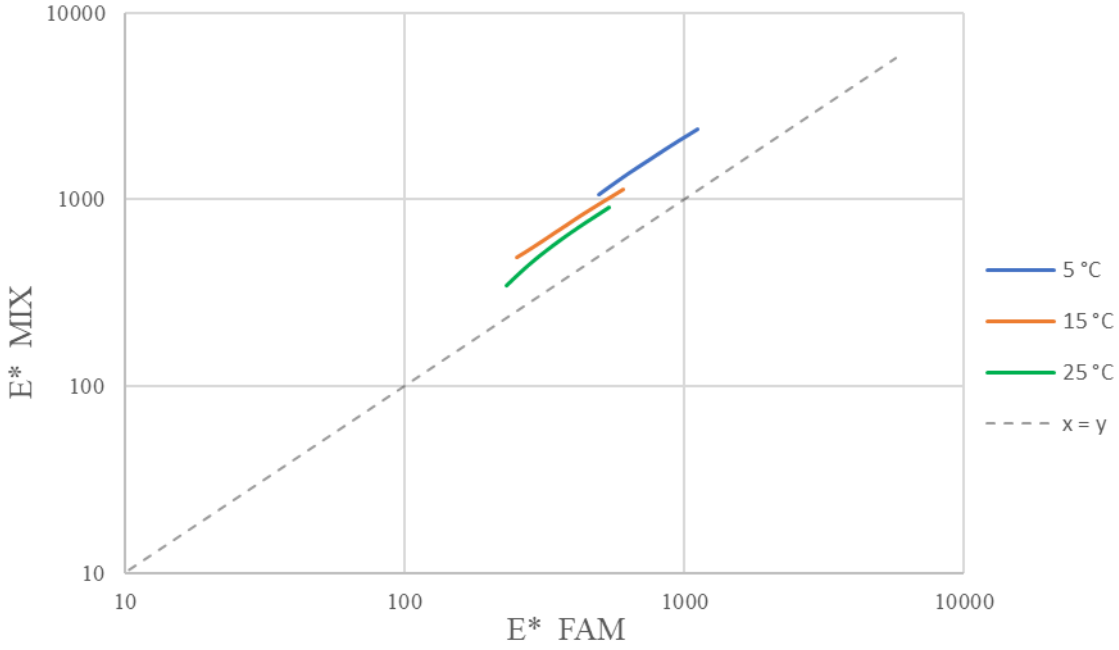

Figure 4.38: GG_C3 material and small indenter

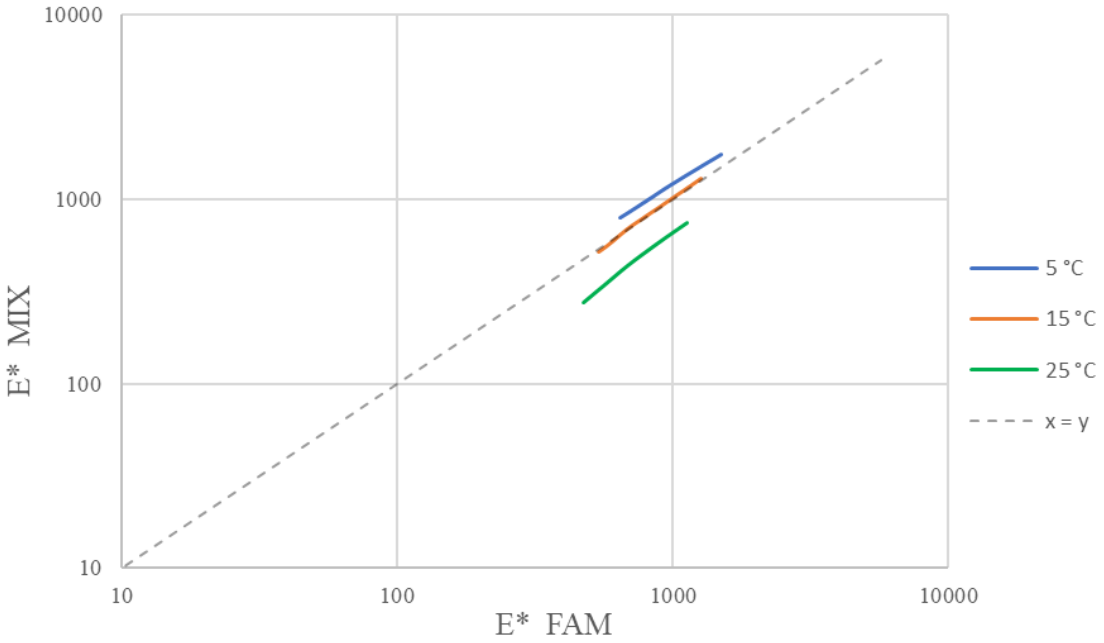

Figure 4.39: GG_C3 material and big indenter

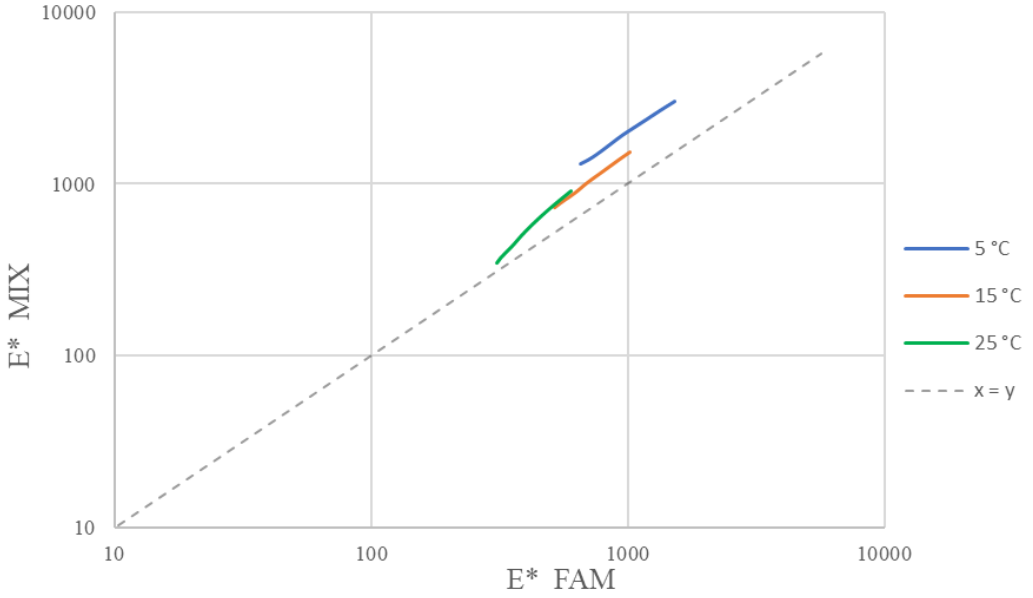

Figure 4.40: GG_C2 material and small indenter

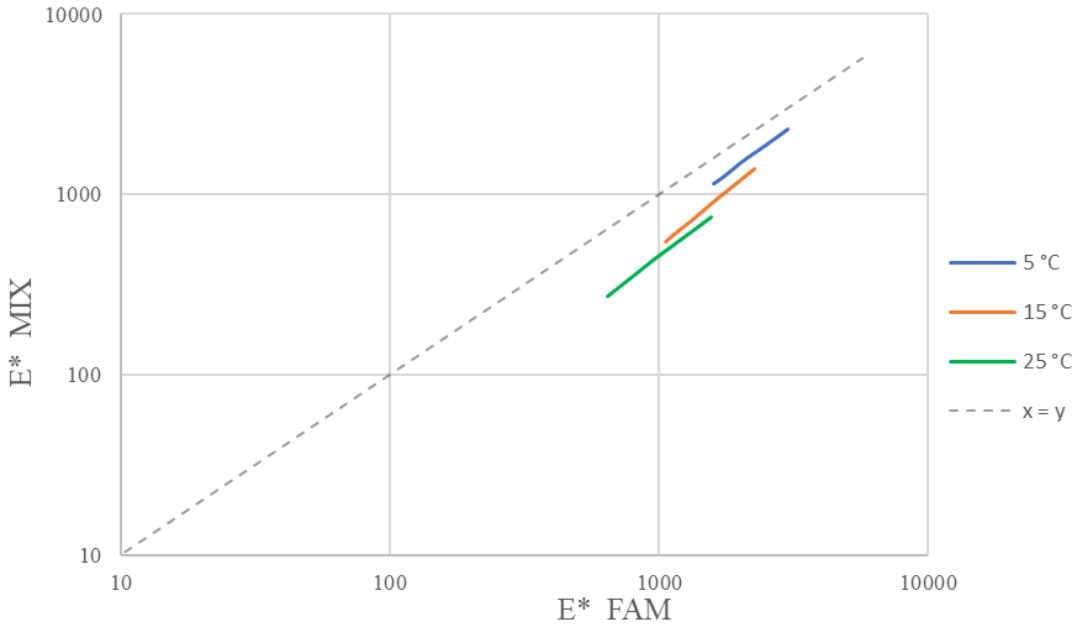

Figure 4.41: GG_C2 material and big indenter

Also in this comparison it can be seen that, using the small indenter, the Mixtures result stiffer than FAM. With the big indenter, it is confirmed a greater homogeneity, as also appears from the previous statistical analysis.

The ratio between Mixtures and FAM is contained in a range between 0,5 and 1.

4.5 Comparison with classical E^* test

Once the tests have been completed, the results obtained from the indentation test have been compared with those obtained through cyclic uniaxial compression tests, using an AMPT PRO system performed at "Laboratorio Strade e Trasporti" of DICEA at *Università Politecnica delle Marche.*

The relationship between the indentation tests measurements and the results obtained with the cyclic uniaxial compression tests on the corresponding CBTM is plotted in the Figure 4.42a-b:

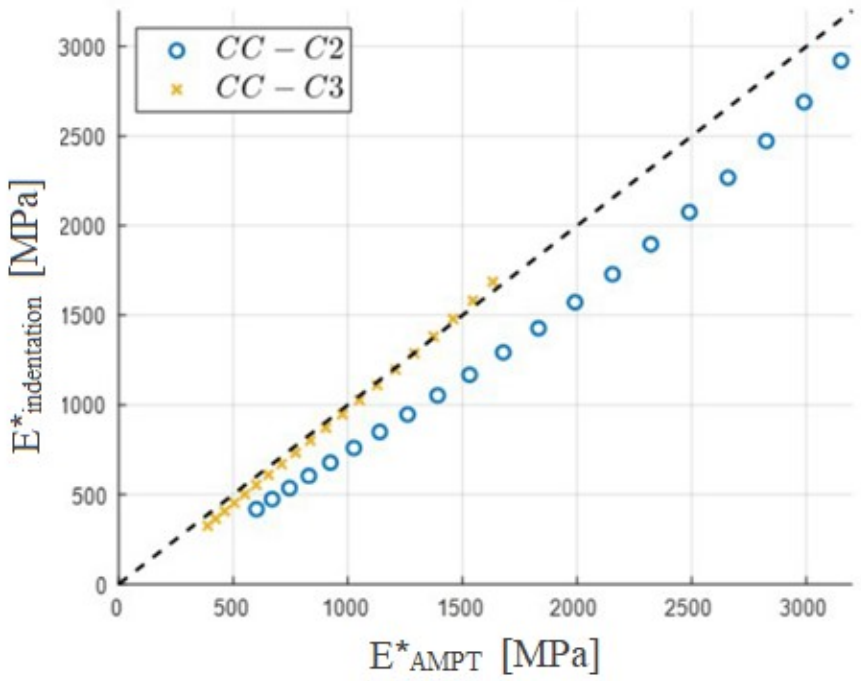
$CC-C2$
$CC-C3$
3000
2500
2000
1500
1000
500
0
0
500
1000
1500
2000
2500
3000
E*indentation [MPa]
E*AMPT [MPa]

a)

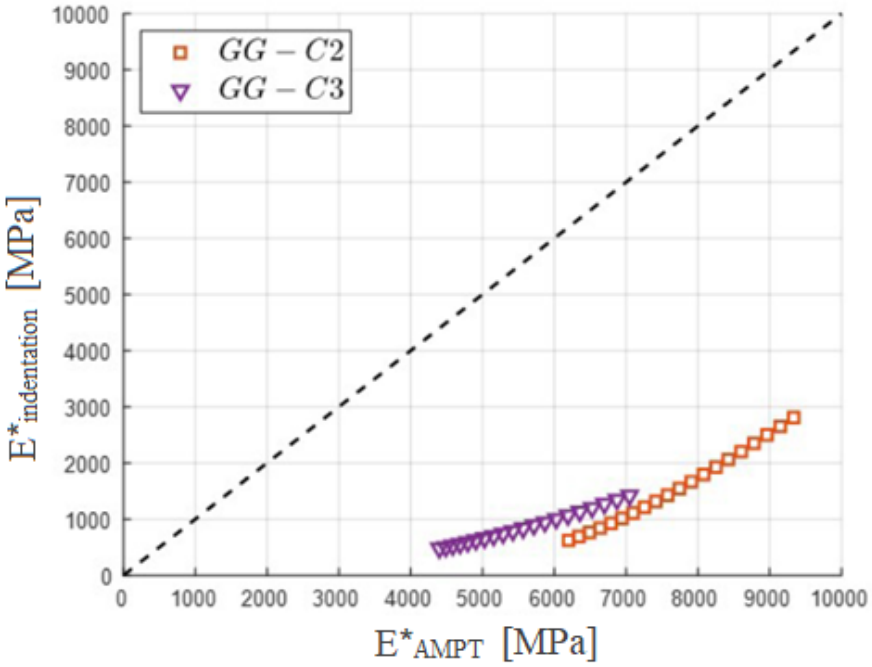

b)

Figure 4.42: Equality plots a) DG materials; b) GG materials

It follows that trend is consistent for DG grading (qualitative and quantitative) since exists a clear linear relationship between the indentation and cyclic uniaxial compression tests measurements:

$$G_{indentation}(t) = mG_{AMPT} \tag{4.3}$$

Where m is the slope of correlation line (Figure 4.43a-b).

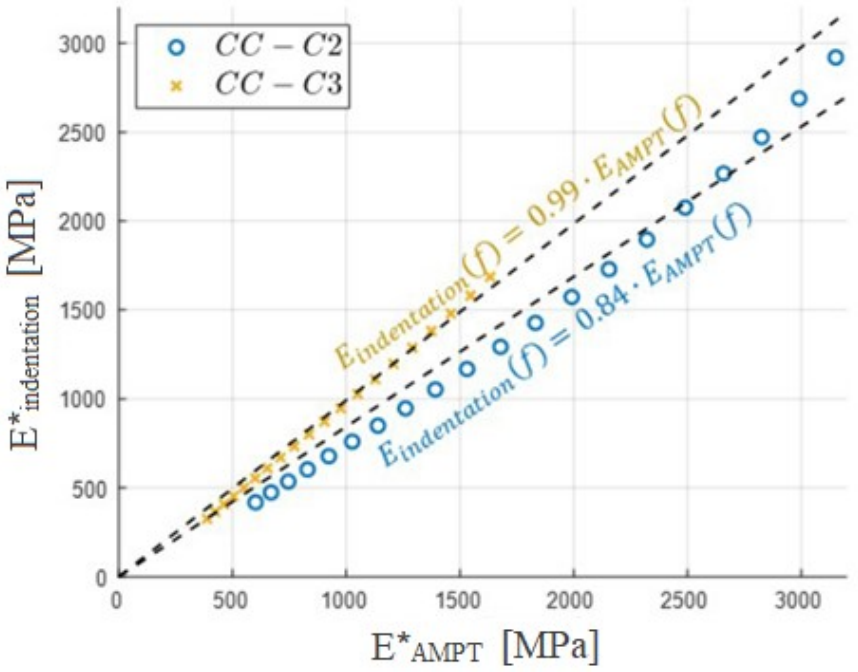

a)

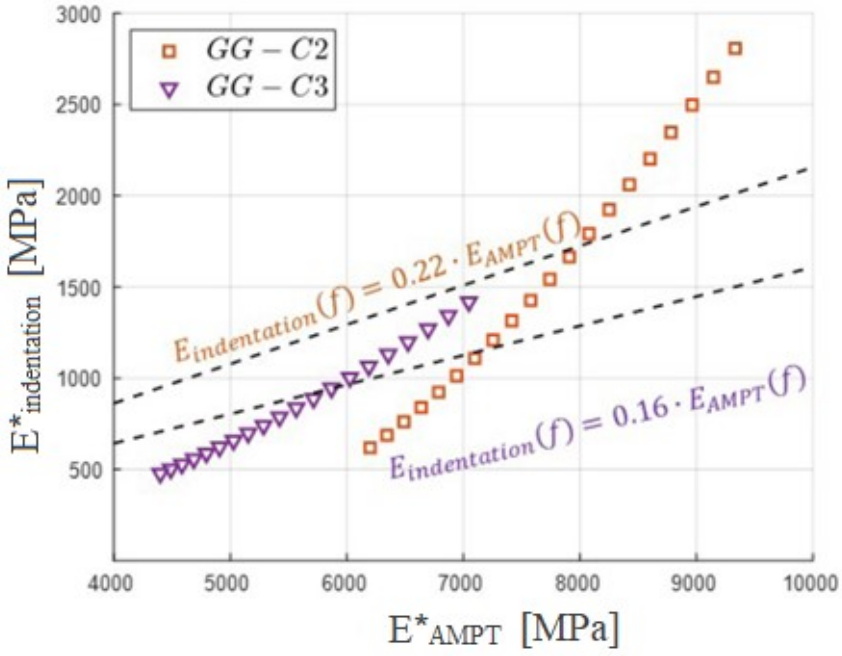

b)

Figure 4.43: linear relationship (quantitative and qualitative) a) DG materials; b) GG materials

It is possible for GG to get only a qualitative agreement but it is also possible to get a linear correlation between indentation results and cyclic uniaxial compression results (Fig 4.44a-b)

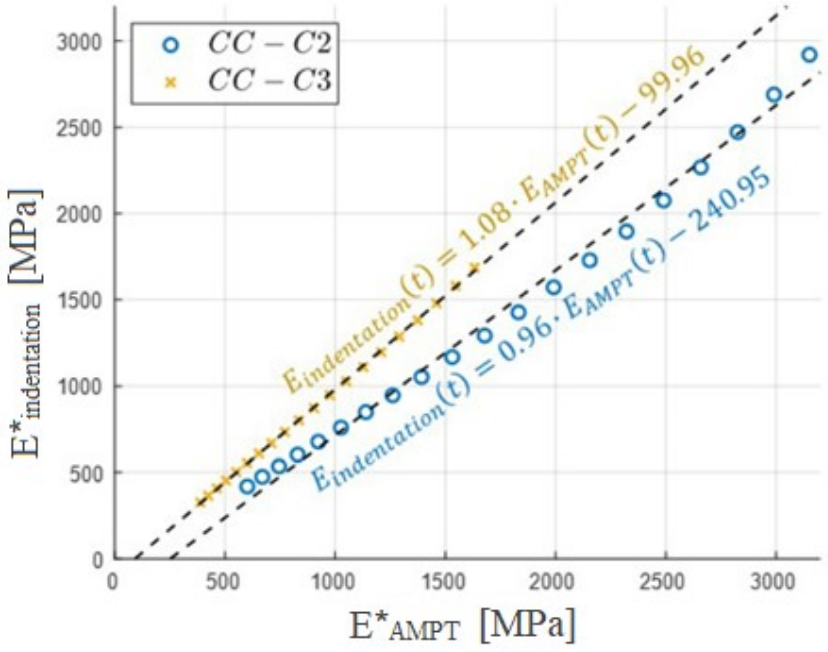

a)

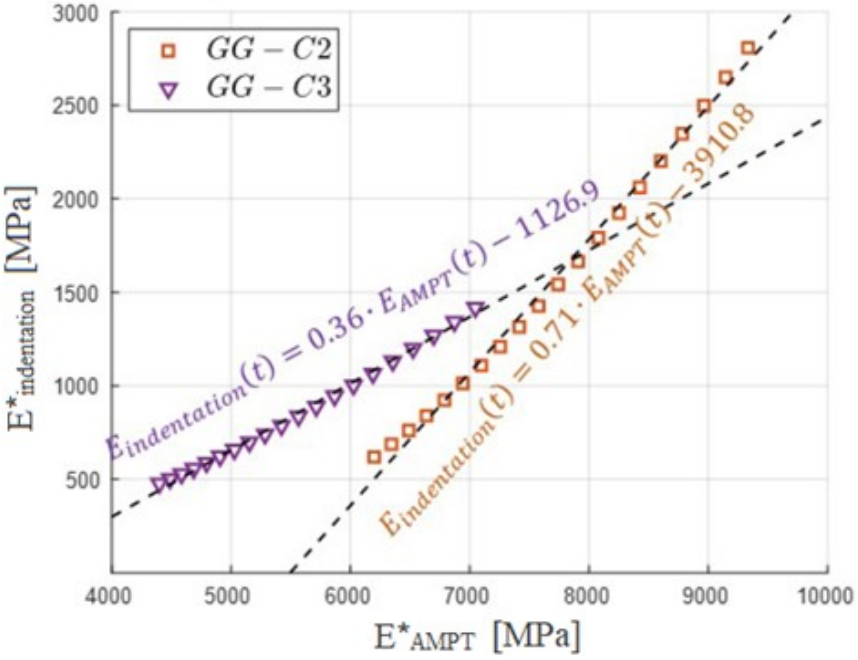

b)

Figure 4.44: correlation line a) DG materials; b) GG materials

The reason why the results of GG are not consistent could be related to linearity: it is necessary to explore better the preliminary tests about the linearity check to prevent a premature material breaking.

Conclusions

The main goal of this thesis was to evaluate the feasibility of the indentation test as a practical tool for measuring the complex Young's modulus of cold recycled materials mixtures. To this aim, mixtures and the corresponding fine aggregate matrix mortars were tested with two different types of indenter in terms of contact area (2.52 mm and 6.32 mm). Mixtures and mortars were produced with different grading distribution (dense graded and gap graded) and type of cement (Sulfoaluminous cement and Portland-slag cement).

The main results can be summarised as follows:

- The values of E^* increased as the test temperature was decreased and the test frequency was increased. This is physically consistent because cold recycled materials mixtures are time- and frequency-dependent materials;
- Statistical analysis of $G\ (t = 1)$ and 95% CI of E^* values showed that the variability of results was more noticeable with the small indenter than the big indenter. This was due to the scale effect, since the dimension of the coarse aggregate was comparable with the indentation areas;
- The scale effect was more evident in mixtures (due to the presence of coarse aggregate) and less marked in mortars. For the latter, the indenter type had a minor effect.
- Indentation tests performed on different samples of the same mixture/mortar were affected by the sample-to-sample variability. Therefore, the construction of mastercurves using different specimens did not lead to reliable results. On the other hand this highlighted that the indentation test was sensitive to sample-to-sample variability;
- The comparison with the complex modulus results obtained from cyclic compression tests carried out at "Laboratorio di Strade e Trasporti" of DICEA at *Università Politecnica delle Marche,* showed good agreement for the dense

graded mixture. For the gap graded mixtures the E^* values measured with the indentation test were considerably lower than those obtained with cyclic compression tests. This could be explained considering the effect of non-linearity on the indentation results.

The research also suggested possible future developments:

- The use of larger cylindrical specimens, both in terms of height and width (e.g. 150 mm) should be considered. This would allow having more surfaces available on which to perform the tests on the same sample at different temperatures, and thus obtain mastercurves not affected by sample-to-sample variability;
- The sensitivity of the indentation test could be used to assess the homogeneity of a single sample. To this purpose the test could be carried out also on surfaces orthogonal with respect to the compaction direction;
- More attention should be paid to the linearity check, considering that the linearity limit could be mixture-dependent.

References

(1) MIGNINI, Chiara; CARDONE, Fabrizio; GRAZIANI, Andrea. Using fine aggregate matrix mortars to predict the curing behaviour of cement bitumen treated materials produced with different cements. *Construction and Building Materials*, 2021, 268: 121201.

(2) XIAO, Feipeng, et al. A literature review on cold recycling technology of asphalt pavement. *Construction and Building Materials*, 2018, 180: 579-604.

(3) MIGNINI, Chiara; CARDONE, Fabrizio; GRAZIANI, Andrea. Experimental study of bitumen emulsion–cement mortars: mechanical behaviour and relation to mixtures. *Materials and structures*, 2018, 51.6: 1-14.

(4) GRILLI, Andrea; GRAZIANI, Andrea; BOCCI, Maurizio. Compactability and thermal sensitivity of cement–bitumen-treated materials. *Road Materials and Pavement Design*, 2012, 13.4: 599-617.

(5) ARRA, asphalt recycling and reclaiming association. Basic asphalt recycling manual. *U.S. Department of Transportation*, Federal highway Administration, 2001.

(6) BOCCI, M., et al. A study on the mechanical behaviour of cement–bitumen treated materials. *Construction and building materials*, 2011, 25.2: 773-778.

(7) MIGNINI, Chiara. Multiscale Approach for Characterising the Behaviour of Cold Bitumen Emulsion Materials. *PhD Thesis,* 2021.

(8) FADIL, Hassan, et al. Measurement of the viscoelastic properties of asphalt mortar and its components with indentation tests. *Road Materials and Pavement Design*, 2019, 20.sup2: S797-S811.

(9) ROYLANCE, David. Engineering viscoelasticity. Department of Materials Science and Engineering, Massachusetts Institute of Technology, 2001.

(10) HERTZ, H., Über die Berührung fester elastischer Körper. *Journal Für Die Reine Und Angewandte Mathematik*, 1881,*92*, 156–171.

(11) LEE, E. H., RADOK, J. R. M. The Contact Problem for Viscoelastic Bodies. *Journal of Applied Mechanics*, 2011. *27*(3), 438

(12) KRAUS, Michael A. et al. Parameter identification methods for visco-and hyperelastic material models. Glass Structures & Engineering, 2017, 2.2: 147-167.

(13) PARK, S. W.; SCHAPERY, RA0942. Methods of interconversion between linear viscoelastic material functions. Part I—A numerical method based on Prony series. International journal of solids and structures, 1999, 36.11: 1653-1675.

(14) RILEM, Multiphase characterization of cold bitumen emulsion materials. *Methodology for the materials preparation and testing*, 2019.

(15) MTS 810 & 858 Material Testing Systems. MTS Systems Corporation, 14000 Technology Drive - Eden Prairie, MN 55344-2290 USA

(16) INSTRON, Universal Testing Machine Compliance.